Bright Trans-Neptunian Objects in the Southern Sky

Michele Taisia Bannister

A thesis submitted for the degree of

Doctor of Philosophy

of the Australian National University

Australian National University

Research School of Astronomy & Astrophysics

Submitted 20th February 2013

Disclaimer

I hereby declare that the work in this thesis is that of myself alone, except where indicated in the text of the thesis. The work was undertaken between February 2008 and February 2013 at the Australian National University, Canberra, and during visits to the California Institute of Technology, Pasadena. It has not been submitted in whole or in part for any other degree at this or any other university.

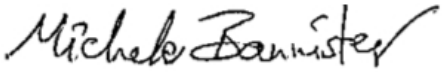

Michele Taisia Bannister
20th February 2013

Acknowledgments

The path of any scientific project is one of surprises, reversals and tangled, misaligned, or missing data; I have been glad to have many people to help.

I am indebted to my supervisors Mike Brown, Paul Francis, and Brian Schmidt. Mike, who taught me how to know when not to aggregate bad data with good, and how to tell when one has gone beyond what has been done before; Paul, for the art of clearly communicating one's science, posing a succinct question and how it will be tested, and for sounding out all ideas; and Brian, whose humility and kindness are a model of exemplary leadership for how to manage big collaborations. Thank you all.

To my beloved Michael, husband and friend: thank you, for all the time, encouragement and patience. Your enthusiasm and love has made all this work possible.

Thank you to my friends in Canberra and overseas - the pleasure of your company has made this journey joyful. The same of the students and staff of Stromlo and of Caltech Planetary Science, past and present: especially those in our Caltech research group, Meg, Wes, and Kon, and officemates Zane and Terry-Ann for lively and stimulating discussions. I hope we have many more chances to collaborate.

To my colleagues in the science-Twitter network, in Stromlo Student Outreach, and in the Secret Poetry Cabal — your professional camaraderie helped build my knowledge and confidence, and helped me keep alive the fierce joy in scientific exploration: it is brought out better by sharing it with others.

I recognise and acknowledge the significant cultural role and reverence that the Warrumbungles have within the communities of the traditional owners, the Gamilaroi, Wiradjuri and Weilwan peoples. We are most fortunate to have the opportunity to conduct astronomical observations from Siding Spring Mountain.

This research has made use of many of the astronomical tools developed worldwide and made freely available to all: I thank the staff of NASA's Astrophysics Data System, those of NASA/Caltech Jet Propulsion Laboratory who work on HORIZONS, and the Minor Planet Center, for their invaluable service to the community. I also appreciate the ever-patient team of `sysman` at Stromlo, who have rebooted `miner` for me more times than they may like to remember. Thank you also to the Catalina team, who made their data available for my thesis, and to the tireless observers who created my half-million images of the southern sky: Rob, Gordon and Donna.

Finally, to my parents: this may have all started when we visited the Sydney Observatory one birthday and saw the marks of Shoemaker-Levy 9 just spinning into view on the disk of Jupiter, but it was your love and support all these years since that made it possible. This thesis is dedicated to you both.

I wish to gratefully acknowledge the financial support for this research from the Australian government via an Australian Postgraduate Award, an ARC grant, from the Joan Duffield Postgraduate Scholarship, and from the Astronomical Society of Australia for me to present this research at the EPSC-DPS Joint Meeting, Nantes, France, in October 2011.

Abstract

We complete the census of bright distant trans-Neptunian worlds through surveying the Southern Hemisphere sky, particularly the unexplored high-latitude regions that would contain trans-Neptunian objects (TNOs) that have experienced severe scattering.

In this thesis, we developed an archival TNO survey of 6,275 square degrees of sky south of the ecliptic that have more than thirty nights of observation over five years, to a limiting magnitude of 19.0 in clear. We generated our survey through an innovative analysis of the archive of more than half a million images taken between 2 March 2004 and 23 October 2009 by the Siding Spring Survey. This survey for near-Earth asteroids uses the 0.5 m Uppsala telescope at Siding Spring Observatory. Our survey took advantage of their dense temporal coverage to resample their cadence of observation into a survey for slow-moving objects. From twenty billion astronomical sources on the Uppsala images, we extracted thirteen million transient sources, computed a subset of the trillion possible Solar System orbits that these points of light could form, and produced only a few hundred potential candidate TNO orbital arcs. This computational processing required a hundred thousand hours of CPU time.

Our survey adds to the last two decades of work into understanding the cold, distant outer regions of our Solar System that lie beyond Neptune's orbit. These regions contain varied populations of small objects. As the remnant planetesimals of the protoplanetary disk, they offer insight into the early history and evolution of the Solar System. The brightest reflect enough photons to allow spectroscopy, indicating the composition of the topmost few millimetres of the volatile ices that form the mantles of these worlds. The sixteen hundred TNOs known have been discovered through sky surveys with optical telescopes; most extensive surveys have previously focussed on the Northern Hemisphere sky.

We detected no new objects in the southern sky. We defined the exact phase space of orbital parameters that was well sampled by the Uppsala TNO survey by developing a survey simulator. Examining our survey's observation of the objects from a well-characterised synthetic population, we found we had a 90% detection efficiency of the Kuiper belt and scattered disk; seeing no objects with an absolute magnitude between our range of sensitivity of -2.5 to 3.5 limited the bright end of the TNO population distribution.

We unsuccessfully attempted to characterise two of the known distant objects. Pluto's largest moon, Charon, is suspected to have cryovolcanism-related ammonia on its surface; we observed in the L-band with Gemini North's GNIRS spectrograph to improve the detection, but received too little telescope time to detect Charon. In contrast, little is known about the newly discovered high-inclination Centaur-like object 2012 DR30: we obtained a light-curve with the Faulkes South 2m, but found only that this object was unvarying in brightness at better than the 5% level.

Contents

CHAPTER 1

Introduction

> Is it not likely that in Pluto there has come to light the first of a series of ultra-Neptunian bodies, the remaining members of which still await discovery but which are destined eventually to be detected?
>
> – Frederick C. Leonard
> August 1930

The realisation of the true extent of the populations in the outer regions of our Solar System has been a triumph in the development of our understanding of planetary systems. In the last two decades, Leonard's hoped-for *ultra-Neptunian bodies* have come to light in beautiful and unexpected variety. These distant icy worlds, the remnants of the protoplanetary disk, offer insight into the early history and evolution of the Solar System (Barucci et al. 2008a). They have been extensively surveyed in the Northern Hemisphere sky; the eight[1] dwarf planets discovered are sufficiently bright for detailed spectroscopic study, and have illuminated the evolution of volatile species far from the Sun (Brown 2012). Their abundant smaller brethren retain the dynamical disturbances from the early rearrangements of the architecture of the major planets. Around two hundred thousand that are larger than 100 km in diameter are thought to exist (Petit et al. 2011)[2]; some sixteen hundred[3] have been found. This sample of the population has revealed a fascinating level of diversity: spectrally ultra-reddened objects (Sheppard 2010), objects on retrograde orbits tilted near-perpendicular to the plane of the Solar System (Gladman et al. 2009), populations defined by having their orbits held in weak filaments of gravitational resonances (Gladman et al. 2008), dwarf planets with moons on non-Keplerian orbits (Ragozzine & Brown 2009), and the first inner Oort cloud object (Brown et al. 2004).

However, no survey has yet explored the whole sky; only minimal surveying has yet been made in the Southern Hemisphere, beyond declinations of -35 degrees (Trujillo 2008). This

[1] Table at http://www.gps.caltech.edu/~mbrown/dps.html, updates daily

[2] Petit et al. (2011): inner classical belt $130k^{+30k}_{-27k}$, outer/detached classical belt $80k^{+60k}_{-40k}$, scattered $5k^{+5k}_{-3k}$.

[3] The Minor Planet Center reported 356 Centaurs/scattered objects and 1249 TNOs on 3 July 2012.

thesis surveys the southern sky and completes the census of the brightest of these distant worlds, begun more than eighty years ago (Tombaugh 1961).

In this chapter, we outline why a sky survey is scientifically valuable: we begin with our current understanding of the trans-Neptunian populations' origin at the dawn of the Solar System (§ 1.1), their taxonomy and spectral colours (§ 1.2), and the observed and physical properties of dwarf planets (§ 1.4). The photographic wide-field sky surveys that have provided the observations that underlie this understanding started early in the twentieth century, but did not approach their present sophistication until the early 1990s. We review these, their requirements and inherent biases, and the limits that they have placed on the trans-Neptunian population in § 1.3. We conclude in § 1.5 by summarising this overview of the state of the field and how, by surveying the southern sky, this thesis will provide an original contribution to our knowledge of the outer Solar System.

1.1. Origin of the trans-Neptunian populations

The outer Solar System encompasses the objects that orbit between and beyond the orbits of Jupiter, Saturn, Uranus and Neptune, the enormous worlds that gravitationally dominate our planetary system. In this thesis, I considered the much smaller occupants of this region, particularly those in the remote and vast outer reaches beyond Neptune: the trans-Neptunian objects (TNOs). To understand how many TNOs exist of each size, and how they are distributed on orbits around the Sun, we must first consider what is known of the processes that formed and sculpted their populations. The discovery and mapping of the TNO population will allow greater insight into the details of these physical processes.

Like the other planetary bodies in the Solar System, trans-Neptunian objects formed when the Sun was young, in its T Tauri phase, and surrounded by a slowly accreting disk of dust and gas. This dust was mainly crystalline silicates: Mg-rich olivine and orthopyroxene (Taylor 2001) The heat of the young Sun controlled the gas temperature and pressure in the protoplanetary disk, and the magnetorotational instability of the Sun's magnetic fields threading the disk drove turbulence in the disk. Together, these created a unique set of ice lines: the distance from the Sun at which each volatile species could condense from the disk's gas into a solid, where it could then contribute to a forming icy body. The H_2O or snow line, where the disk cooled to 145-170 K, was at 2.7 AU, according both to theory and observation of the asteroid belt (Lecar et al. 2006). At 160 K and 10^{-6} bar, the water ice was crystalline; at 145 K it was instead amorphous ice (Taylor 2001). The ice lines migrated during the disk evolution as the infall accretion rate dropped. The snow line may even have moved inside the present Earth's orbit, though this is inconsistent with the current 0.02 wt% water content of the Earth (Oka et al. 2011).

There are two current models for the formation of the earliest planetesimals from the primordial nebula. Either turbulence-induced instabilities in the disk coalesced into small clumps of material, or disk material coagulated by collisions into small clumps. Gas drag within the disk pulled the dust present towards the star, producing orbits at different rates; gas drag and turbulence then controlled the collisional velocities. Beyond the snow line, water contributed up to 50% of the mass of the nascent planetesimals, as much as that from silicon and iron (Martin & Livio 2012).

Radionucleide studies show that the agglomeration and growth from micron-diameter dust to centimetre-sized nuggets happened in the rapid span of < 50 kyr (Dauphas & Chaussidon 2011). Surface effects held particles together on the micron scale, the strength of the "dust bunnies" took over at the millimetre to metre scale, and gravity dominated the structure of the body once it was larger than kilometres in size.

The physics guiding the growth between the metre-diameter scale and the kilometre-diameter scale of these little planetesimals is not entirely clear. The gas drag in the disk would have caused a one-metre body at one AU to drift into the Sun on a timescale of only a hundred years. The relative orbital velocities for metre-scale objects set the maximum relative velocities at any stage of planetesimal growth: they produce collisions that in simulations grind the little planetesimals into dust, rather than allowing them to agglomerate into larger objects (Kenyon et al. 2007).

At sufficiently small sizes, collisional grinding took place: this size transition was a function of the velocity dispersion — the RMS of the inclination and eccentricity of the TNO orbits. The velocity dispersion of 1.5 km/s (Jewitt 2000b) meant that all TNOs smaller than dwarf planets were ground down by further collisions, rather than continuing to grow. Eventually they reached dust-size, and were lost from the Solar System through the slow displacement of radiation pressure. The present level of dust in the Kuiper belt is exceptionally low; the New Horizons mission carries an instrument to make the first direct measurement, but it is already known to be sufficiently low, with an optical depth of $\tau \sim 10^{-7}$ in micron-size particles, that the region can be considered dust-free (Jewitt 2000b). The only present-day dust production is from TNO erosion from collisions with interstellar dust particles (Jewitt 2000b). This contrasts with the dusty disks of the Kuiper belt analogues of extrasolar systems seen today, which to be detected at all are in a dust-rich early phase of their evolution.

This past bridging of the metre-to-kilometre scale in their growth to larger worlds remains an area of active theoretical research. The historical picture becomes clearer once the planetesimals grew by accretion of gas, dust and smaller planetesimals over a few million years to diameters of several kilometres. Then the planetesimals lived in a realm of physics where worlds grew by collision, and the abundance of small worlds meant that collisions were frequent. Collision on collision, the nascent planets accreted each other and grew in size.

Several embryos became more dominant in their growth rate; the exact mechanisms are unclear but include a feedback loop of runaway growth for the "oligarch" embryos. The largest swept out channels in the gas of the primordial nebula as it rotated around the infant Sun, leaving grooves to mark their passage. Cleared gaps suggestive of such activity are seen in the disks of extrasolar protoplanetary disks ("transitional disks"): gas giant planets have been directly imaged in such warped and structured disks, e.g. β Pictoris (Lagrange et al. 2010) and, in the case of LkCa15, with a source in the gap inferred to be such a protoplanet (Kraus & Ireland 2011). This phase of planetary embryos lasts another several million year (Dauphas & Chaussidon (2011) and references therein).

By several tens of millions of years after the Sun's formation, comparison with the evolution of young Sun-like stars like HL Taurus and R Monocerotis suggests that the disk had become planets and planetesimals, clear of gas and dust. The noble gases in the Earth imply the final, collisional accretion in which the planets grew to their current sizes took place after

the nebula was cleared away by the Sun's activity: many small planetesimals were swept up into the growing planets (Taylor 2001).

A large fraction of the planetesimals were scattered in this post-disk time by encountering the gravitational field of the planets: their orbits' inclination, eccentricity and semimajor axis were decisively shifted (Tsiganis et al. 2005). Most were ejected to the interstellar medium. Between 1 and 10 percent were thrown out at velocities in the narrow window where their ejection speed was less than the local Solar System escape speed: only these orbits were then vulnerable to the subtle influence of galactic tides and perturbations from passing stars. These lifted the scattered planetesimals' perihelia far beyond planetary influence and circularised their orbits. This group form the Oort cloud of comets (Jewitt 2010). Most comets have remained with perihelia permanently beyond fifty thousand AU; we see a tiny disturbed fraction that drop towards the Sun into planet-crossing orbits, which lower their perihelia to a mere < 5 AU. From these, the total Oort population is extrapolated to number $(1 - 3) \times 10^{11}$ (Francis 2005).[4]

In the many succeeding millennia, the constant repetitive scattering of planetesimals slowly shifted the orbits of the giant planets themselves, through the accumulation of the minute angular momentum exchanges of each encounter (Tsiganis et al. 2005). This restructuring of the Solar System architecture was aided by various pairs of the giant planets reaching mutual orbital resonances at various times, which drove new divots of scattering into the stable regions of planetesimal orbits.

Not all worlds were lost to the mass scattering: discrete populations of minor planets remained, often preserved by being in orbits with parameters that were shielded from the scattering. With their slow-evolving orbits, they are fossils of the protoplanetary time.

However, these minor planets are not exclusively grouped in low-inclination, near-circular orbits, as might be expected from populations preserved from even a flared protoplanetary disk (Gomes 2009). The modern trans-Neptunian populations are a highly sculpted artefact. They display a split between a major near-flat and a minor highly inclined population, with the most populous group truncated at near 48 AU. There is also significantly less mass in the overall population than Solar System formation models would lead us to expect (Gomes 2009).

We therefore examine the current orbits of these populations to understand the gravitational influences that shaped them. These orbital structures contain three potential levels of information: the "primordial" trans-Neptunian population formation state; how it was influenced as the planetary architecture rearranged into its current state (Morbidelli et al. 2008) and how it has evolved under the current architecture (Volk & Malhotra 2011). From the present orbits of these small worlds, we chart the course of the ancient movements of the planets.

1.2. The modern dynamical populations beyond Neptune

Our present understanding of the current orbits of the known objects beyond Neptune is that they fall into several distinct populations: the nomenclature of these groups are

[4]Down to an absolute magnitude of $H = 11$: $H \gtrsim 10$ corresponds to a nuclear radii less than about 1 km.

determined by their orbital parameters. These include both the standard Keplerian orbital elements and several derived parameters, defined below.

For an object that is mutually interacting with a planet and with the Sun, the degree of interaction or perturbation by the planet on the much less massive object's orbit can be quantified by the Tisserand parameter (Tisserand 1890): the interactions relevant here are those of an object with an orbit with semimajor axis a, inclination i, eccentricity e, with respect to either Jupiter, for distinguishing objects coupled to Jupiter like Jupiter-family comets, or Neptune, sometimes used for distinguishing objects scattered by Neptune (Elliot et al. 2005).

$$T_{planet} = \frac{a_{planet}}{a_{tno}} + 2\cos i_{tno}\sqrt{(a_{tno}/a_{planet})(1-e_{tno}^2)} \tag{1.1}$$

This is a constant of motion in the frame of the restricted three-body problem where the reference plane is relative to the planet.

Also of use in such classification is the sphere of dominant gravitational influence, or Hill sphere, of a planet, where its gravitational influence dominates the tidal influence of the Sun. For objects in the outer Solar System, the relevant Hill sphere is Neptune's, 0.776 AU in radius, the largest of any planet in the Solar System due to being furthest from the Sun. The radius r_H of a Hill sphere of a planet with mass m_P and an orbital semimajor axis a_P orbiting the Sun, which has mass $M_\odot$, is given by (Hill 1879):

$$r_H = a_P\left(\frac{1}{3}\frac{m_p}{m_p + M_\odot}\right)^{1/3} \tag{1.2}$$

Closest to the Sun, the **Centaurs**, which are considered a TNO population (Gladman et al. 2008), have perihelia $q_{Saturn} < q_{Centaur} < q_{Neptune}$ and $q_{Centaur} > 7.35$AU; or perihelia and semimajor axes between the orbits of Jupiter and Neptune (5.2–30 AU). They are a dynamically unstable group: under the strong gravitational influences of the giant planets, their orbits are evolving so rapidly that they can be lost entirely within the space of only ten million years. Once their orbits dip into the region of the terrestrial planets, they are seen as Jupiter-family comets. Centaurs may originate in the population of objects that have encountered Neptune, or in the chaotic zones near mean-motion resonances.

Surrounding the Lagrange points of Neptune are the **Neptune trojans**, which may either have formed or have been captured into these stability points: their matched semimajor axis with Neptune left them vulnerable to its past migration. There are expected to be 50-350 objects larger than 40 km in each Lagrange point (Sheppard & Trujillo 2010).[5]

The **Kuiper belt** sits between 35 and 48 AU, in orbits where they do not gravitationally encounter Neptune. Kuiper belt objects (KBOS) are divided into two populations, by whether they are on orbits in resonance with Neptune. The **classical KBOS**[6] are not resonant; even at perihelion, they are always well separated from Neptune, with Tisserand parameter > 3, $e < 0.24$, $a_{Neptune} < a_{KBO} < 2000$ AU (after Elliot et al. (2005) and Gladman et al. (2008)).[7]

[5] The MPC reports six at the L4 point and three at the L5 point as of 4 December 2012.

[6] Also "cubewanos", after the first discovered, 1992 QB1.

[7] Elliot et al. (2005) and Gladman et al. (2008) put the e cutoff at slightly different places; Gladman et al. (2008) does not use a Tisserand parameter; Elliot et al. (2005) do not use a semimajor axis cutoff to exclude detached objects.

Those KBOs in main mean motion resonances with Neptune are identified by that resonance; for example, (134340) Pluto is in the 3:2 resonance (the "plutinos"). Such **resonant KBOs** have eccentricities roughly $0.1 < e_{KBO} < 0.3$ (Gladman et al. 2008). Exact identification of whether objects are within the higher-order resonances like the 12:7 can be difficult, requiring many cycles of numerical integration of the object's orbit to determine membership, as objects diffuse in and out of such weak resonances over the lifetime of the Solar System. The classical KBOs are the most numerous population. The resonant KBOs are rarer, but outnumber the scattered TNOs, which even after a decade of surveying remain the sparsest population.

The **scattered or scattering disk**,[8] (Torbett 1989) are objects on orbits that have encountered Neptune; as a region, it encompasses the orbital space that can be visited by bodies that have encountered Neptune within the radius of a Hill sphere(Morbidelli & Brown 2004). This region also sources the short-period comets. The orbits of scattered disk objects (SDOs) evolve over time scales that can be as long as the age of the Solar System. The orbits of the scattered disk overlap spatially with those of the detached objects, which have orbital perihelia, their closest approach to the Sun, more distant than they could be placed by scattering from Neptune. Objects can be within SDO space that are in a high-order (weak) resonance with Neptune.

Detached objects[9] have a broad spectrum of differing descriptions: however, their defining feature is $q > 50 - 70$ AU. This "lifted" perihelion cannot be produced by interaction within the planetary region, and requires another origin, such as scattering by an unknown planet, or perturbation by a stellar encounter, either within or after the Sun's birth cluster dispersed (Brown et al. 2004). These objects are close enough to the Sun that the Galaxy's gravitational tides are not their primary influence.

Well beyond this is the realm of comets. Beginning beyond 20-50,000 or more AU, the **Oort cloud** is so remote that its dominant perturbing influence is the gravitational tides of the Galaxy, and its members are so small and faint that they cannot be observed, except when one is disturbed and enters the planetary realm as a comet (Morbidelli 2005).

Both the relative abundances and the orbital parameters of these trans-Neptunian populations are needed to tell the story of their origins. Each population cluster must have an origin, and providing a uniform explanation for each has proved difficult. Are these populations primordial, or have they been placed in their current locations at a time after the Solar System formed? Over the last two decades, the evolutionary scenarios have shifted from proposing the emplacement of the KBOs by the smooth migration of Neptune (Malhotra 1995) to the more violent scattering events driven through abrupt ice giant migration that are postulated in the Nice model (Levison et al. 2008).

The inner truncation of the Kuiper belt occurs distinctly at the 1:2 resonance point with Neptune. Dynamical stirring took place to push the classical KBOs into their current ranges, which are an order of magnitude larger than those that could be produced by only a mutually gravitationally stirred primordial disk. This is preserved in the inclination distribution of the populations. Brown (2001) recognised the separation of the KBOs into a near-flat "cold" population and a highly inclined and thus dynamically "hot" population. Lack of

[8] Or scattered Kuiper belt objects (Jewitt et al. 1998).

[9] This population are also called inner Oort cloud objects (Brown et al. 2004), extended scattered disc objects (Gladman 2002), distant detached objects (Gomes et al. 2006) or scattered-extended (Elliot et al. 2006).

dynamical excitation is used as a strong argument for a dynamically primordial nature. Most KBOs are found within $10 \pm 1^\circ$ of the invariable plane, the plane of average angular momentum in the Solar System (Brown & Pan 2004).

The cold classicals sit between this 1:2 resonance and the 3:2 of the plutinos, with semimajor axes of between 39.4 and 47.8 AU. Teasing out whether there is structure within the cold classicals has been a question for over a decade: Petit et al. (2011) concluded that there is a core of dynamically undisturbed TNOs within the population of these non-resonant objects. This "kernel" must have been left untouched by the resonance sweeping of Neptune's migration. It is not retained by N-body models that try to form the population with a smooth migration of Neptune; Batygin et al. (2011) can preserve it through requiring a rapid precession of the longitude of the ascending node of Neptune.

The cold classicals can also be preserved if the Solar System initially contained five multi-resonant giant planets: the two gas giants and three ice giants. Recent studies suggest that this architecture more favorably evolves to the configuration of the present day than a four-planet system (Nesvorný 2011), and avoids destructive excitation of the cold classicals if one of the ice giants is ejected early in the dynamical evolution of the system (Batygin et al. 2011).

A surprisingly high proportion of the smaller population of TNOs are binary systems: up to 20% in the cold classicals and 5-10% elsewhere (Stephens & Noll 2006; Noll et al. 2008). The binaries that are resolved generally have very wide separations (Parker & Kavelaars 2011). These are incredibly fragile systems: if they were located in the inner Solar System, gravitational perturbations from the planets would rapidly break the binaries apart. In addition, the mass ratio in the resolved systems are surprisingly equal, suggesting that the binary components had a common formation: with TNOs too sparse in the present to form binaries through gravitational capture, perhaps they are direct remnants of the formation of planetesimals in binary or trinary clusters (Nesvorny et al. 2010). The abundant nature of these delicate systems suggests that their host population is ancient (Parker & Kavelaars 2010b).

All the other TNO populations have experienced significant dynamical evolution, so there are many aspects which remain to be explained. For example, the Kuiper belt truncates; this is unexpected when the Solar System is compared to observations of younger planetary disks around solar-mass stars, where the disks can extend to hundreds of AU. Suggested causes include tidal disk truncation by a passing star, which may also have provided the dynamical excitation of the hot KBO population, but it is also possible that no larger bodies grew in the outer reaches. Observations will help in resolving this, by confirming the number of large distant objects.

The population density of the scattered and extended scattered disks is at present mysterious. Some objects in the extended scattered disk have been identified, such as 2004 XR_{190}, but inner Oort cloud objects are currently only known from (90377) Sedna and 2000 CR_{105}. These distant objects appear too large (300-2000 km) to have accreted at their present location, given the low density of the protoplanetary disk at these distances.

N-body simulations of the protoplanetary disk show that the gravitational potential of the gas disk excites Kozai oscillations in the scattering planetesimals, such that the distribution

of the scattered disk depends on the shape of the profile of the gas disk (Kretke et al. 2011). The high-inclination population that is observed therefore limits the mass of the early gas disk. The currently-known relatively small size of the high-inclination population pushes the mass of the disk downward; however, this population fall on a region of the sky that has not been well mapped. Surveys of this population will constrain the size of the protoplanetary nebula at the time of the formation of Jupiter (Kretke et al. 2011).

The significantly higher inclinations of almost all the largest TNOs is an outstanding puzzle for TNO population formation models. The inclination of a smaller object's scattering from an ice giant is not dependent on the mass of the object, yet the dwarf planets are not evenly distributed in inclination (Brown 2008).

1.3. The importance of surveys

At the beginning of the twentieth century, the outer reaches of the Solar System, including the source of comets, were not understood. Eight planets were known: a ninth body, beyond Neptune, was thought necessary due to mistaken measurements of the orbit of Neptune. A "Planet X" would provide the necessary perturbations to Neptune's orbit.

Todd (1880) made the first serious search for a planet beyond Neptune, examining by eye a 2-by-50 degree strip along the invariable plane with the 26" USNO refractor. Although he reported "I have much confidence in this telescopic search…there should be no pressing need of duplicating it.", his method of searching visually for a perceptible disk made checking even 13th magnitude stars "quite out of the question" (Tombaugh 1961).

The search clearly required better technology. Lowell tried small photographic surveys between 1906 and his death in 1916, but it was not until a 13" was commissioned at Lowell Observatory in 1929 that a photographic survey began in earnest. Tombaugh (1946, 1961) pioneered the technique used for detection of slow-moving objects: take multiple images of a large field, some time apart, and examine each point of light to see if any have shifted in position.

Working with the 13", a blink comparator and pairs of 12 x 14 degree photographic plates, taking images hours apart, with a third image about two days later, Tombaugh and collaborators observed primarily within 15 degrees and no further than 25 degrees from opposition. The image on the third night gave the survey a motion sensitivity of out to 400 AU and excluded asteroids closer than Saturn. As they moved to higher ecliptic latitudes, the temporal spacing of the images was increased proportional to the secant of the ecliptic latitude (Tombaugh 1961), though the maximum span of the three observations was kept at a week. The survey fields were overlapped to provide sensitivity to Saturn-interior Centaurs with orbital inclinations of up to 15 degrees, and more distant objects of higher inclination. This survey ran until 1945.

Tombaugh successfully identified one object: Pluto. Unfortunately, Pluto was close to the predicted location of a perturber of Neptune; this meant that it was immediately thought to be on the order of a terrestrial planet in size. The true size and composition of this world were not established until the detection of its satellite Charon by Christy & Harrington (1978), which then showed that Pluto was only equal in diameter to roughly the size of

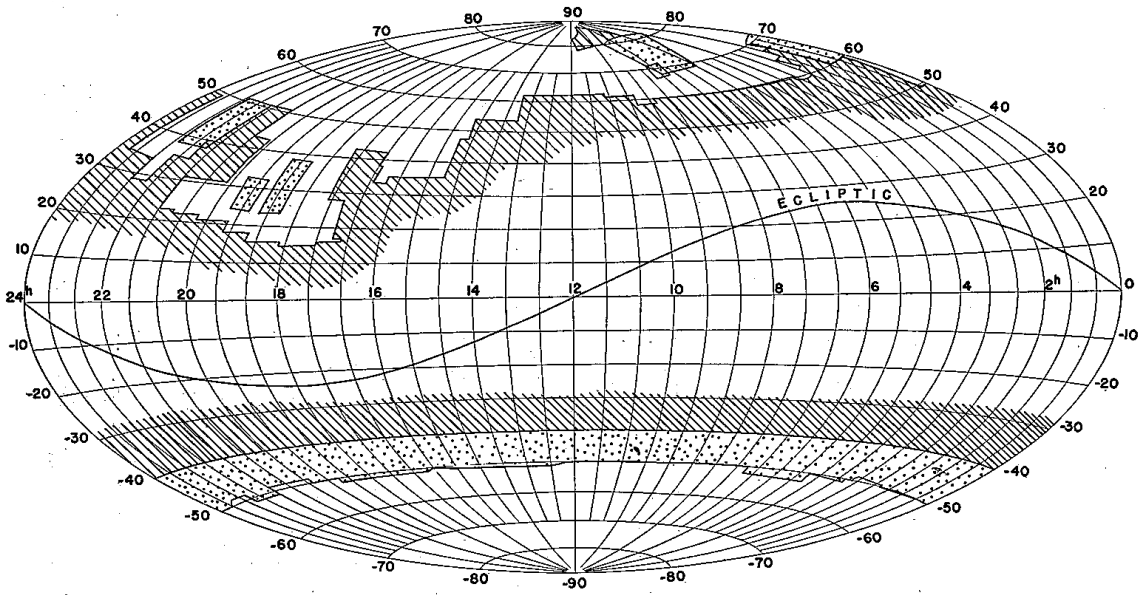

Figure 1.1 The sky coverage of Tombaugh (1961) from surveying for TNOs between 1929 and 1945: the shading indicates estimated limiting magnitudes. White area around the ecliptic: mag 17; crosshatch: mag 16-17; stipple: mag 14-15, with uncertainties of up to 0.5 mag. Declination ranges beyond the stipple were not observed.

Western Australia, and had the density of ice with a little rock. Pluto was discovered with a supposedly non-optimal six days between the second and third observations (Tombaugh 1961).

Tombaugh's survey was practically complete down to 17th magnitude for three-quarters of the sky, covering about 30,000 square degrees (Figure 1.1). They did examine an additional 1530 deg^2. area along the ecliptic, 7.5 hrs of RA long, to 18th magnitude (Tombaugh 1961).

The magnitude and spatial completeness of this survey, and the painstaking labour involved in surveying by hand with the technology of photographic plates, meant that few further surveys were undertaken in the succeeding decades. The Solar System remained as seen in Fig. 1.2); "[i]n the modern era of software analysis, one can only hold in awe the diligence and expertise of those researchers engaged in this work." (Fitzsimmons 2000).

Following Leonard (1930)'s optimism that further Pluto-like objects would soon "come to light", the likelihood of there being numerous other TNOs was taken up by Edgeworth (1943, 1949), who suggested that there would be a cloud of such objects, but it was his contemporary Kuiper's (unciting) review in 1951, suggesting a distant belt, that gained greater attention. Neither astronomer had a physical model of formation or predicted the distribution of orbits in this region; however, Kuiper's name is now used for the population between 38 and 45 AU (§ 1.1).

The lack of interest in the outer structure of the Solar System saw the field languish through the 1950s and 60s. This underwent a gradual shift in the 1980s. Fernandez (1980) revisited the ideas of Edgeworth and Kuiper in an effort to explain the flux of short-period comets (Joss 1973), while Duncan (1988) showed that these comets could not originate from a spherical source population, due to the low inclination of their orbits. This work supported the existence of a flattened "belt" at 40-50 AU, a population distinct from the inner part of Oort's exceedingly remote cloud with semimajor axis $\sim 10^4$ AU (Marsden et al, 1978) that

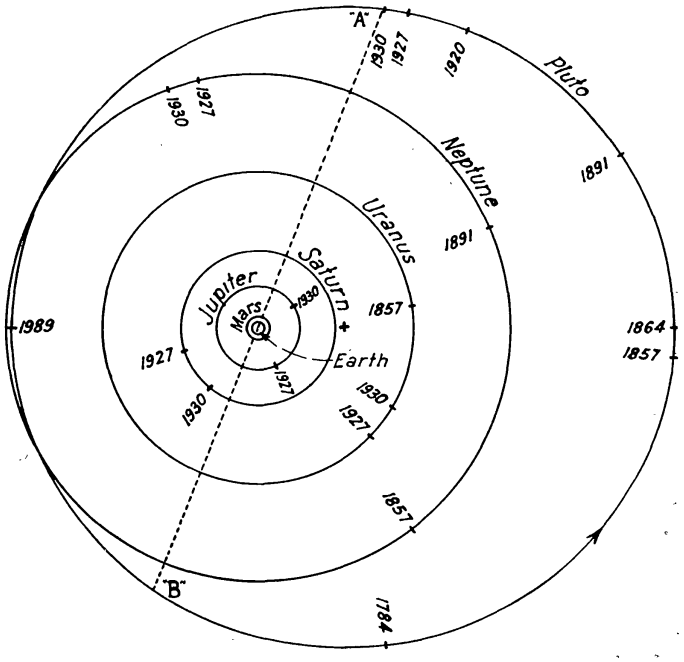

Figure 1.2 The Solar System as depicted by Leonard (1930) after the discovery of Pluto: the innermost circle is Earth's orbit.

was the source of comets.

There were complementary observational efforts. Kowal et al. (1979) made a photographic plate survey at Palomar in the late 1970s, leading to the discovery of the first Centaur, (2060) Chiron. This survey searched 6400 deg^2. down to $m_r \sim 18.5$. The final such survey by Luu & Jewitt (1988) unsuccessfully surveyed 297 deg^2 down to $m_r \sim 19.0$.

This changed with the development of CCD cameras in the late 1980s (Table 1.1). These detectors offered a linear response to incident light, up to their point of saturation, and were very efficient at converting this received flux to signal. However, they could only be manufactured with painfully small surface areas. This limited their utility for wide-field surveys for nearly another decade, but a few astronomers made immediate use of them for small-scale TNO searches. A number of researchers made pilot digital surveys with a mix of hand and computer-blinked analysis techniques in the late 1980s and early 1990s, though all were unsuccessful (Luu & Jewitt 1988; Kowal 1989; Levison & Duncan 1990; Cochran et al. 1991; Tyson et al. 1992).

The perseverance of Jewitt & Luu (1993) in a subsequent larger survey brought their discovery of (15760) 1992 QB_1.[10] This heralded the age of discovery of the Kuiper belt. 1992 QB_1 was followed by nearly a hundred more Kuiper belt objects in the next six years (Fitzsimmons 2000), and the first scattered disk object, 1996 TL_{66} (Luu et al. 1997). These were found through a scattering of small but quite deep optical surveys, most in the Northern Hemisphere (Jewitt & Luu 1995; Jewitt et al. 1998) (Table 1.1).

[10] 1992 QB_1 has subsequently turned out to be a rather uninteresting medium-small (H = 7.2) cold classical object with a featureless spectrum. Classical objects are however sometimes referred to as "cubewanos" in its honour.

Table 1.1 TNO surveys up to mid-2000

Survey (if named)	Facility	Area (deg^2)	m_{50}	Reference
EROS-2	La Silla 1.5	30.0	$\sim 19.0\ I$	P. Tisserand (pers. comm.)
QUEST	Llano del Hato 1.0	66.8	20.0	Rabinowitz & Team (2000)
sKBO	CFHT/12K	20.2	23.7	Trujillo et al. (2000)
sKBO	UH 2.2/8K	51.5	22.5	Trujillo et al. (2000)
unpublished	La Silla 2.2	1.6	24.0	Delsanti et al. (1999); Boehnhardt & Hainaut (2000)
	KECK/LRIS	0.01	27.9	Chiang & Brown (1999)
	SSO 40″	12.0	21.0	Brown & Webster (1998)
JL Deep	Keck	0.3	26.3	Luu & Jewitt (1998a)
	CFHT/UH8k	51.5	23.4	Gladman et al. (1998)
	Palomar 5	0.049	25.6	Gladman et al. (1998)
	Palomar 5	0.075	25.0	Gladman et al. (1998)
	CFHT/UH8k	51.5	22.5 VR	Jewitt et al. (1998)
Pluto-Express	CFHT/12k	2.22	23.1	Trujillo & Jewitt (1998)
MKCT	UH 2.2	3.9	24.2	Jewitt et al. (1996)
MKCT	CTIO 1.5	4.4	23.2	Jewitt et al. (1996)
	HST/WFPC2	0.001	27.9	Cochran et al. (1995); Brown et al. (1997); Cochran et al. (1998)
	WHT	0.7	23.5	Irwin et al. (1995)
	UH 2.2	1.2	24.8	Jewitt & Luu (1993, 1995)
	INT 2.5	0.7	22.5	Williams (1995)
unpublished	McDonald 2.7	unknown	unknown	Cochran et al. (1991)
	Flagstaff 40″	4.9	21.0	Levison & Duncan (1990)
	KPNO 1.3	0.338	24.0	Luu & Jewitt (1988)
	KPNO 0.6/CTIO 0.9/plate	297.0	19.5	Luu & Jewitt (1988)
unpublished	unreported	0.01	24.9	Tyson et al. (1992)
	Palomar 48″/plate	6400	18.5	Kowal (1989)
	Lowell 13″/plate	1530	18.0?	Tombaugh (1961)
	Lowell 13″/plate	30000	16.8?	Tombaugh (1946, 1961)
	26″ USNO refractor/eye	100	10.0?	Todd (1880)

[a] Expanded from Kavelaars et al. (2008a) and Brown & Webster (1998). Facility refers to telescope name/aperture and dimensions of CCD array of camera. Survey limiting magnitude is normally given at m_{50}, the magnitude at which the detection efficiency of TNOs drops to 50%.

Table 1.2 TNO surveys from mid-2000 up to December 2013

Survey (if named)	Facility	Area (deg^2)	m_{50}	Reference
LSQKBO	La Silla 1.0	~ 7500	21.5	Rabinowitz et al. (2012)
OCKS	Las Campanas 1.3	~ 2500	21.6	Sheppard et al. (2011)
	HST/ACS	1.83	26.43	Fuentes et al. (2011)
	HST/ACS	0.45	26.1	Fuentes et al. (2010)
HELE-CFEPS	CFHT	480.0	23.9 g'	Kavelaars et al. (2008b), J.J. Kavelaars (pers. comm.)
CFEPS	CFHT	321.0	23.5–24.4 g	Kavelaars et al. (2009); Petit et al. (2011)
PDSSS	Palomar 1.2	11786.0	21.3	Schwamb et al. (2009, 2010)
	Subaru/Suprime	0.26	26.8	Fuentes et al. (2009)
SDSS Stripe 82	Sloan	300.0	22.6 r	unpublished; cf. Kaib et al. (2009)
	Subaru/Suprime	0.3	26.8	Fraser & Kavelaars (2009)
	Subaru/Suprime	2.8	25.7	Fuentes & Holman (2008)
	CFHT/Blanco	3.0	26.4	Fraser et al. (2008)
ESSENCE	CTIO Blanco	11.52	23.7	Becker et al. (2008)
Spacewatch	KPNO 0.9	7790.6	21.0 (rate dependent)	Larsen et al. (2007)
Irregular Satellites	CFHT/12K	11.85	24.0	Petit et al. (2006)
DSS NGS-POSS I	Palomar 1.2	4992.0	unpublished?	Rhoads (2005)
DES	KPNO/CTIO 4.0	550.0	22.0	Millis et al. (2002); Elliot et al. (2005)
	HST/ACS	0.02	28.5	Bernstein et al. (2004, 2006)
Caltech Wide Area	Palomar 1.2	19389.0	20.5	Trujillo & Brown (2003); Brown (2008)
	CTIO	1.50	25.5	Allen et al. (2001)
	KPNO	2.3	24.9–25.4	Allen et al. (2002)
SDSS	Sloan	100.0	21.5	Ivezic et al. (2001)
KPNO-Large	KPNO 0.9/Mosaic	164.0	21.1	Trujillo et al. (2001b)
	CFHT/UT1	0.31	25.93	Gladman et al. (2001)
CFHT	CFHT	73.0	23.7	Trujillo et al. (2001a)
Spacewatch	KPNO 0.9	1483.5	21.5	Larsen et al. (2001)
SEKS	Mt Stromlo 1.3	2900.0	19.5	Moody et al. (2003); Moody (2004)
Baker-Nunn	APT 0.5	1428.0	18.8	Sheppard et al. (2000)

[a] Updated/expanded from Kavelaars et al. (2008a) and Brown & Webster (1998), excluding occultation surveys, whose discoveries are inherently irretrievable. Facility refers to telescope name/aperture and dimensions of CCD array of camera. Survey limiting magnitude is normally given at m_{50}, the magnitude at which the detection efficiency of TNOs drops to 50%.

These surveys (Table 1.1) were hampered by their small area: at the time the 52 sq deg of Jewitt et al. (1998) was "huge" (Fitzsimmons 2000), though the total area of the sky is 41,253 sq degrees.

The natural constraint on the length of integration between obtaining the optimum signal-to-noise (s/n) and preventing trailing provides an inherent limit to the depth of survey of a 2 m-class telescope, of $m_r \approx 24$ (Fitzsimmons 2000). This led to the development of the "shift and add" stacking techniques, where multiple exposures are restacked along possible TNO motion vectors and coadded to try to get a TNO to pop out as a point source among the trailed distant galaxies and stars. This technique is often used in the narrow-field or "pencil-beam" surveys which reach much fainter magnitudes (Parker & Kavelaars 2010a).

The new availability of both the Hubble Space Telescope (HST) and telescopes in the 8-10 m class led to an enthusiastic push to the greatest possible depths, and to a division of surveying into two groups: the pencil-beam surveys and the all-sky surveys (Table 1.1, 1.2). The small-area deep surveys sample the small-diameter end of the population distribution. They have assessed the TNO population to very small diameters: Bernstein et al. (2004) checked down to m_r 28.5 with HST (Bernstein et al. 2006), while Fraser et al. (2008) obtained 72 KBOs from a magnitude-limited search between $m_{g'}$21–26.4 in only 3 deg^2.

The shallower all-sky surveys measure the bright end of the population and characterise the overall sky density, particularly for the rarer TNO populations. Even in the 1960s, Tombaugh (1961) looked ahead hopefully to a search "to the twentieth magnitude", which he saw as being quite plausible with the then-new, optically faster design of Schmidt telescope, and suggested that it be tried with the 48" Schmidt telescope at Palomar[11]. From the late 1990s, successive wide-field surveys at Palomar Observatory including Trujillo & Brown (2003) and Schwamb et al. (2009, 2010) used exactly this telescope with a modern digital imager (Table 1.2). They produced a fruitful crop of TNOs, including many dwarf planets, found in all dynamical classes.

In addition, the Deep Ecliptic Survey (DES) (Millis et al. 2002; Elliot et al. 2005) surveyed 550 deg^2 to m_r 22.5 and Spacewatch (Larsen et al. 2001, 2007) helped populate the relatively small and faint KBO population, which rapidly increased in number.

There have been attempts to explore the mid-depth population, fulfilling both the constraints of magnitude depth and sky coverage. The most comprehensive work in this area has been the Canada-France Ecliptic Plane Survey (CFEPS) survey on CFHT. This four-year survey carefully worked through 321 sq.deg. of the ecliptic to depths in the range m_{AB} 23.5-24.4, with comprehensive followup of their 169 discoveries (Petit et al. 2011).

CFEPS also made a small subsurvey for a high ecliptic latitude extension, HELE-CFEPS (Kavelaars et al. 2008b), which led to the discovery of the first few "perpendicular" objects in the Solar System, with retrograde orbits with inclinations of just past ninety degrees. These objects remain particularly puzzling, as straightforward scattering from the giant planets is insufficient to place them on such high-inclination orbits, and their orbits are not

[11]It is interesting to ponder that Luyten's work in the optical with the Palomar Sky Survey of the 1950s for his massive parallax-measuring project was with a plate measuring machine that used colour illumination of the plates to show unmatched objects statically, rather than through blinking. J. Larsen notes "I suppose the difficulties in approaching Luyten to ask to use it would have made its applicability for planetary astronomy limited. Oh, but the possibilities…"

stable enough over Solar System lifetime timescales for them to be on "primordial" paths. However, this survey remains one of very few to sample the high-latitude areas of the sky that contain the potential high-inclination trans-Neptunian population.

In 2013, over 1600 TNOs were known: the majority are in the Kuiper belt. These modern wide-field and pencil-beam surveys have allowed the dynamical properties of the trans-Neptunian region to be mapped, first in broad-brush strokes, but in ever-increasing detail. We turn now to the contributions made from surveying the southern sky.

1.3.1. Previous surveys in the Southern Hemisphere

Throughout the development of the field, work in the Southern Hemisphere has been limited, as most of the band within 10 degrees latitude of the ecliptic is visible from the Northern Hemisphere (Fig. 1.3). There were a few early surveys in the south. A survey in Chile at La Silla (Boehnhardt & Hainaut 2000) covered a very small amount of sky, and made no discoveries (Delsanti et al. 2000), but continued to be unsuccessfully proposed for a few successive years (Boehnhardt & Hainaut 2002). A Venezuela survey by Rabinowitz & Team (2000) at the 1 m Schmidt at Llano del Hato, part of a quasar and transient survey, twice drift-scanned 66.8 deg^2 centered at RA = 13.3 h, Dec = -1.1 deg at a 4-hour separation, discovering one object (2000 EB_{173}).

Three surveys have been previously made in Australia. 12 square degrees were observed to a limiting magnitude of $m_R \sim 21.0$ by Brown & Webster (1998) with the Siding Spring 40-inch telescope near the ecliptic between April 1995 and April 1997, with one potential Centaur detected. Sheppard et al. (2000) used the UNSW Automated Patrol Telescope at SSO for surveying 1,428 deg^2 to $m_R = 18.8$, observing one previously discovered Centaur, 1997 CU_{26} (Chariklo), and also kept their fields very close to the ecliptic. The EROS-2 survey monitored ~ 88 deg^2 of the Large Magellanic Cloud, 10 deg^2 of the Small Magellanic Cloud and about 100 deg^2 toward the Galactic Bulge (mainly at Galactic latitude $-2 < b < -6$) over 6.7 years to $m_I \sim 20$. 30 deg^2 of the closest fields to the ecliptic have been image subtracted for TNOs, with no detections, at an estimated detection efficiency of 50% for $I \sim 19$ (P. Tisserand, pers. comm.).

The previous major Australian-based survey of Marshall et al. (2001) had planned to cover the entire southern sky, with the MACHO survey's Great Melbourne Telescope. They had only surveyed ~2,900 deg^2 around the ecliptic before the telescope and the reduced survey data were destroyed in the Canberra bushfires of 2003 (Moody et al. 2003).[12] None of the few detections made in this survey (Moody 2004) were subsequently successfully observed again for recovery and determination of their orbits, so they are considered lost.

In recent years, since the beginning of this thesis, two other surveys have commenced operation and searches for TNOs in the Southern Hemisphere (Table 1.2). The Yale survey uses the former QUEST survey camera (Schwamb et al. 2009) on the La Silla 1.3 m telescope, to a limiting magnitude of ~ 21.5 (Rabinowitz et al. 2012). The OGLE-Carnegie survey uses a 1.3 m telescope at Las Campanas, using the OGLE data to obtain a limiting magnitude of 21.2 to 21.6, and runs a full subtraction pipeline on their survey area of ~ 2500 deg^2 of part

[12] The original data survive, and have been the source of several publications on Cepheids.

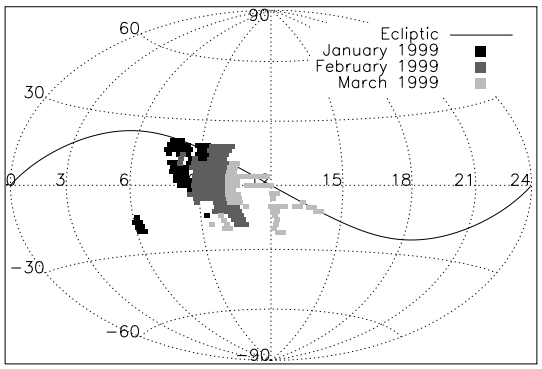

(a) Sheppard et al. (2000): 1428 deg^2 to m = 18.8.

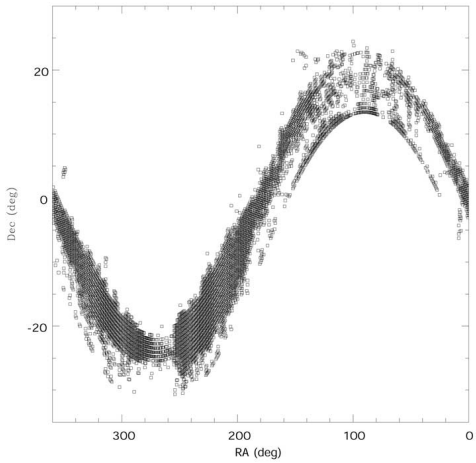

(b) Moody et al. (2003): 500 deg^2 to m = 19.5 (2900 deg^2 reported in Moody (2004)).

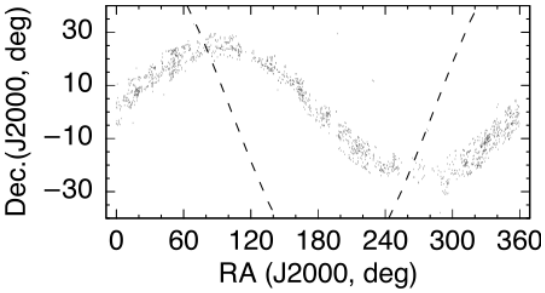

(c) Deep Ecliptic Survey (Millis et al. 2002; Elliot et al. 2005): 550 deg^2 to m = 22.0

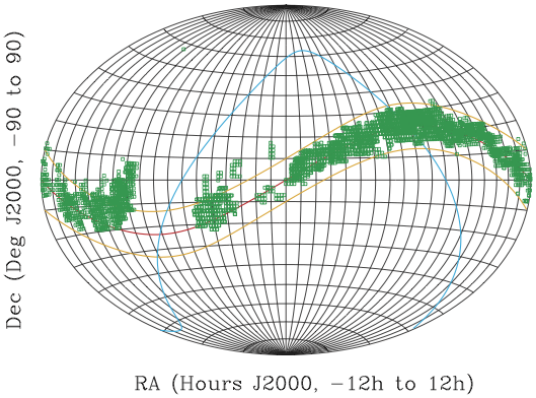

(d) Spacewatch slow-moving (Larsen et al. 2007): 7790.6 deg^2 to m = 21.0.

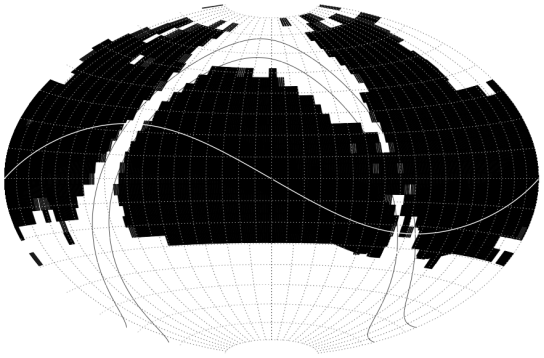

(e) Palomar (Trujillo & Brown 2003; Brown 2008): 19389 deg^2 to m = 20.5.

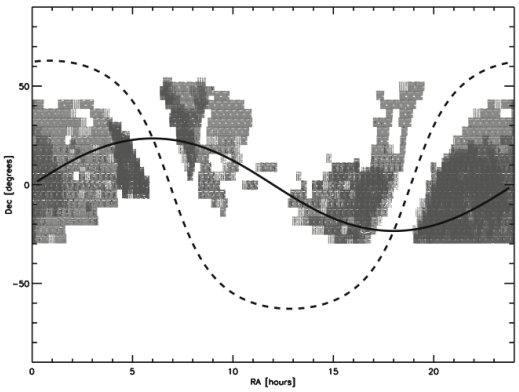

(f) Palomar Distant (Schwamb et al. 2009, 2010): 11786 deg^2 to 21.3.

Figure 1.3 Wide-field digital TNO surveys greater than 500 deg^2 up to 2009, when this work began; Larsen et al. (2001) (1483.5 deg^2 to m = 21.5) is omitted as Larsen et al. (2007) overlaps its coverage. Note the lack of southern surveying.

of the galactic plane and regions south of declination -25 that are near the ecliptic (Sheppard et al. 2011).

1.3.2. Requirements for detecting moving objects

Filter-wise, the sky is darker at V, but the CCDs used in digital cameras have higher efficiency at R, so the signal to noise is better in R, and the filter avoids bright emission lines from atmospheric OH that occur at longer wavelengths (Jewitt & Luu 1995); most surveys keep to a variant of this filter.

To detect moving objects in the Solar System, a piece of sky must be repeatedly imaged: three observations will provide the definition of an orbit. The stars provide a fixed background, and the moving object changes position in successive images. The two main classes of moving objects that will be detected, asteroids and TNOs, have quite different characteristics. We wish to detect TNOs, and avoid the far more numerous asteroids.

Opposition, the point relative to the observer on the Earth that is opposite the location of the Sun in the sky, is on the meridian at midnight and moves eastward at about 30 degrees per month. When at opposition, all Solar System objects exhibit apparent westward motion, proportional to their heliocentric distance. This apparent motion is due to the Earth also orbiting the Sun, at a higher velocity than the more distant objects, following from the Keplerian nature of the gravitational potential. The objects at opposition are both fully illuminated and at minimum geocentric distance. If we assume that both Earth and TNO are on concentric coplanar orbits, the rate of motion $d\theta/dt$ on the sky of an object at geocentric distance Δ (AU) and heliocentric distance r_H (AU) observed near opposition is given by (Luu & Jewitt 1988):

$$\frac{d\theta}{dt} = \frac{v_{Earth} - v_{\text{TNO}}}{1.5 * 10^8 \Delta} \tag{1.3}$$

where $d\theta/dt$ is in radians per second, v_{Earth} is the Keplerian velocity of the Earth ($\sim$ 30 km/s), v_{TNO} is the Keplerian velocity of the TNO. $d\theta/dt$ for TNOs where $r_H >> 1$, can instead be equivalently given in arcsec per hour as per (Fraser et al. 2008):

$$\frac{d\theta}{dt} \sim 147.8\text{AU} \left[\frac{1}{\Delta} - \frac{1}{r_H^{3/2}} \right] \tag{1.4}$$

or equivalently (Brown & Webster 1998):

$$\frac{d\theta}{dt} \approx 147.8\text{AU} \frac{\cos\omega}{r_H} \tag{1.5}$$

where ω is the angle from opposition, such that almost all the object motion is a reflex effect from the Earth's motion.

The alternative location for observation is at quadrature, along the Earth's orbital motion vector, which produces apparent motion that is only due to the object's orbital motion in the plane of the sky. In this case its rate of motion in arcsec per hour is similarly given by (cf. Fraser et al. (2008) formulation):

$$\frac{d\theta}{dt} = \frac{147.8}{r_H^{3/2}} \tag{1.6}$$

for objects on circular orbits.

At opposition, TNOs will have their greatest rate of motion: Centaurs at $5 < R < 30$ AU have $4 < d\theta/dt$ (normally they move at up to 15″/hr), and other objects > 30 AU have motion rates of a few arcseconds per hour: KBOs at 40 AU move at ∼ 3″/ hr at opposition. This trans-Neptunian motion is detectable over a single night, and can be used for initial detection of TNOs and for positive identification of known TNOs in follow-up observations where the size of the orbital element error ellipse is large.

In contrast, asteroids will be at their slowest rate of motion. Away from opposition, those inward of ∼ 5 AU move swiftly: rates of 100″ per hour are quite common. Therefore, for most efficient detection, TNOs should be observed as close to opposition as possible; but asteroids near their stationary points can then be confused with TNOs.

Increasing the spacing of observations to occur over more than one night will remove the confusion with asteroids, whose motion will swiftly pick up again. This multi-day spacing of discovery and followup observations is the key to a successful survey for outer Solar System objects. There is a level of finesse in setting the exact spacing of observations, so determining the optimum spacing of the observations for discriminating and identifying TNOs is the first task in survey design.

The spacing of observations leads directly to the efficiency of object detection of the survey as a function of heliocentric distance. The short cadence of near-Earth asteroid surveys also permits them to detect Centaurs, but the normal intranight processing which they make for surveying leaves them unable to see TNOs, eg. Spacewatch discovered five of the first nine Centaurs as a result (Larsen et al. 2001). Most TNO surveys are able to pick up distant Centaurs; those in closer than 10 AU may not be adequately sampled in this way, as different surveys have varying detection heliocentric cutoffs, in the hope of better removing their contamination by asteroids.

1.3.3. The biases inherent in surveys

Surveys of the outer Solar System have a number of biases inherent in their construction: all surveys are sampling a particular region of the phase space in a very particular way. There are several major sources of bias to consider: flux bias, pointing or sky coverage bias, ephemeris (followup or tracking) bias, and cadence (detection) bias (Kavelaars et al. 2008a). Careful design of surveys can only minimise rather than eliminating bias, but as long as each survey's characteristics are suitably reported, a given survey's biases can be taken into account during the interpretation of their results, their discoveries "de-biased", to find the true underlying properties of the populations of the outer Solar System. This holds even for surveys with no discoveries: as long as the survey reports where it did not find anything, it still explores phase space in a way useful to understanding the trans-Neptunian region.

As TNOs are discovered primarily in the optical by reflected solar light, surveys are flux limited by the size of their telescopes and the duration of each integration: this **flux bias** leaves them more sensitive to near and bright TNOs than either to small or to distant TNOs. As reflected flux is also proportional to an object's diameter, surveys are also more sensitive to larger TNOs (bigger reflectors) than small TNOsṪhis can be quantified as long as the flux limits of the survey are well known, but at present it leaves a lack of knowledge about very

small sub-10 km sized objects and objects well beyond 50 AU , and an oversampling of the plutinos, which spend much of their orbit interior to Neptune where they are easily detected (Kavelaars et al. 2008a).

The **pointing bias** from the choice of sky coverage for a survey biases which regions of orbital phase space are sampled: an object of orbital inclination i spends most of its orbit at ecliptic latitudes close to $\pm i$ (Gladman et al. 2012), i.e. highly inclined objects spend little of their orbit near the ecliptic. Limited-area surveys are predominantly made near the ecliptic, where more objects can be found, due to the low inclinations of the more abundant TNO populations. This introduces a bias in inclination phase space toward better sampling of the low-inclination population and poor statistical sampling (a few in a few hundred detections) of the high-inclination population (Kavelaars et al. 2008a). High-latitude surveys such as CFEPS-HELIO, and all-sky surveys, address this problem, but it is still prevalent in the current literature (Table 1.1, 1.2). This has masked such statistics as the true proportions of the hot and cold classical populations — this observational bias has previously preferentially selected for the discovery of objects in the cold population, close to the invariant plane/ecliptic, despite the hot population theoretically being larger (Gulbis et al. 2010). It has also masked the true thickness of the Kuiper belt: if visible with the naked eye, the dense core of the Kuiper belt would cover about a quarter of the sky (Fitzsimmons 2000).

Also produced by sky coverage selection is **bias in ecliptic longitude**: populations in certain mean-motion resonances will be better sampled than others, depending on where the sky coverage is placed relative to Neptune (Gladman et al. 2012). The orbital dominance of Neptune clusters the KBO population in its resonant regions; for example, the plutinos come to perihelion $\sim \pm 90^\circ$ from Neptune, and have an observed abundance in that confined region (Gladman et al. 2012). While the point of perihelion of a given resonance will librate, it does not do so over a timescale sufficient to smear out this bias. Existing surveys often unevenly sample this longitudinal structure.

In contrast, **ephemeris bias** results from how well surveys can extend the arcs of their discoveries once made: the initial assumption that an orbit is circular is fine to help fit an initial orbit to the arc of a few days or hours present at discovery, allowing retrieval of the object within a few months of discovery. However, as that assumption is almost certainly incorrect, an object on such a short arc can be lost if follow-up is not available due to lack of telescope resources or adverse weather, by not being in the area of sky expected from the prediction based on a wrong orbit (Jones et al. 2006, 2010). Objects with "extreme" orbital elements at the currently least populated corners of orbital phase space are most likely to be lost in this way (Kavelaars et al. 2008a). This bias can be accounted for by sufficiently wide-field surveys to take advantage of the slow motion of TNOs by designing blindly pointed followup that repeatedly observes the discovery-target sky (Jones et al. 2006).

The distance to which a TNO can be detected is a function of the apparent magnitude of the object, but also of the survey's sensitivity to its motion rate. The choice of cadence of a survey dictates its sensitivity of distance: observing three times in half an hour gives sensitivity to the motion of main-belt asteroids, but not to that of KBOs, which will have barely shifted on the sky to seeing-matched pixels at greater-than-arcsecond-seeing sites, so multi-hour cadences are used in most trans-Neptunian surveys. **Cadence bias** is generated

through this choice of survey cadence: multi-hour cadences will move objects > 50 AU barely two seeing disks between observations at typical ground-based site image quality, so retaining high efficiency in the discovery pipeline to detect such distant objects is difficult (Kavelaars et al. 2008a). Purpose-designed multi-night-baseline surveys for distant objects are necessary, e.g. Schwamb et al. (2009).

Understanding the population that we sample through the surveys is therefore a matter of inversion, applying the survey's characterised biases to its observations to produce a modelled population of the trans-Neptunian region.

1.3.4. Survey detection efficiency and the observable size distribution of TNOs

The completeness of the survey provides a comprehensive measure of its usefulness. A survey provides two values: the number of objects of each magnitude within its sky coverage, which can be better considered as the sky density of TNOs, and the derivative from that, a measurement on the upper end of the luminosity function of TNOs. This constraint provides a check on existing models of TNO size distribution, which are normally fit by a power law (Fraser & Kavelaars 2008).

To calculate this sky density and its derivative constraint, certain parameters of the survey must be found: the magnitude limit in each field; the temporal coverage of the survey; the spatial coverage of the survey. They will be used to characterise the detection limits of the survey.

The direct measurement made by all surveys is the luminosity function: the number of objects found at each magnitude. This apparent magnitude must then be converted to the size of the object, based on its heliocentric distance and its reflectivity (geometric albedo). Multiplied by the density of observed TNOs on the sky, this gives the true useful measure of the TNO population, its size distribution: the number of objects that are of each diameter, and the population's total mass.

For an object on a circular orbit, its magnitude $m_{opposition}$ when seen at opposition, at heliocentric distance r_H and geocentric distance $\Delta \sim (r_H - 1)$, with an albedo p and a radius R is given by (Tombaugh 1961):

$$m_{opposition} \propto pR^2 r_H^2 (r_H - 1)^2 \tag{1.7}$$

and therefore, assuming a given constant limiting magnitude and a given albedo, the object's radius is given by (Tombaugh 1961):

$$logR = logr_H(r_H - 1) + constant \tag{1.8}$$

or for $r > 10$ (Tombaugh 1961):

$$logR = 2logr_H + constant \tag{1.9}$$

If this is modified to take into account the object's geometric albedo p, a radius-magnitude relation can be obtained (Luu & Jewitt 1988):

$$pR^2 = 2.25 * 10^{16} r_H^2 \Delta^2 10^{0.4(m_{Sun} - m)} \tag{1.10}$$

where m_{Sun} in $m_R = -27.26$ (Luu & Jewitt 1988).

In a more generalized wavelength-dependent parameterization, the magnitude of the object we observe that has a diameter D is given as (Fraser & Kavelaars 2008):

$$m = K_\lambda + 2.5log_{10}(\frac{r_H^2\Delta^2}{D^2 p_\lambda}) \tag{1.11}$$

where p_λ is the wavelength-dependent object geometric albedo (discussed in more detail in § 1.4.1) and the constant is given by K_{lambda}; in R-band, $p_R \sim 4\%$ gives $K_R = 18.8$ (Fraser & Kavelaars 2008).

This means the smallest observable object at a given heliocentric distance r_H, observed by a survey with a limiting magnitude of m_{max}, has a diameter (Fraser et al. 2008):

$$D_{min} = \frac{r_H^2 10^{(K_\lambda - m_{max})/5}}{\sqrt{p}_\lambda} \tag{1.12}$$

Correspondingly, the largest observable object, D_{max}, comes from applying the magnitude m_{min}.

The cumulative sky-plane surface density of TNOs, σ deg^{-2}, can be fitted (Jewitt 2000b):

$$\log \sigma = \alpha(m_R - m_0) \tag{1.13}$$

where α, m_0 are constants, and m_R is the red magnitude. Surveys have to observe down to a magnitude of $m_0 = 23.3 \pm 0.1$ to reach the surface density where there is one object per square degree of sky (Jewitt 2000b). Schlichting et al. (2009) used HST to find a surface density of KBOs with diameters larger than half a kilometre of $.1^{+4.8}_{-1.7} x 10^7$ deg^{-2}, which superseded previous surface density measurements from occultations, particularly the non-detections of the TAOS occultation survey (Bianco et al. 2010).

The number of TNOs in a survey field can be parameterized as (Jewitt 2000b):

$$N = A \int \int R(r)s(D)dDdr \tag{1.14}$$

where A is a normalisation constant, R(r) is the radial distribution, s(D) is the size distribution, r is the heliocentric distance and D is the object diameter.

So from these two measurements, we can obtain the size distribution of all TNOs. The largest objects currently known are Pluto (radius 1173^{20}_{10} km (Zalucha et al. 2011))[13] and Eris (assuming it is spherical), radius of 1163 ± 6 km (Sicardy et al. 2011)). The smallest is the unnumbered object of Schlichting et al. (2009), 1040 ± 120 m in diameter. The expected numbers of dwarf planets can be estimated from fitting models to the measured sky-plane surface density of TNOs.

However, the differential power law used to describe the size distribution does not have constant coefficients across all diameters. This raises complications when trying to work out the total population of TNOs. Our understanding of the cumulative size distribution at different diameter ranges is described by the parameterisation (Irwin et al. 1995):

$$N(> r) \propto r^{1-q} \tag{1.15}$$

[13] At 6.5 to 24 microbars (Lellouch et al. 2009), Pluto's atmosphere is dense enough that its surface is not directly detected during occultations. This gives a comparatively large uncertainty to its diameter, depending on the atmospheric assumptions made in the processing of the occultation timing measurements.

where $N(> r)$ is the number of objects with radii greater than r, and q is the power-law index. The correspondence between this and Eqn. 1.13 is given by (Petit et al. 2008):

$$\alpha = \frac{q-1}{5} \tag{1.16}$$

q varies considerably: its change at different diameters has been an area of very active research in the last decade. It indicates how the TNO population has been sculpted; the current TNO population is a relic of its former self, retaining only approximately 0.1 M_{Earth} (Bernstein et al. 2004; Petit et al. 2008). Assumptions about albedos, since $M \propto p^{-3/2}$, play a role in the uncertainty on this value. The remaining population has been modified through collisional grinding and scattering (Kenyon et al. 2007). This means the original population was much more massive, and it is this inferred massive original population that must be used in calculating the dynamical evolution of the Solar System. Almost all of the original objects have been scattered to the most distant reaches of the Solar System.

1.3.5. The most distant objects

The existence of trans-Neptunian objects at the limits of the current surveys can be constrained to certain mass ranges. The current generation of optical surveys place strict limits out to ~ 200 AU within their sky coverage; Schwamb et al. (2010) were even more sensitive in their extensive sky coverage, out to ~ 1000 AU (motion rates of 0.2″/hr) . However, there are other methods that also restrict the existence of very large Solar System companions at greater distances: infrared surveys and measurements of perturbers of stable astronomical clocks.

A TNO of dwarf planet size rapidly becomes too cold, and correspondingly too faint, to be seen when beyond the orbit of Jupiter in the comparatively short exposures of all-sky surveys in the infrared. Reflected sunlight is brighter in the optical than in the infrared at those distances, so the large optical surveys are better placed to detect sub-Earth mass objects. However, a distant Jovian-mass object would emit its own radiation in the mid-to-far infrared and would be visible to the space-satellite IR surveys: IRAS (1984), ISO (1996), MSX (1996), AKARI (2006), and WISE (2008).[14] It would show as a slow-moving 40-100 K blackbody; for example, a Jupiter-size object at 570 AU would glow with 1 Jy at 60 microns (Houck et al. 1984). IRAS detected no such object (Beichman 1987). AKARI has not published any such analysis of its transient sources, or published a transient catalogue, though it has reported observations of known main-belt asteroids as part of its survey (Usui et al. 2011), and some dedicated observations of TNOs (Sekiguchi et al. 2012). WISE was sufficiently sensitive to outer Solar System objects, particularly in its longest-wavelength 22 micron channel; its Solar System moving objects pipeline, NEOWISE, recovered 32 Centaurs and scattered objects, of which 6 were new discoveries (Bauer et al. 2011). Their data are also not yet fully analysed for large distant objects. The low temperature of an Oort cloud Jupiter-mass gas giant at 30,000 AU would make it just detectable in WISE's longest band at 4.9 microns, but such an object would be so far into the noise of the data that their pipeline would require rewriting for reprocessing and co-adding the entire survey (Wright 2011), J. Masiero (pers.comm.).

[14] ISO and MSX both had small ~ 10% sky coverage; IRAS, AKARI and WISE were dedicated all-sky surveys.

Several authors have argued that the long-period and outer Oort cloud comets show a preferred scattering in their orbital elements and aphelia distributions that is evidence for a 1-4 Jovian-mass planet in the outer Oort cloud (the most comprehensive overview is Matese & Whitmire (2011)). However, the observed population of long-period and first-time comets is very difficult to accurately debias (Horner & Evans 2002); the thousand-strong comet catalogue that will be produced by the Gaia mission's survey offers more promise for testing cometary ephemerides for the effects of distant perturbers (Horner & Evans 2002).

The highly precise measurements of stable astronomical clocks, such as the rate of change of the period of systems such as pulsars in binary systems and pulsating white dwarfs, provide constraints on the presence of a massive companion to the Solar System: its mass would accelerate the Solar System barycentre. No acceleration has yet been found. Combining several types of clocks that provide a reasonable spatial sky coverage has generated a sensitivity of $a_{Sun}/c \sim 10^{-19}$ s^{-1}, which limits the existence of a Jovian-mass planet at 200 AU (Zakamska & Tremaine 2005). The arguments of Matese & Whitmire (2011) are further countered by the greater sensitivity of the acceleration method: while IRAS is more sensitive to Jovian masses at 70-400 AU, this method is more sensitive to possible planets at $> 300 - 400$ AU than either the optical and infrared surveys or the residuals in the motion of the comets (Zakamska & Tremaine 2005). This limit will be improved by the long-term decadal measurements of pulsars planned for the Square Kilometre Array (Seto & Cooray 2007).

These constraints on the existence of high-mass objects do leave open the possibility of Mars-sized objects in the outer reaches: a 23^{rd} mag object of Mars- to Eris-size would easily have escaped notice in the current surveys (Trujillo 2008). This thesis will not place constraints at those magnitudes. For that, we require the next generation of TNO surveys; those that are planned to occur on the 4 m + apertures that are equipped with wide-field cameras. These include the Outer Solar System Origins Survey with MegaCam (Boulade et al. 1998) on the Canada-France-Hawaii Telescope (OSSOS)[15], the HyperSuprimeCam on Subaru (Miyazaki et al. 2012), the Dark Energy Camera on the Cerro Blanco 4 m (DECam) (DePoy et al. 2008), and further in the 2020s, the Large Synoptic Survey Telescope (LSST) (Collaboration et al. 2009).

1.4. Dwarf planets: the largest objects in the size distribution

The brightness of an object detected by a survey is a function of its size and distance. Those objects bright enough to study in detail are often also the largest objects. Understanding the physics of the geology and evolution of such worlds, to better understand planetesimal composition and evolution, motivates surveys to discover TNOs.

The most interesting bodies of the trans-Neptunian realm are those that are large enough to have differentiated: separated out to have a core and mantle[16]. Differentiation takes place when the internal gravity of a world is enough to cause the materials of different densities to separate out. For bodies formed beyond the Solar System's water ice line, which in the present day is midway through the asteroid belt, this produces a core of silicates

[15]CFHT Large Programs 2013-16

[16]Unlike the terrestrial planets, this differentiation does not produce a lithologically separate surface crust.

("rock") and a mantle of volatile species and compounds ("ices"). It is too cold for water ice to sublimate at Kuiper belt distances, so water ice forms a stable bedrock for the other volatiles.

Since their formation, the surface temperatures of TNOs have remained below about 50 K; this has protected the volatile molecules that were trapped during accretion (Jewitt 2000a). However, differentiated TNOs are far from pristine: collisional processing from the 1.5 km/s velocity dispersion among TNOs, and radiogenic heating in those larger than 100 km diameter, have modified this initial state.

The exact size at which a world is large enough to differentiate is not precisely clear. The existence of differentiation is taken to occur when a body ceases having a lumpy form; the column pressure on the material at its core is sufficient for it to round into hydrostatic equilibrium. This does not mean that it will be spherical. Nonzero rotation rates will invariably distort it to an oblate sphere. Particularly high rotation rates, such as the 3.9 hour period of (136108) Haumea, will cause the body to flow into the form of a Jacobi ellipsoid (Rabinowitz et al. 2006).

Heat within the planetary interior can assist in this process. Endogenic heating is provided by Al^{26} in dust from supernovae, accreted during the TNO's formation. This provides heat in the interior of the body, but only soon after its formation (this radioactive isotope has a half life of only seven hundred thousand years, so its influence is particularly short-lived). Exogenic heating can be provided by impacts, or if the body is in a binary system or has a sufficiently close moon, through tidal "kneading".

The dwarf planets are large enough to retain a variety of the most volatile ices. We record the existence of these species through their spectral features.

1.4.1. Understanding surface composition

The most basic observational information about a non-luminous object is what alteration it provides to the light that it reflects. The Sun's G2V spectrum is brightest in the visible bands. Light radiates outward isotropically from the (approximately) spherical Sun, diminishing its intensity in an inverse-square relation with distance as it spreads into the spherical volume; the light reflected from a trans-Neptunian surface back to an observer on Earth undergoes this twice, and so is diminished as inverse to the fourth. At trans-Neptunian distances the light is diminished indeed. In addition, the steep slope of the size distribution means that most TNOs are so small that their reflecting area, and thus the amount of light they return, is minimal at best. It requires our largest telescopes, 8–10 m diameter, observing the brightest of these worlds, to pick out this scant scattered light, which contains information about the composition, temperature, phase and structure of the surface.

These reflection spectra contain solar lines, and the composition of the TNO's variety of surface materials produce solid-state absorption lines, which are identified through comparison with spectra measured in the laboratory from thin films of ices of individual volatiles chilled to the trans-Neptunian temperatures of fifty K.

The strongest spectral lines of volatiles are found in the visible and near infrared. They shift in position as a function of the temperature of the surface and the phase (level of

crystallisation) of the material, and their absorptions change if the volatiles are diluted by several species being mixed together. The morphology of the ice grains form a varyingly reflective surface that is difficult to model – the most typically used scattering model is that of Hapke (2005), but it is very hard to obtain a unique model for each observed spectrum. The complex interaction of the effects of grain size, shape, size distribution and porosity of the surface are difficult to separate. This leads to spectral models that have many free parameters.

The spectra also sample only the composition of the first few millimetres of the surface at most: the path length of light through the translucent depths of methane and nitrogen ice is only a few centimetres (Abernathy et al. 2009). This means they do not necessarily reflect the TNO 's bulk composition, and can be (perhaps disproportionally) affected by surface processing effects. Long-term effects on these surfaces are difficult to study well in the lab, because the processes take place over millennia-long timescales. They include irradiation, impact gardening and sputtering.

There are four classes of object that are seen from these spectra: those with methane, with moderate water ice features, with strong water ice lines, and those with no features at all (Fig. 1.4). Objects such as (50000) Quaoar and (136108) Haumea (2003 EL_{61}) show crystalline water ice spectra (Jewitt & Luu 2004; Trujillo et al. 2007), (134340) Pluto and (136199) Eris show evidence for surface methane (Brown 2002; Brown et al. 2005), and some TNOS e.g. 1996 TL_{66}, show featureless near-IR spectra like those of the Jovian Trojans (Luu & Jewitt 1998b).

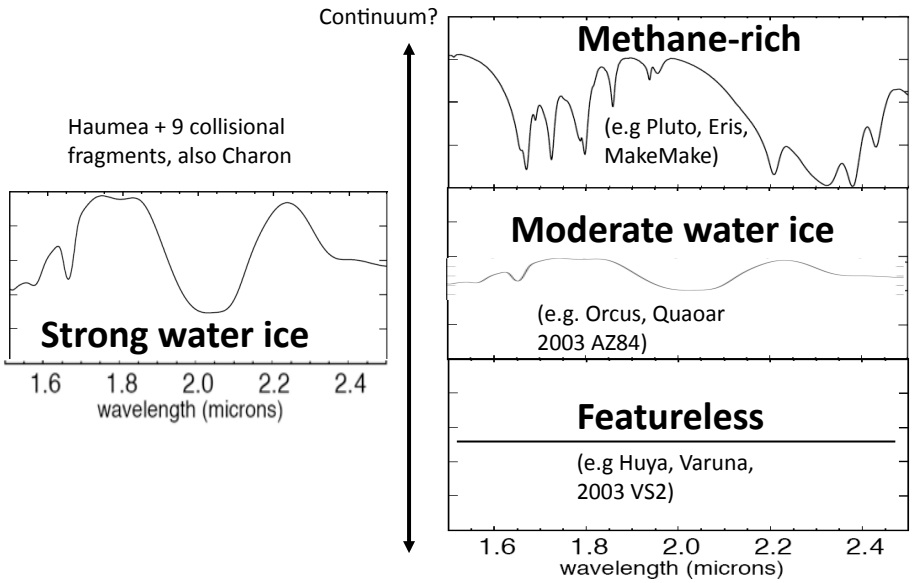

Figure 1.4 The differentiation in spectra between those KBOS where spectra are obtainable. (E. Schaller, pers. comm.).

The largest dwarf planets are methane-rich: Eris, Pluto, Makemake (2005 FY_9) and Quaoar all have methane on their surfaces (Brown et al. 2005; Brown 2002; Brown et al. 2007; Schaller & Brown 2007a). This distribution of volatiles with object size was explained in the model of Schaller & Brown (2007b): the retention of surface volatiles is predicted as a function of an object's size (its surface gravity) and its temperature regime (perihelion distance) (Fig. 1.5).

This accounts for the stability of methane on the surface of objects such as Pluto over Solar System-age timescales; it is still present even on Quaoar, which sits right at the boundary of long-term stability (Schaller & Brown 2007b).

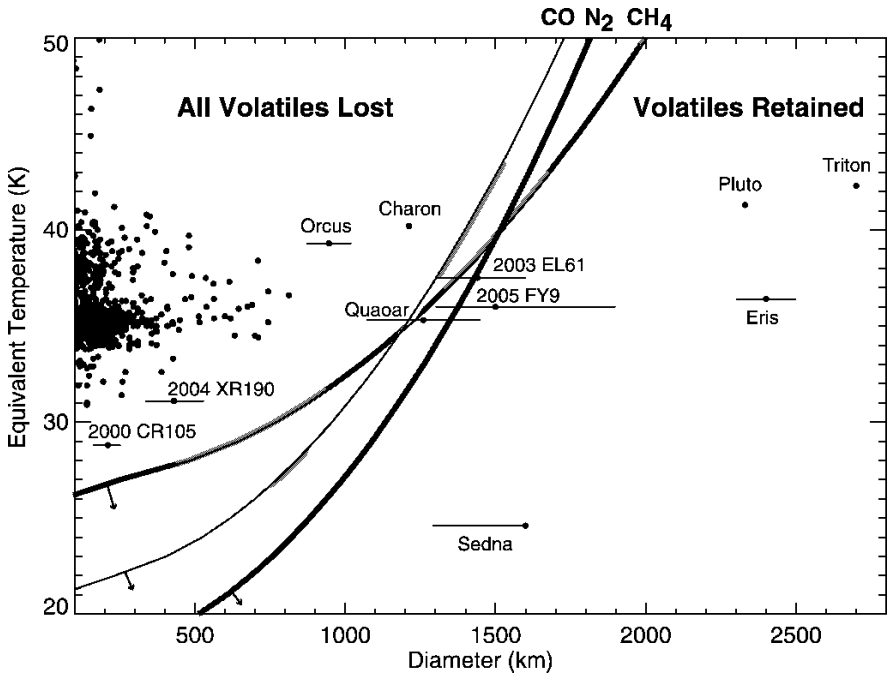

Figure 1.5 Schaller & Brown (2007b): the volatile species retained on a large TNO are a function of the dwarf planet's solar distance (the temperature it experiences) and its mass (the surface gravity it applies to retain atmospheric molecules).

The slow sparse rain of cosmic rays onto this surficial methane forms higher-order hydrocarbons. For example on Eris, Brown et al. (2007) found a good fit to the major spectral features could be made by a surface that had an intimate mixture of 1 cm methane grains, 100 micron ethane grains, and 10 micron tholin grains. Brown et al. (2007) also suggested that as the path lengths are very long, the big methane grains may be sintering into large polycrystalline slabs, with a photolytic rind of the higher-order hydrocarbons on top.

Acetylene should also be one of the higher-order hydrocarbons present on dwarf planets, but has so far not yet been detected on any body. Its features would be very subtle; they were not seen on Eris by Brown et al. (2007).

Water ice detections pose a particular puzzle. Most water ice bands seen in the trans-Neptunian region are the bands formed by crystalline water ice. Models of the space environment instead suggest that the unceasing bombardment of cosmic rays should break down the crystals into amorphous water ice, in the space of one to ten million years. This mismatch with the observations has led to the conclusion that the water ice on the surfaces of these objects is regenerating in a constant cycle of transformation (Mastrapa & Brown 2006), though this is debated by Zheng et al. (2009). Whether this is through cryovolcanism or other mechanisms is not yet determined.

The majority of TNOs smaller than dwarf planets have surprisingly disappointing near-infrared spectra that are featureless, with no absorption lines (Fig 1.4). Their wavelength-

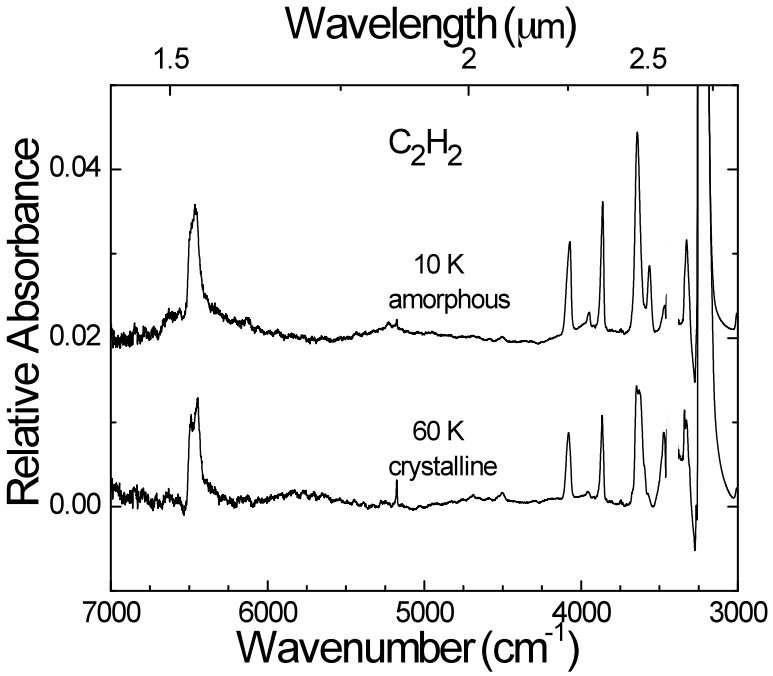

Figure 1.6 Acetylene reflection spectra from thin-film laboratory measurements (M. Moore, pers. comm.). The small features are hard to detect against the background of lines from other volatiles.

dependent surface reflectance, or spectral slope, is completely flat. This lack of distinguishing properties makes it difficult to infer their composition or if any material evolution has taken place. However, they are the most abundant type of TNO discovered in surveys, so reaching an eventual understanding of their surface composition and evolution will be necessary to understand this majority of the modern planetesimal population.

Interpretation of spectra is not possible without knowledge of the geometric (Bond) albedo p_λ of the object, specifically in the wavelength range in which the spectra was measured (Stansberry et al. 2008). Albedo is governed by surface composition: in determining how bright an object will appear in a survey, a dwarf planet covered in methane frost will be more reflective than a deeply reddened object covered in high-order hydrocarbons.

The apparent magnitude of an object is dependent on its geometric albedo: brightness is a product of p_λ and the cross-sectional area available to reflect light (phase function can be neglected as being at unity for TNOs) (Russell 1916; Stansberry et al. 2008). If the object is large enough or close enough for its thermal radiation to be detected, then the albedo can be precisely calculated in combination with the visual measurements, as thermal radiation is dependent on the surface area and object temperature, the latter dependent on albedo (Stansberry et al. 2008). The 50 K temperatures in the Kuiper belt mean that obtaining the thermal measurements normally requires a space-based telescope as the TNOs are so faint, so thermal measurements are available for only a subset of the known TNOs.

Having an accurate albedo allows a conversion of observed visual magnitude to effective radii. The inadequacy of visible observations to determine size for all but the largest, resolvable TNOs means many TNO sizes are inferred from an assumed albedo, normally set at about 4% (Lykawka & Mukai 2005). Through measurements of thermal emission objects

have now had their albedos determined down to the sub-100 km range; in the regime below ~ 700 km diameter, albedos hover around 4-8%, e.g. the sample of 52 dynamically excited objects observed by WISE had a mean albedo of 8 ± 4% (Bauer et al. 2013). Albedos may be as high as 15% in some slightly larger 400-600 km diameter cases, e.g. Ixion and 2003 AZ_{84} (Stansberry et al. 2008). At the largest end of the size distribution, dwarf planets show a wide range of albedos: Varuna $11.6\pm^{7.6}_{4.6}$% (Stansberry et al. 2008), Sedna > 4.6% (Grundy et al. 2005), Quaoar 19 ± 3% (Grundy et al. 2005), Charon 37 ± 2% (Grundy et al. 2005), Pluto 72 ± 12% (Grundy et al. 2005) and Makemake 77 ± 3% (Ortiz et al. 2012). In general, it is the dwarf planets rather than the smaller TNOs which have the higher albedos (Brown 2008).

Exact sizes can also be found from occultation measurements, and the albedo found instead. These have put the measured upper end of the TNO visual albedo range remarkably high: close to perfectly reflective. At $p_V = 88\pm^{15}_{6}$%, 2002 TX_{300} (Elliot et al. 2010) is a small, 186 km-diameter member of Haumea's collisional family. Objects in this dynamical and compositional family are expected to be highly reflective due to their surface spectra of pure water ice; they are atypical of most small TNOs. Eris has an even higher albedo of $96\pm^{9}_{4}$% (Sicardy et al. 2011).

The main distinction that can be made from the known albedos is that dwarf planets operate in an albedo range quite different to that of small < 400 km TNOs: those objects large enough to retain even a tenuous or episodic atmosphere have their brightness decisively influenced by the patchy surface frosts renewed through atmosphere-surface interactions. Consideration of such strong albedo variability and extreme reflectivity is important when assessing how the observed magnitudes of objects discovered in surveys correlate with their sizes; a given albedo value is unlikely to hold true across all TNOs bright enough to be found in shallow surveys.

1.5. Summary and thesis outline

The sculpted form of the Kuiper belt and the other distinct trans-Neptunian populations provide constraints on the evolutionary history of the Solar System. As observational surveys have sketched in the population groups over the last two decades, providing an evolutionary model that can encompass the origin of each population group has proved difficult. This has led to a broadening in evolutionary scenarios, from the emplacement of the Kuiper belt by the smooth migration of Neptune (Malhotra 1993, 1995) to the more violent scattering events driven through abrupt ice giant migration that are postulated in various forms of the Nice model (Tsiganis et al. 2005; Levison et al. 2007), and hybrid models (Murray-Clay & Schlichting 2011).

As the dynamical models increase in subtlety and complexity, so too have the surveys. These trans-Neptunian populations are defined by their orbital parameters; a detailed characterisation of their relative abundances, their size distributions, is necessary to ensure the dynamical models are correctly reproducing the present-day features. This has been made through both wide-field and pencil-beam surveys (Fraser & Kavelaars 2008; Fuentes & Holman 2008; Bernstein et al. 2004), which characterise the size distribution by sampling particular diameter ranges through to their survey magnitude limits.

Space-based infrared wide-field surveys can potentially see exceptionally large objects at trans-Neptunian distances, though they are not useful to search for average-sized TNOs as those are not large enough to produce enough infrared emission to reach their survey sensitivities. They do provide constraints on the population of super-sized dwarf planets in this realm. Most notably, they provide no indication of the existence of any companion object to the Sun, such as a small brown dwarf or scattered gas giant; the WISE satellite's survey is theoretically able to provide such constraints to levels that can then overlap with the wide-field optical surveys.

The trans-Neptunian objects have been extensively surveyed in the Northern Hemisphere sky (Tombaugh 1961; Trujillo & Brown 2003; Elliot et al. 2005; Larsen et al. 2007; Brown 2008; Kavelaars et al. 2009; Schwamb et al. 2010). All surveys sample only a particular subregion of orbital parameter space. This is defined by their sky coverage, temporal sampling (observing cadence) and magnitude limits. These surveys have focussed on the regions near the ecliptic. Lack of dynamical excitation in a TNO's orbit implies a primordial, unaltered orbital nature; the high-inclination population of TNOs maps out the scattering events. Most of the dwarf planets have substantial orbital inclinations of tens of degrees, despite the lack of dynamical correlation between mass and scattering inclination. This puts a survey of the entire southern sky, far from the ecliptic, at an advantage for detecting new large bright trans-Neptunian objects, and adding to the statistics of the high-inclination scattered population. At the start of this thesis, only minimal surveying had yet been made at these high ecliptic latitudes in the Southern Hemisphere.

The following chapters of this thesis detail our[17] study of the trans-Neptunian population of the Solar System as visible in the southern sky. It is divided into several sections:

Dwarf planets and large TNOs offer tests of our understanding of volatile processes and icy surfaces in the outer Solar System. We took opportunities to examine individual TNOs, which are detailed in Chapter 2: an attempt to detect ammonia on Pluto's moon Charon with Gemini's GNIRS spectrograph, and the first observed light-curve for the Centaur-like TNO 2012 DR30, which fell on Uppsala survey fields after the collection of the Uppsala TNO survey data.

To try to obtain more bright TNOs to study in detail, we needed a southern sky survey. Fortunately, ANU has been involved for some fifteen years with the Catalina Sky Survey, which searches for near-Earth asteroids using the 0.5 m Uppsala telescope at Siding Spring Observatory. This survey's data set runs from 2004 to 2009, and the survey is on-going. Careful consideration of the Uppsala sky coverage through time showed that it would be possible to re-analyse its data set for TNOs, and the CSS kindly agreed to this. The development of a method to transform this asteroid survey into a resampled TNO survey, operating at a completely different cadence, is detailed in Chapter 3.

The results of this analysis are described in Chapter 4. No new bright objects were discovered. We examine the efficiency of the survey at detecting bright objects through the development of a survey simulator, and discuss the implications of the null detection for the TNO populations. The Uppsala survey completes the surveying of bright TNOs across the sky, examining the phase space of magnitudes where other surveys would saturate.

[17] For stylistic reasons I use the plural form throughout this thesis to refer to work led by myself but naturally done in collaboration with my supervisory panel. The text however is solely my own.

However, it is limited to $< 20^{th}$ magnitude objects. We discuss the survey's sensitivity to large, very distant (> 100 AU) objects, cf. § 1.3.5.

We conclude this thesis in Chapter 5 with a discussion of the project and the prospects for future TNO surveys and object characterisation, including those with the telescopes that are planned for the next decade. These include a proposed future Southern Hemisphere TNO survey with the new ANU 1.35 m SkyMapper wide-field survey telescope at Siding Spring, together with our design choices to ensure that the survey will have the best possible coverage of the TNO population visible to $g \sim 21.5$. The simulator of Ch. 4 could also be applied in the future to the SkyMapper survey. This is followed by a full reference list and an appendix.

CHAPTER 2

Investigations of two TNOs

> Instead it is we who are seized; and not, it would seem, for any greater knowledge; but instead made idle sport of by atmospheres and ice.
>
> – Ernest Shackleton

The trans-Neptunian objects of the outer Solar System are a population of the remnant planetesimals from its formation. Their surfaces show us the ices of their composition. These surfaces have changed through more than four billion years of irradiation and impact resurfacing: TNOs now effectively conceal their pure primordial compositions.

These distant worlds are extremely faint. Only a handful of the 1600 objects known are sufficiently large to allow spectroscopic studies. They reflect a solar spectrum imprinted with diagnostic near-infrared absorption bands that can be linked to species of ices. Definite detections include the ices of water, methane, carbon monoxide, nitrogen, methanol and ethane (Brown 2012); water is the most abundant, due to its comparative lack of volatility.

Their mix of ices provide sample points to the makeup of the primordial nebula in its distant, tenuous regions (even though their subsequent evolution mean the primordial ice abundances are not directly visible). This ties directly into the physical and chemical conditions used in models of planetary formation.

In the last decade, the astonishing variety of these large TNOs has become apparent. Where once it seemed that their common origin in the outer reaches of the primordial nebula should have led to a uniform set of internal compositions and densities, we have instead found a dazzling array of differences that continue to thwart efforts to produce a consistent explanation.

The surveys discussed elsewhere in this thesis did not offer any opportunity to characterise new outer Solar System objects. However, two interesting questions presented themselves as opportunities in the course of the thesis: the first a puzzling aspect of the surface composition

of a large TNO , and the second the determination of the properties of a newly found TNO with an orbital history that suggested its physical properties might be out of the ordinary.

In this chapter, we investigate the surface properties of two TNOs: Charon, to try to detect ammonia (§ 2.1), and a recent capture to the inner Solar System, 2012 DR_{30}, which was discovered in February 2012 and has not yet been studied (§ 2.2). However, our observations met only partial success.

2.1. Searching for ammonia on the surface of Charon

Charon, the largest moon of the dwarf planet Pluto, is one of the very few trans-Neptunian objects large enough for us to be able to study the ices of its surface. The absorption bands in Charon's spectrum are dominated by water ice. However, near-infrared observations of Charon have shown a 2.21 micron absorption band, which has been attributed to ammonia. Ammonia decreases the melting point of a water ice mix: a sufficiently large TNO, heated during its accretion, could once have had an internal ocean. The 2.21 micron absorption band could be the signature of ancient cryovolcanic lavas.

Unfortunately, this single observed line is ambiguous: its position could be strongly influenced by the ice grains' size and shape. It only provides a tantalising hint at this geophysically important molecule, not confirmation of its presence. Detecting a stronger second line would provide this proof. Laboratory studies show that the deeper fundamental line of ammonia sits at 3-3.1 microns, in the L-band.

In this section, we extend on our motivations for trying to confirm the detection of ammonia on Charon (§ 2.1.1), and describe our observational setup and results from two hours of observing Charon with GNIRS on Gemini North to obtain an L-band spectrum that could confirm the presence of ammonia (§ 2.1.2).[1] We found that the integration time calculator was not well suited to determining the integration time needed for the measurement: as a compromise we were granted two hours to make the experiment, but this proved unsuccessful at detecting Charon in L-band.

2.1.1. The uncertain presence of ammonia

Charon is more than half the size of its primary, and its size is well known due to its near-lack[2] of an atmosphere: 606 ± 1.5 km in radius (Person et al. 2006; Gulbis et al. 2006). Its collisional formation (Canup 2005) did not quite leave it large enough to retain a surficial layer of volatiles over its involatile water ice (Schaller & Brown 2007b). Its surface composition now differs dramatically from that of its primary: Pluto is dominated by methane and molecular nitrogen, Charon by crystalline water ice – but Charon also has a tantalising hint of ammonia.

[1] Based on observations obtained at the Gemini Observatory, which is operated by the Association of Universities for Research in Astronomy, Inc., under a cooperative agreement with the NSF on behalf of the Gemini partnership: the National Science Foundation (United States), the Science and Technology Facilities Council (United Kingdom), the National Research Council (Canada), CONICYT (Chile), the Australian Research Council (Australia), Ministério da Ciência, Tecnologia e Inovação (Brazil) and Ministerio de Ciencia, Tecnología e Innovación Productiva (Argentina).

[2] $< 0.11 \mu$bar N_2 (Person et al. 2006)

Ammonia is an important ice because it lowers the melting point of a mix with water ice. This raises the possibility of internal oceans in large trans-Neptunian objects. Strazzulla & Palumbo (1998) showed that ammonia hydrates are easily destroyed by irradiation; at a distance of 40 AU, this would take less than ten million years (Cooper et al. 2003, 2008). However, these hydrates have possibly been observed on the surface of Charon (Brown & Calvin 2000) and the slightly smaller TNO Orcus (Barucci et al. 2008b). This presents a puzzle: a supposedly static, frozen world is actively resurfacing itself. Possible mechanisms are impact gardening exposing new subsurface, solid-state convection of the mantle, and cryovolcanism erupting ammonia-water lava from an internal ocean.

Brown & Calvin (2000) suggested that ancient cryovolcanism was the most likely cause. If ammonia from frozen ancient lavas is layered on the surface of Charon, this offers a unique opportunity: direct access to the internal composition of a trans-Neptunian object. Currently active cryovolcanism, as suggested by Cook et al. (2007), is geophysically implausible, as the heat provided by accretion and by the initial radionucleide abundance of these TNOs to a possible internal ocean has long since dissipated. The liquid reservoirs would have solidified in the intervening four billion years. But if the lavas are ancient, it requires ammonia to be stable under long-term radiation, contrary to the laboratory studies. To resolve these contradictory situations, we must first have solid proof that this geophysically important molecule does indeed exist on Charon.

The diagnostic signatures of ammonia and hydrated ammonia are in the near infrared. Existing laboratory spectra of chilled thin-film ices, which provide us with the lines that should be visible in this spectral band, show that the fundamental transition of ammonia is in the mid-infrared L-band. Only shallower overtone bands are found at the shorter wavelengths of J, H and K bands.

Laboratory data indicate that there is a clear and well-understood band at 2.2 microns (Fig. 2.1). However, the prominent fundamental ammonia absorption band is at longer wavelengths, between 2.96 and 3.11 microns (Moore et al. 2007), as shown in Fig. 2.2. This observation is therefore key to confirming the detection of ammonia: we expect to see this band in the L-band reflectance spectra of Charon, if cryovolcanism is occurring on Charon.

Previous observations of Charon in these near-infrared wavelengths have provided good measurements from 0.6-2.45 microns in V, J, H and K on FORS2/ISAAC/SINFONI at the VLT (Merlin et al. 2010). These improved on 1.5-2.4 micron measurements in H and K with NIRI (Cook et al. 2007, 2009), who were in turn improving on the work of Brown & Calvin (2000), Buie & Grundy (2000) and Dumas et al. (2001). These measurements provide tantalising evidence for the presence of ammonia ice, ammonium hydroxide, and ammonia hydrate; the clearest feature that they saw is at 2.21 microns.

However, a single line does not provide a positive identification. The line position in solid state absorption spectroscopy can be affected by the shape and size of the grains of ice (eg. Fig. 2.3). Detection of the much stronger fundamental of ammonia, providing a second line, would resolve this ambiguity. This makes observations at wavelengths beyond 2.45 microns a priority for resolving this signature of potential cryovolcanism.

The only data taken to date at such wavelengths were with NACO on the VLT at 1-4 microns (JHK, L, M) (Protopapa et al. 2008) (Fig. 2.4). These data have low signal-to-noise. They

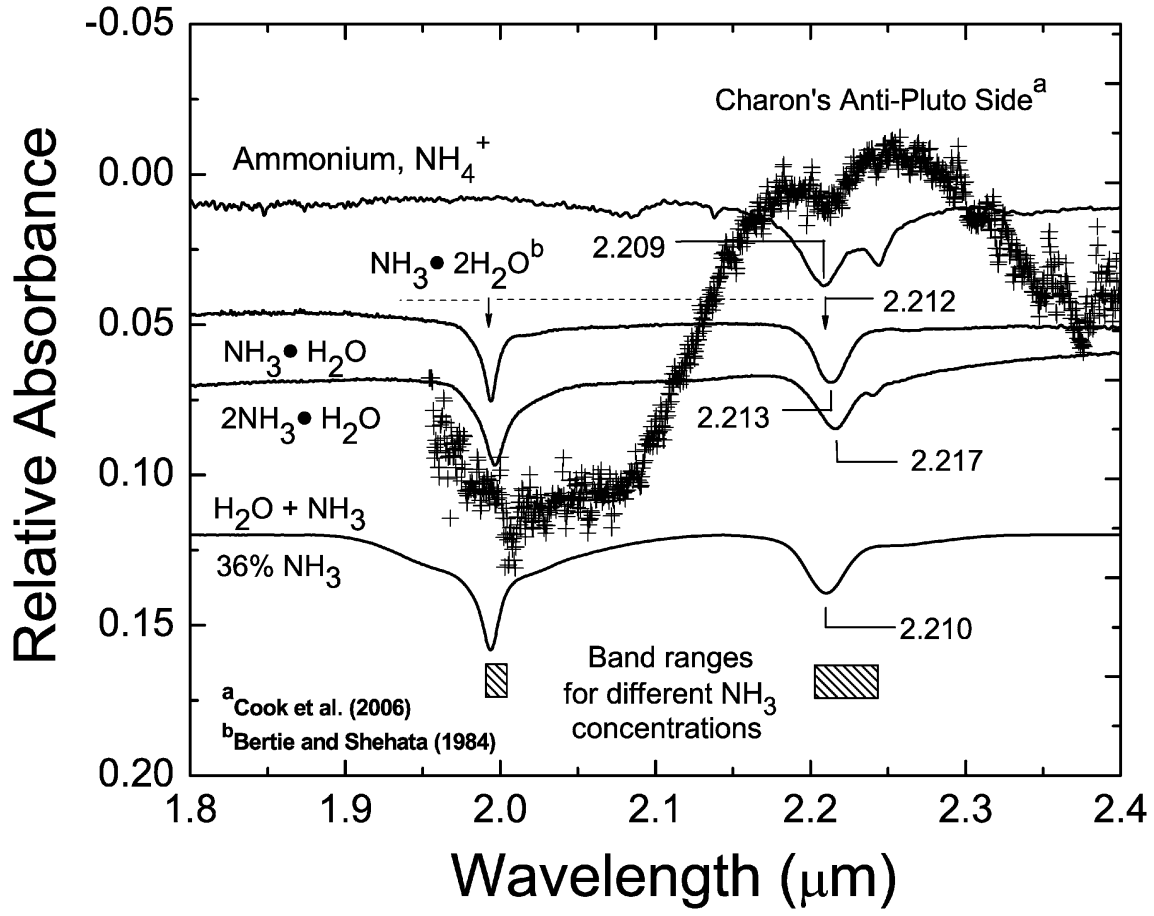

Figure 2.1 Moore et al. (2007): laboratory IR spectra of $2NH_3{\cdot}H_2O$, $NH_3{\cdot}H_2O$, and a mixture deposited at 90 K, showing the frequently-observed band at 2.21 microns. A spectrum by Cook et al. (2007) of Charon's anti-Pluto hemisphere, which is at 42 K, is shown for comparison. Spectra are stacked for clarity and scaled to the 2.21 micron ammonia band.

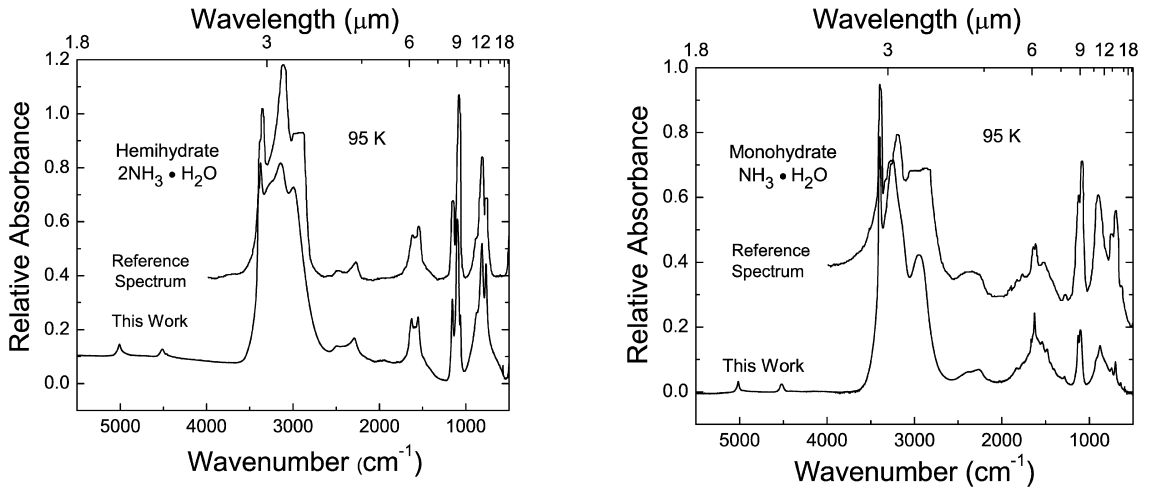

Figure 2.2 Moore et al. (2007): laboratory IR spectra of $2NH_3{\cdot}H_2O$ and $NH_3{\cdot}H_2O$ at 95 K. Note the prominent broad absorption feature at 3.08 microns (3250 cm^{-1}), produced by the overlap of the ν_1 H_2O and the ν_3 NH_3 bands, and how minor the absorption at 2.21 microns that was prominent in Fig. 2.1 appears here in comparison.

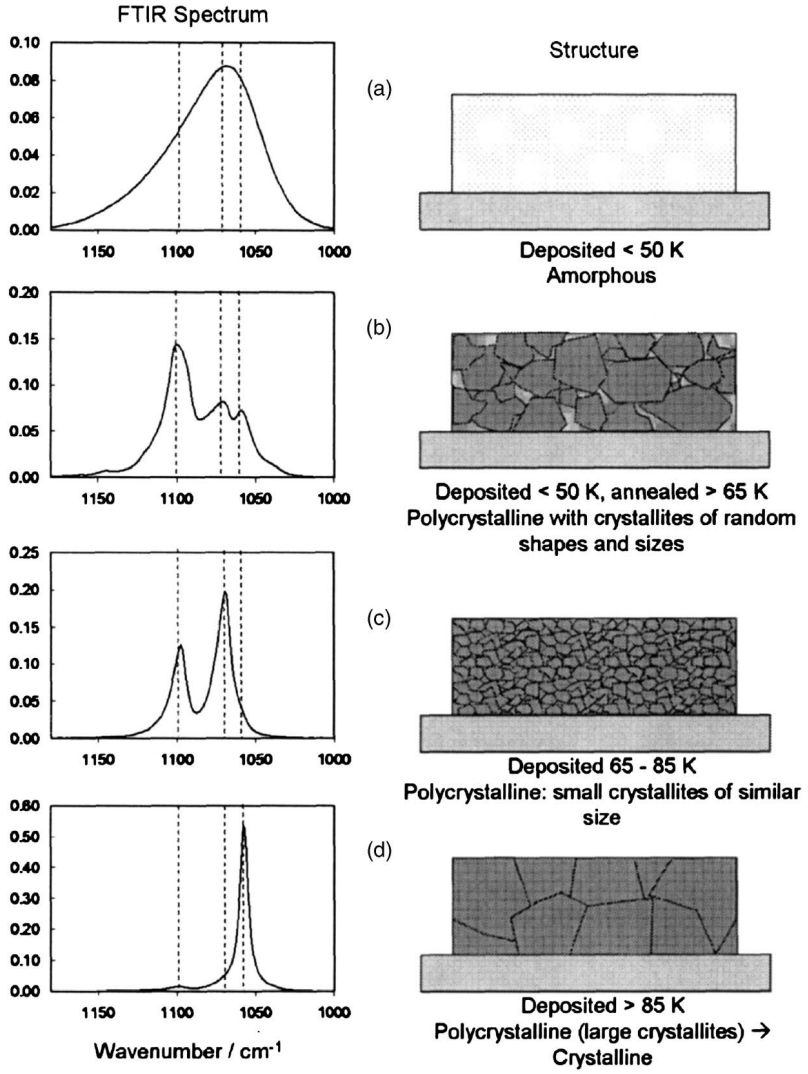

Figure 2.3 Dawes et al. (2007): laboratory spectra of ammonia. wavenumber is $1/\lambda$; these axes are therefore from 0.83 to 1 micron.

suffered from up to 2.2" seeing, overly low resolution, and the instrument noise of NACO at L and M. They do not even detect the ammonia band at 2.21 microns.

2.1.2. Observations with GNIRS on Gemini North

The Gemini North InfraRed Spectrograph (GNIRS) is a spectrograph offering both long-slit and cross-dispersed spectroscopy. The long-slit capability is possible between 1.0-5.4 microns, within which it has a lowest spectral resolving power R of 1700, and two possible pixel scales, 0.15"/pix and 0.05"/pix. The slit can vary in width between 0.1 and 1.0 arc sec. The different pixel scales are provided by the four cameras, paired with 'long' and 'short' focal lengths to provide sensitivity to 'blue' (0.9-2.5 microns) and 'red' (2.8-5.4 microns) parts of the wavelength coverage (Elias et al. 2006a). There is also the capability for 1.0-2.5 micron imaging, though as the field of view is a vignetted keyhole, it is generally used for target acquisition. Both modes, spectroscopy and imaging, can be used together with the Gemini adaptive optics (ALTAIR) between 1-2.5 microns; at longer wavelengths, the adaptive optics' performance is poor (Elias et al. 2006b).

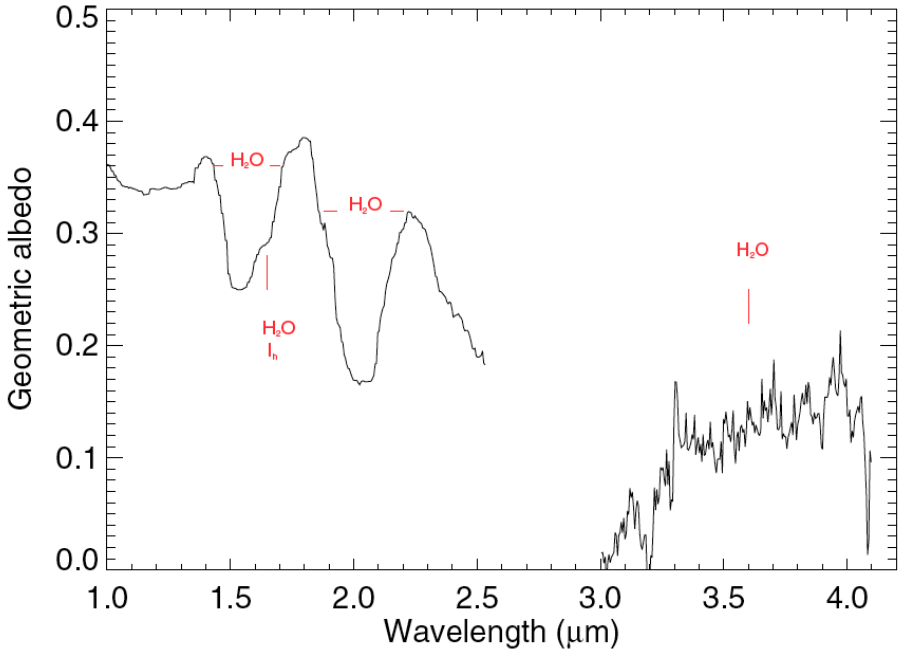

Figure 2.4 Protopapa et al. (2008): a spectrum of Charon in the near-infrared from one to four microns, taken with NACO on the VLT. Protopapa et al. (2008) noted that their lack of detection of the 2.21 micron ammonia feature was due to their low spectral resolution of 35 in J-band. The feature from ammonia that we wish to detect is between 3.0 and 3.1 microns (L and M), where the s/n of Protopapa et al. (2008) is very low, though in M their resolution was 200.

GNIRS' performance suggests that it has exceptional sensitivity in L-band (Elias et al. 2006b). The Gemini North telescope is ideal for observing a satellite at small angular separation from its primary in the mid-infrared, due to its high resolution and low emissivity. We were awarded two hours of queue time on GNIRS to take advantage of both these characteristics. We wished to see if these observations of Charon could provide data that improves on that of Protopapa et al. (2008).[3]

Resolving the ammonia-related absorption lines in the reflectance spectrum of Charon is not an easy task. These distinctive signatures are modifying the faint solar spectrum at L-band, as reflected from a 1200 km diameter object with a 10% L-band albedo that is at a distance of 32 AU. In this section, we describe the selection of our instrument parameters: we traded off spectral resolution to allow us both to detect the ammonia-related features and have a measure of their depth, after binning to improve the final signal-to-noise. Setting these parameters was an evolutionary process.

Refining the GNIRS parameters

We aimed to use GNIRS with long-slit spectroscopy at the lowest spectral resolution we could, as the signal-to-noise of TNOs is too low to obtain high spectral resolution (300 is considered very good). We also needed high angular resolution to make it possible to separate out the spectral contributions of Charon and Pluto, due to the overlap of their point-spread functions (PSF). For this we chose a configuration that would have small pixels

[3]We greatly appreciate the support provided by Gemini staff scientists Christopher Onken and Tom Geballe in the preparation of the Phase II observing plan.

for the spatial resolution, but a low spectral resolution, controlled by the choice of camera ("short" or "long") and slit width. The exact resolution was set by the actual object size.

The diameter of Charon would shrink if we used adaptive optics. With AO, it would be ~0.1" at L-band. The slit width must be wide enough to capture the wings of the PSF (all the light from the object). This needs to be combined with minimising the contribution to the background from the sky, which is bright in L-band; its contribution is controlled by the choice of slit width.

This meant that we were comparatively insensitive to the sky background conditions on the night. Initially we thought, as is usual for mid-infrared observing, that we would ask for a night with the lowest possible water vapour. As the telluric contribution is not problematic in the 3.0–3.1 micron region, we could relax this constraint.

To minimise flux contamination from Pluto, we needed to maintain target separation. The orbits of Pluto's satellites are nearly fully projected on the plane of the sky (i.e. we see Pluto close to pole-on), so Charon's angular separation from Pluto varies from 0.60" to 0.87" every three days in the course of its six-day orbit. We therefore asked for the observations to be taken on the days of maximum separation.

These observations aligned the slit along the orbital plane of Charon, so that the small motion of Charon in its orbit during the night would not affect its position relative to the sides of the slit. The change in position angle of Charon is about 3.5 deg/hr; this produces movement perpendicular to the slit of about 0.04 arcsec per hour. One reacquisition was requested in the 2-hour observing block, so that the position angle would be adjusted once (after moving ~ 2 pixels of the long camera).

We acquired on Pluto (V~ 13.4) in H- and H2-band. While normally the wavelength settings need to be consistent between the acquisition step and the science exposure to avoid problematic motion of the grating[4], in practise the sequences run without trouble (C. Onken, pers. comm.). As the L-band cuts off at 2.8 microns, we did not gain any advantage by setting the central wavelength below 3.3 microns.

As is normal for infrared observations, the sky background was found and removed by the technique of dithering: we asked for this to be between two positions along the slit in an A-B-B-A nodding, with single coadds at each position (and correspondingly doubled the ABBA iterations). This kept the revisiting of the sky at a rate under two minutes for optimal sky subtraction. The high background in the L-band allowed the use of the "bright" read mode, which reduced readout overhead and allowed more time for science exposures.

Spectra at similar airmass for removal of the solar and telluric lines from Charon's spectra were obtained from a nearby G2 standard star, observed for 5 minutes either before or after the observations of Charon. This gave a telluric at the airmass closest to the mean airmass of Pluto/Charon during the science observations.

During 2011B, Pluto-Charon were within the restricted observing range for Gemini North: they did not rise above 51 degrees elevation from Mauna Kea, but were above 40 degrees elevation for 3 hours after twilight ended, during August. We therefore asked for the

[4]GNIRS documentation suggests "Although the grating is bypassed by the acquisition mirror, keeping the central wavelength and grating selection fixed avoids the grating being moved between acquisition imaging and spectroscopy (and thus between the science target and telluric standard)."

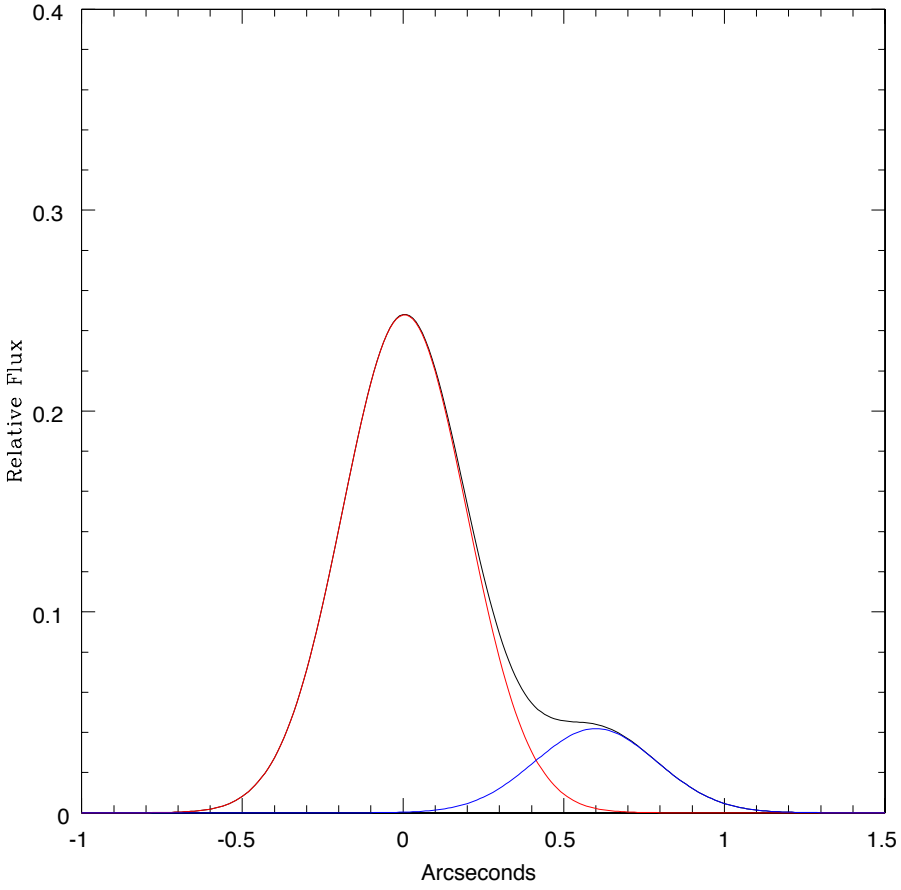

Figure 2.5 1-D case of two flat surface brightness distributions with a factor of 2 difference in flux and diameter, separated by 0.6", in 0.45" seeing. Pluto is in red, Charon in blue. About 80% of the total Charon flux is found at $x >= 0.42$", although 10% of that enclosed flux is from Pluto; this is the worst-case situation as it is 1D and the physical situation is 2D. Courtesy C. Onken.

observations in two-hour blocks: accounting for time to acquire and observe the standard star (18 + 5 minutes), time to acquire Charon (24 minutes), and a 10% overhead while on target, this allowed approximately an hour of integrations on Charon in each block.

We debated the use of adaptive optics, as AO would improve our target separation. Pluto is a magnitude brighter than Charon, and can serve as a natural guide star. (Both Pluto as the NGS and Charon required non-sidereal tracking). The Pluto-Charon system is also currently in the galactic plane, providing numerous nearby stars that could alternatively be used for NGS-AO. The field density of stars is high, but not enough to cause confusion. While the use of AO would require the night's image quality to be in the 70th percentile and under photometric conditions, this would be necessary without AO as well.

However, using AO would incorporate the 3.9 magnitudes higher L-band background of the Altair AO module: an AO target has to be nearly forty times brighter to provide the same s/n, but the AO's shrinking of the size of the PSF only increases the flux within the slit by a factor of three. The low elevation meant that the best possible seeing would give a Charon FWHM of ~ 0.45", with little difference in IQ 70 conditions. With the 0.45" seeing, Pluto and Charon would not be entirely separated by using AO (Fig. 2.5). However, binning would minimise the AO-induced decrease in signal.

We therefore decided not to use AO. We instead planned to use the more complex technique of spectroastrometry (Bailey 1998; Porter et al. 2004) in the data reduction. This technique should be able to allow us to make a clean detection of the spectral differences between Pluto and Charon, even in the absence of a clear separation. Data artefacts would be minimised using techniques of Brannigan et al. (2006).

We had some confusion during the preparation of the proposal ascertaining what would be a suitable integration time to provide s/n to fulfil our requirements. Charon has a V magnitude of 15.89 and V albedo of 0.37; according to the data of Protopapa et al. (2008), the L-band albedo is ~ 0.1, so with the colour correction, Charon has a similar magnitude in L to that in V.

We initially considered using the long 0.10"/pix camera with the 10 l/mm grating and the 0.15" slit. This would minimise the contribution from the sky, as the smallest slit available for the short camera is 0.3".

At this magnitude, according to GNIRS' Integration Time Calculator (ITC), with three hours of observation we obtain a signal-to-noise per spectral pixel of ~ 0.8 at 3 to 3.1 microns. The spectral pixels are 0.970nm while the feature we wish to measure is about 100 nm wide. This means we could bin, compare against the continuum, and improve this signal-to-noise to about 8, which would allow an unambiguous detection of the 3.1 micron ammonia band, given its predicted depth (Fig. 2.2).

This seemed quite reasonable a request to make of the Gemini time allocation committee. However, Gemini technical staff were interested to see what effect there would be if the ITC was tried with the prescription for AO-mode S/N calculations, redid the calculation, and found that the exposure time required was roughly 2300 hours (C. Onken, pers. comm.):

$$t = 1hr\left(SN_{target}/5 * SN_{ratio} * 10^{-0.4(L_{Charon}-9.7)}\right)^2 \quad (2.1)$$

where the s/n of the target was 0.8/pixel, the s/n ratio (between 3.5um and 3.05um) was taken as 1.0, and $L_{Charon} = 15.9$. This was a significant discrepancy from our initial calculations without the use of AO, thought it is mostly due to the very high (3.9 magnitudes) L-band background of the Altair AO module.

This calculation by C. Onken led us to realize that despite the GNIRS ITC not yet being able to do AO-incorporating calculation, the *default* of no-AO requires the user to input a source brightness 0.5 mag fainter, which we had not done in our initial calculation of the time required that had led us to think it was possible to make the observation in only three hours. With our choice to go without AO, and with the target (0.5 + 0.24) mag fainter[5] 20th percentile seeing, any level of water vapor, and observing instead for considerably longer with 36 x 600s integrations (i.e., 6 hours on-source), the ITC indicated a mean s/n of ~ 0.8/pixel across the 3.0-3.1 micron range.

After this recalculation, we determined to relax the request for 20% seeing, as with our suggested observing strategy of keeping the observations within two-hour blocks, this would require 12 hours in total (after including the telescope's overhead for this instrument). This would use the start of 6 IQ20 nights, as many as might be expected within two months. This was likely to stretch the generosity of the Australian Gemini time allocation committee.

[5] 0.24 mag fainter for the flux recovery being at the worst-case 80%.

We instead therefore submitted a proposal that requested 7 hours on-target with IQ better than 70th percentile and water vapor "Any" conditions; a total requested time of 14 hours (including overhead). However, the proposal could then be completed within 7 nights that had much more likely occurrence of observing conditions. While this would push the ammonia feature s/n down to ~ 0.6 per pixel, it should be detectable.

In the Phase II step of programming the observations into the Gemini queue, we reconsidered the choice of settings. The novelty of our choice of long 0.10"/pix camera, with the 10 l/mm grating and the 0.15" slit, without AO, required new arcs, examples and flats to be added to the GNIRS library.

We decided that the loss of light from Pluto/Charon would more than offset the reduced background from using the 0.3 or 0.45 arcsec slit. This slit also matched the seeing; on the long camera it was 9 pixels wide.

The 4.5 times wider slit meant that the exposure times should in principle be shortened;[6] however, as we were interested only in the short wavelength part of the L band, we were able to increase the exposure time considerably, and use 60 seconds. The flats required a 9 second exposure.

The s/n can be the same with either the 10 l/mm grating, 0.05" pixels, and 0.45" slit, or with the (higher spectral resolution) 32 l/mm camera, 0.15" pixels, and same slit The 10 l/mm grating, with a maximum spectral resolution of ~ 1800, + long camera was here equivalent to the 32 l/mm (which gives the same spectral resolution for the short [i.e., low spatial resolution] camera). The first configuration required summing the spectra in many more rows, but that was as intended for spectroastrometry.

2.1.3. Results

The two hours of Gemini queue time we were granted was in Band 2, under program GN-2011B-Q-40; the ITAC noted that this was all that was available in this restricted RA range for a Band 2 allocation. Gemini observed this program in one block on 18 July 2011, taking 1 hour and 54 minutes on Pluto/Charon with GNIRS with the 10 l/mm grating and 0.45" slit (Table 2.1). During this time Pluto/Charon were close to their maximum elevation for the night, at airmass 1.3 to 1.5. A standard star was observed for L-band spectra both before (HIP85908) and after (G0V standard HIP94394) the Pluto/Charon data were acquired, which provided telluric subtraction spectra (Table 2.1). This night's worth of data became available on 23 July.

The good-quality seeing due to the crisp clear night (~ 6°C, windspeed < 0.2 m/s, 13 – 28% relative humidity) meant that Pluto/Charon had overlapping PSFs with centroids 11-13 pixels apart (Fig. 2.6). This corresponded well with the separations of 12.5-12.7 pixels predicted from their astrometry by JPL Horizons. In single raw images, Pluto, which we expect to be ~ 0.1'' across, is 2 pixels across.

The GNIRS instrument had recently been moved from Gemini South to North, so the Gemini data reduction software was not available for the data. We built a stack of the ninety

[6] According to the exposure table, with the long camera, 0.1"slit, no AO, the maximum exposure time at the long wavelength end of the L band is 180 sec. Since we use a 4.5x wider slit, the individual exposures on source should not exceed 40 seconds, and were recommended to be 30 seconds to be safe.

Table 2.1 Observations of Pluto and Charon acquired by Gemini GNIRS in L-band with the 10 l/mm grating and 0.45″ slit for program GN-2011B-Q-40.

Set UT	Target	File #	Filter	Slit/Acquisition	Int(sec)/LNR/Coadds	Observer notes
08:19:21	HIP85908	50	H	0.45	15.0/1/1	
08:20:02	HIP85908	51	H2	ACQ	0.5/1/5	
08:23:23	HIP85908	52	H	0.45	15.0/1/1	
08:24:04	HIP85908	53-58	H2	ACQ	0.5/1/5	
08:32:03	HIP85908	59	H2	0.45	0.5/1/5	
08:34:23	HIP85908	60	H	0.45	15.0/1/1	
08:37:22	HIP85908	62-64	H2	0.45	0.5/1/5	
08:43:29	HIP85908	65-72	L	0.45	30.0/1/1	saturated
08:51:43	HIP85908	73-76	L	0.45	20.0/1/1	reduced to 20s
08:58:23	Pluto	77	H	0.45	15.0/1/1	
08:59:04	Pluto	78-82	H	ACQ	0.6/1/5	
09:08:50	Pluto	83-84	H	0.45	0.6/1/5	
09:11:04	Pluto	85-128	L	0.45	60.0/1/1	
10:02:19	GCALflat	129-138	L	0.45	0.45/1/1	
10:05:55	Pluto	139	H	0.45	15.0/1/1	
10:06:37	Pluto	140-143	H	ACQ	0.6/1/5	
10:12:28	Pluto	144-146	H	0.45	0.6/1/5	
10:15:18	Pluto	147-190	L	0.45	60.0/1/1	
11:42:51	GCALflat	191-200	L	0.45	0.45/1/1	
11:46:22	HIP94394	201	H	0.45	15.0/1/1	
11:47:04	HIP94394	202-203	H2	ACQ	0.2/1/5	
11:48:41	HIP94394	204	H2	0.45	0.2/1/5	
11:50:27	HIP94394	205-212	L	0.45	15.0/1/1	

[a] File # is the acquisition number of the image on the night (the three digits at the end of Gemini's "original file name" in the Gemini data archive).

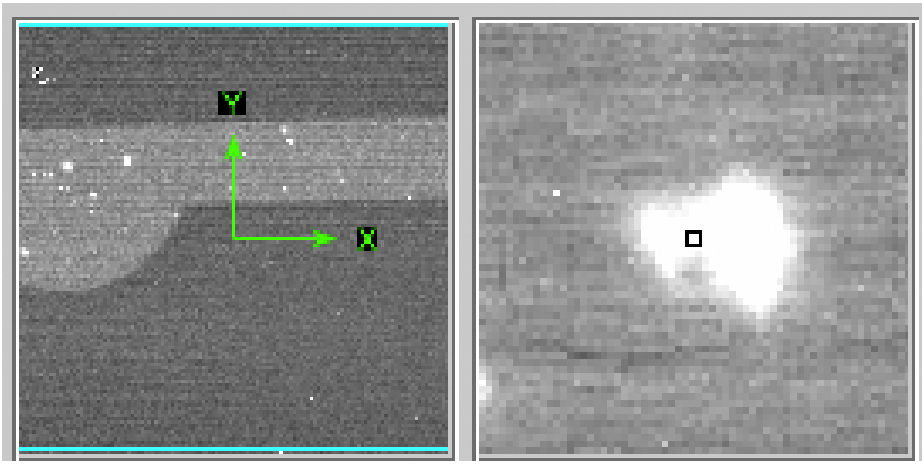

Figure 2.6 Pluto and Charon in the acquisition field of GNIRS in H-band. The long narrow field shown corresponds to the position of the slit as it was taken on the target, as GNIRS has a flip-in mirror that allows positioning of a target in the slit without movement of the grating, prism or camera (GNIRS Target Acquisition).

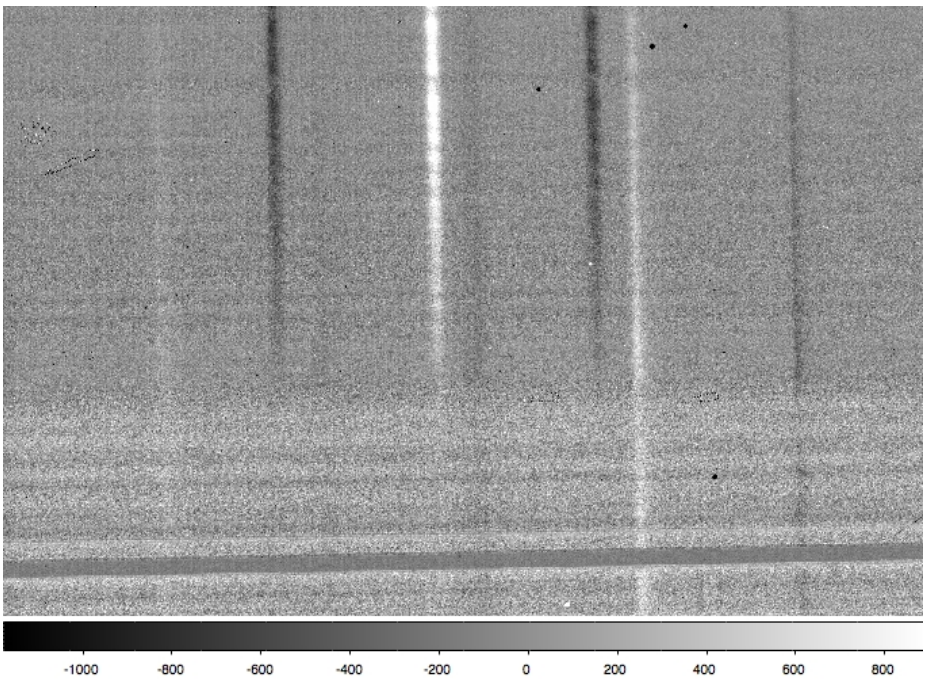

Figure 2.7 A dither-cancelled stack of the ninety Pluto-Charon L-band spectra made with one-minute integrations with GNIRS on Gemini North (exposures 85-128 and 147-190 in Table 2.1). As there is a blank spot in the centre of the spectrum, summing over the column of the stacked images produces two peaks of Pluto, rather than the normal widening of the peak.

Pluto/Charon spectra (exposures 85-128 and 147-190 in Table 2.1), scripted by accounting for and cancelling the displacement of the ABBA dither (Fig. 2.7). However, Charon was not visible in this stack. The width of the Pluto line in this stack is 15-17 pixels, which may imply that the initial coadding was faulty (the tilt of the spectrum has to be accounted for and the author-written script may not have accounted for this as effectively as would the Gemini GNIRS reduction package). Of primary importance is that the stack does not show Charon as a shoulder on the line of Pluto's light (Fig. 2.8) when the stack shown in that figure is column-summed; in that summed profile Charon must appear to the left of Pluto, as indicated in Fig. 2.6, and no such signature was present. If Charon is there, it is exceedingly faint.

The lack of detection of Charon prevents further data reduction, but emphasises the difficulty of this observation: we have trialled a set of parameters of GNIRS that may make it possible to try for the detection more effectively in the future. The peak flux count on Pluto in the data is about a thousand, so to ensure detection we would suggest increasing the total integration by a factor of ten.

2.1.4. Future work

Although the program was cut back to a smaller allocation than requested, the data provide a feasibility test. This will strengthen a future proposal to acquire the full dataset. Since the data were released, the GNIRS IRAF package has been extensively updated, and also now accounts for the instrument being on a different telescope to when it was written; the data should also be re-reduced with this package. Once this re-reduction is done, the

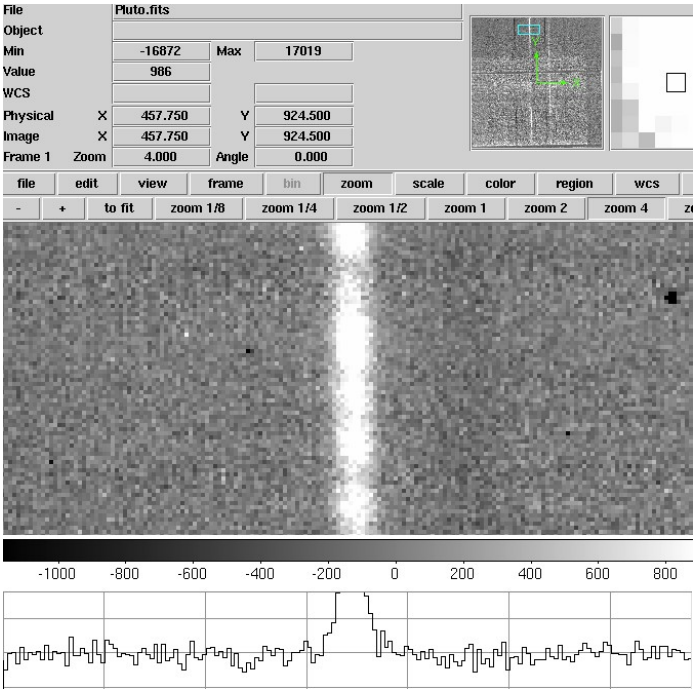

Figure 2.8 A cross-section of the profile of the Pluto-Charon line in the summed (stacked) columns Fig. 2.7: there is no shoulder on the line that would indicate photons from Charon.

column-summed profile of the image stack would be fitted to quantify the lack of detection of Charon (number of sigma at which there was no deviation from a single PSF). It would also be necessary to confirm that the counts received on Pluto and Charon in these two hours of integration matched that expected from the current GNIRS ITC to ensure the predictions of the ITC matched the observations before any re-proposal to Gemini.

2.2. Investigating the newly discovered TNO 2012 DR_{30}

Part of this section has been published as part of an article in Astronomy and Astrophysics: Kiss et al. (2013)

The most distant parts of the outer Solar System are populated by hundreds of thousands of small worlds, gravitationally scattered to their present orbits at the end of the dispersion of the early nebula. These objects have not experienced strong radiative thermal alteration since their scattering by a giant planet. However, their surfaces have been gradually modified by the slow-acting, incompletely understood, processes of cosmic ray and micrometeoroid bombardment. While in principle these distant objects are excellent probes of the nebular conditions during the formation of the Solar System, their surface evolution has hidden their otherwise fresh, unaltered primordial material.

We do not see such objects at Oort cloud distances due to their small size. Occasionally, one is perturbed and its perihelion drops into the inner Solar System: they are then observed only after becoming comets, or active Centaurs, when they are outgassing.

In late February 2012, the Siding Spring Survey discovered a new TNO: 2012 DR_{30} (MPEC 2012-D67). This TNO has a fascinating orbit, well secured by four oppositions of observations.[7] It is severely eccentric, steeply inclined, and has a semimajor axis of greater than a

[7] a = 1104 AU, e = 0.9868, i = 78.0° according to the Minor Planet Center on 16 December 2012.

thousand AU that suggests its origin is cometary. However, its high perihelion at 14.5 AU is distinctly non-cometary. This is not the orbit of a typical Centaur, or of a scattered disk object (§ 1.2). We suspect that 2012 DR_{30} is recently injected from the Oort cloud, and has gravitationally scattered off a giant planet into its present orbit before ever coming close to the Sun (Kiss et al. 2013).

Interestingly, 2012 DR_{30} was not discovered to be on its current orbit until it passed onto the Siding Spring Survey's fields at $-17°$ declination and at magnitude $V \sim 18.8$. Shortly after this designation was assigned (MPEC 2012-D67), the Minor Planet Center announced in MPEC 2012-E01 that the object's arc could be linked to that of a lost previous discovery: 2009 FW_{54}, made by Spacewatch at Steward Observatory on 2009-03-31, which had been lost after six observations. With archival searching, previous detections dating back to 5 April 2000 were unearthed which filled out the orbital arc. The 2008 observations by Purple Mountain, Mt Lemmon Survey, Lowell's LONEOS and Spacewatch were within a few tenths of a magnitude of the discovery magnitude[8]. 2012 DR_{30} was then approaching perihelion and moving at within an arcsecond per hour of its $\sim 11''$/hr motion rate at discovery, just post-perihelion; this motion rate was too slow for it to be detected by Catalina's northern G96 (Mt Lemmon) and 703 asteroid surveys (R. McNaught, pers. comm.). No survey has a 100% detection efficiency; in the earlier TNO surveys of Trujillo & Brown (2003), it may simply have fallen through the cracks.

As a new discovery, little was known about 2012 DR_{30}. Director's discretionary observations on Herschel in May 2012 provided thermal emission measurements; combined with 2.2m multi-colour observations at La Silla which gave a magnitude of $V = 19.254 \pm 0.023$, and $H_V = 7.095 \pm 0.063$, the diameter of 2012 DR_{30} is 184 ± 2 km, taking the best-fit thermophysical pole-on model (Kiss et al. 2013). This makes it among the five largest known Centaurs, or given its evolutionary origin, the largest comet ever seen.

As it is just past perihelion, 2012 DR_{30} is well placed for observations to probe the properties of this large body. We began by obtaining photometry for a lightcurve of 2012 DR_{30}, using the Faulkes South 2 m telescope, which could provide this TNO's rotational period.

2.2.1. Observations with the Faulkes South 2m

Magnitude variation with time provides information on an object's rotational period. A lightcurve can also show if there are significant albedo variations on the object, eg. Haumea's red spot (Lacerda 2010).

We obtained visible-light imagery of 2012 DR_{30} with queue observations on the 2 m Faulkes South telescope at Siding Spring Observatory, NSW.[9] The Spectral camera of Faulkes South that we used has a plate scale of 0.304 arcsec/pixel, with a 4kx4k CCD array, giving a field of view of 10.5 arcmin.[10]

We observed 2012 DR_{30} through the Sloan Digital Sky Survey r' filter on four nights, as detailed in Table 2.2.[11] On each night, consecutive 300 s exposures were obtained with 2012

[8] Observations of 2012 DR_{30} recorded at the Minor Planet Center

[9] Las Cumbres Observatory Global Telescope Network: 2m.

[10] Las Cumbres Observatory Global Telescope Network: Technical Data for Spectral camera.

[11] We appreciate the assistance of Daniel Bayliss in donating several hours of his Faulkes time.

DR_{30} centred on the array; the 2x2 binning set a readout time between exposures of 22 s. The rate of motion of 2012 DR_{30} across the sky was 0.9″/hr (a quarter-pixel, 75 milliarcsec, in 5 minutes), which kept it well within the seeing disk of ∼ 2″ over each integration. Due to the low altitude of 2012 DR_{30}, the longest continuous set of observations were made over less than two hours. 34 integrations were made in total, excluding nine images where the seeing deteriorated below where 2012 DR_{30} could be detected.

Bias subtraction, flatfielding and astrometry were provided by the standard Faulkes queue pipeline. The flatfielding varied in quality due to proximity to the Moon on some of the nights, creating a pocked "golf course" effect in places, but 2012 DR_{30} did not fall on any problematic locations in these observations. We then used `SExtractor` (Bertin & Arnouts 1996) to obtain the flux of 2012 DR_{30} from the reduced images.

We were puzzled to find that the observed position of 2012 DR_{30} differed from its predicted position by a consistent offset of about 12 arcseconds (Table 2.2). This seemed oddly large for a multi-opposition secured orbit. We confirmed that this difference was real by image-by-image blinking & manual checks against JPL Horizons. This verified the output of our script, which obtained 2012 DR_{30}'s predicted positions by querying Horizons based on the timestamp of the header of each image. The offset did lead us to wonder if the Faulkes pipeline had a header timestamp error, but we could find no evidence of such an error such as the keyword being for the start or midpoint rather than the end of the exposure, and such a timestamp error would have to be substantial indeed to produce 12″ of variation. The astrometry world coordinate system provided by Faulkes we double-checked via astrometry.net and could not find any problem there.

The 10 arcmin field of view provided ample suitably bright field stars, from which we selected eleven to act as comparison stars and cancel the effects of atmospheric variability (Table 2.3 and Fig. 2.9). The selection was based on their photometric stability, lack of saturation, no blends or other close stars, and their spatial distribution on the field; the mutual relative photometry of these eleven stars varied by less than 0.01 mag across all the observations. We then measured the differential brightness variation of 2012 DR_{30} against these stars.

The field on which 2012 DR_{30} fell during our observations (R.A. = 10^h16^m, decl. = $-17°05^m$) was too far south to be within the SDSS photometric catalog. We instead used the AAVSO Photometric All-Sky Survey (APASS) Data Release 6 survey catalog for absolute calibration of the magnitudes of the comparison stars. Four had matches within 2.2″-0.5″ in the catalogue (Table 2.3); these matches were confirmed by visual inspection of the images. This catalogue match also confirmed that the astrometry on the field did not have a constant offset in declination, as might be suggested by the shift in 2012 DR_{30} from its expected position, supporting our conclusion that the image WCS was correctly applied.

The known catalogue magnitudes allowed us to tie the zeropoint of the differential variation of 2012 DR_{30} to an absolute magnitude. The scatter in the shift between the observed stellar magnitude and the catalogue value for the four comparison stars was 0.2 magnitudes; we therefore note that the internal precision in the relative photometry is much greater and provides a better measure of the variability of 2012 DR_{30}.

Table 2.2 Astrometry of 2012 DR_{30} from Faulkes South 2 m r′-band imaging over four nights in 2012.

UT of observation	Predicted RA	Predicted Dec	observed RA	observed Dec	offset
2012-05-28 08:28:06.355	10:16:46.65	-17:05:44.3	10:16:46.47	-17:05:56.5	0:00:12.5
2012-05-28 08:33:26.626	10:16:46.65	-17:05:44.2	10:16:46.47	-17:05:56.4	0:00:12.5
2012-05-28 08:38:47.220	10:16:46.65	-17:05:44.2	10:16:46.47	-17:05:56.4	0:00:12.4
2012-05-28 08:44:08.066	10:16:46.65	-17:05:44.1	10:16:46.47	-17:05:56.3	0:00:12.5
2012-05-28 11:56:14.191	10:16:46.65	-17:05:41.7	10:16:46.43	-17:05:53.8	0:00:12.5
2012-05-28 12:01:34.738	10:16:46.65	-17:05:41.6	10:16:46.44	-17:05:53.6	0:00:12.4
2012-05-28 12:06:55.562	10:16:46.65	-17:05:41.5	10:16:46.44	-17:05:53.5	0:00:12.3
2012-05-28 12:12:16.716	10:16:46.65	-17:05:41.5	10:16:46.43	-17:05:53.5	0:00:12.4
2012-05-28 12:17:37.018	10:16:46.65	-17:05:41.4	10:16:46.44	-17:05:53.3	0:00:12.3
2012-05-28 12:22:57.712	10:16:46.65	-17:05:41.3	10:16:46.44	-17:05:53.1	0:00:12.2
2012-05-30 09:06:03.224	10:16:47.13	-17:05:10.4	10:16:46.93	-17:05:22.6	0:00:12.5
2012-05-30 09:11:23.703	10:16:47.13	-17:05:10.3	10:16:46.94	-17:05:22.5	0:00:12.5
2012-05-30 09:16:44.081	10:16:47.13	-17:05:10.3	10:16:46.94	-17:05:22.5	0:00:12.5
2012-05-30 09:22:04.962	10:16:47.13	-17:05:10.2	10:16:46.94	-17:05:22.4	0:00:12.5
2012-05-30 09:27:25.380	10:16:47.13	-17:05:10.1	10:16:46.94	-17:05:22.3	0:00:12.5
2012-05-30 09:32:45.671	10:16:47.13	-17:05:10.1	10:16:46.94	-17:05:22.3	0:00:12.5
2012-05-30 09:38:06.124	10:16:47.14	-17:05:10.0	10:16:46.94	-17:05:22.2	0:00:12.5
2012-05-30 09:43:29.790	10:16:47.14	-17:05:10.0	10:16:46.94	-17:05:22.2	0:00:12.5
2012-05-30 09:48:51.063	10:16:47.14	-17:05:09.9	10:16:46.95	-17:05:22.2	0:00:12.6
2012-05-31 08:54:21.306	10:16:47.75	-17:04:56.1	10:16:47.56	-17:05:08.2	0:00:12.4
2012-05-31 09:10:25.284	10:16:47.76	-17:04:55.9	10:16:47.56	-17:05:08.0	0:00:12.5
2012-05-31 09:15:45.913	10:16:47.76	-17:04:55.9	10:16:47.56	-17:05:08.0	0:00:12.4
2012-05-31 09:37:09.023	10:16:47.77	-17:04:55.7	10:16:47.57	-17:05:07.8	0:00:12.5
2012-05-31 09:42:30.113	10:16:47.77	-17:04:55.6	10:16:47.57	-17:05:07.9	0:00:12.6
2012-05-31 09:47:50.256	10:16:47.78	-17:04:55.6	10:16:47.58	-17:05:07.7	0:00:12.5
2012-05-31 09:53:11.190	10:16:47.78	-17:04:55.5	10:16:47.58	-17:05:07.7	0:00:12.5
2012-05-31 10:14:33.638	10:16:47.79	-17:04:55.3	10:16:47.60	-17:05:07.5	0:00:12.5
2012-05-31 10:19:54.273	10:16:47.79	-17:04:55.3	10:16:47.59	-17:05:07.4	0:00:12.5
2012-05-31 10:25:15.577	10:16:47.80	-17:04:55.2	10:16:47.59	-17:05:07.3	0:00:12.5
2012-05-31 10:30:35.888	10:16:47.80	-17:04:55.2	10:16:47.60	-17:05:07.2	0:00:12.4
2012-05-31 10:35:56.461	10:16:47.80	-17:04:55.1	10:16:47.59	-17:05:07.3	0:00:12.6
2012-05-31 10:41:17.404	10:16:47.80	-17:04:55.1	10:16:47.60	-17:05:07.1	0:00:12.4
2012-05-31 10:46:38.478	10:16:47.81	-17:04:55.0	10:16:47.60	-17:05:07.2	0:00:12.5
2012-06-14 10:17:19.847	10:17:23.22	-17:04:27.9	10:17:23.03	-17:04:39.7	0:00:12.1

[a] RA are in H:M:S, declination in D:M:S, offset in degrees. The predicted positions are from JPL Horizons. Measured positions of 2012 DR_{30} have uncertainties of 0.1″ or slightly better.

Table 2.3 Comparison stars selected in photometric reduction of Faulkes South 2 m r′-band imagery of 2012 DR_{30}.

Star ID	flux[a]	APASS m_r	RA (hours)	Dec (deg)
41	97462.2 ± 212.4	16.354 ± 0.047	10:16:38.30	-17:10:04.0
61	113369.1 ± 219.5	16.214	10:16:56.87	-17:09:14.7
79	66749.4 ± 197.9		10:16:57.61	-17:08:23.0
82	95622.8 ± 211.5		10:16:33.54	-17:08:20.4
148	165926.6 ± 241.4	15.629 ± 0.028	10:16:37.92	-17:03:09.4
175	65117.2 ± 196.9		10:16:52.14	-17:04:19.7
210	101109.8 ± 214.0		10:16:31.96	-17:03:57.4
216	64865.0 ± 197.0		10:16:39.52	-17:04:55.7
252	106017.4 ± 216.1		10:16:59.19	-17:05:36.1
260	133196.7 ± 227.9	15.983 ± 0.102	10:16:33.02	-17:06:06.9
273	66359.9 ± 197.7		10:16:33.29	-17:06:25.8

[a] SExtractor's FLUX_APER: flux vector within a fixed circular aperture. Star ID: number assigned by SExtractor after extracting all sources on the image.

2.2.2. Results

We used the Faulkes comparative photometric measurements of 2012 DR_{30} to construct a light curve (Fig. 2.10). This showed very little variation, with an upper limit of 1σ variability of 4 millimag from the standard deviation of the m_r measurements. The comparative photometry is given after Budding & Demircan (2007) as:

$$K_{comparative} = \frac{flux_{DR_{30}} \pm \sigma_{photon-noise}}{\sum flux_{stars} \pm \sqrt{\sum \sigma^2_{stars}}} \tag{2.2}$$

where K is a constant that sets the zeropoint of fluctuation; it was set to the first observation of 2012-05-31, which was roughly centred in the variation over all dates. The uncertainty of the individual magnitude measurements shown in Fig. 2.10 are dominated by the APASS calibration error, increasing them to 50 millimag. We conclude that 2012 DR_{30} shows no light curve variability above the 50 millimag level in r.

We tried to fit a rotation period to 2012 DR_{30}; the periodogram showed aliases only at one- and half-day periods, which would be spurious effects from the cadence of the observations, a bias inherent to ground-based lightcurve observations. It was interesting that other authors on Kiss et al. (2013) noted that the thermal fluxes measured with the space observatories Herschel and WISE varied between epochs and were consistent with either a sidereal period of 6 hrs or 24 hours. Centaur rotational periods are generally shorter than 27 hours (that of the longest known, (60558) 2000 EC_{98} (Rousselot et al. 2005)), and mostly < 11 hours (e.g. the ensemble study of Thirouin et al. (2010) found an average rate of 7.3 hours for Centaurs), so these two periods do encompass the known range of Centaur rotational periods.

It would be useful as future work to obtain a further light curve in multiple colours (g and r) to confirm if there is any more subtle colour-dependent variability, which could indicate either surface composition or topographic variation.

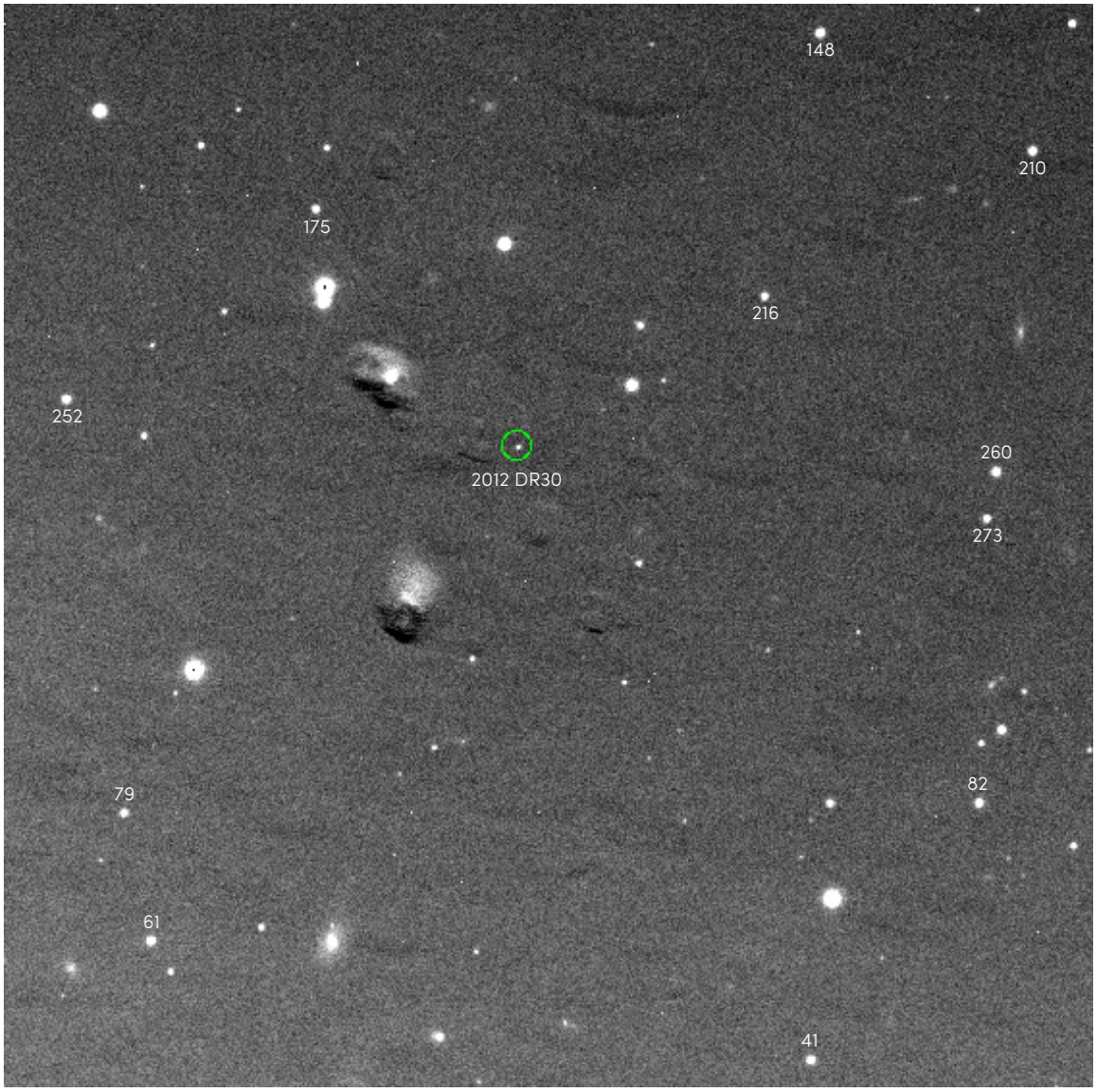

Figure 2.9 Example of observations of 2012 DR_{30} with Faulkes South 2 m r′-band imaging. The comparison stars selected in the photometric reduction as listed in Table 2.3 are labelled with the "star ID" given in Table 2.3. Note the "pocking" due to the proximity of the Moon affecting the flatfielding.

2.2.3. Future work: observations with GeMs/GSAOI

No observations have yet been made with large-aperture telescopes to see if 2012 DR_{30} has any comet-like coma. None were detected in the images from a 2 m, but 2012 DR_{30} is far from the Sun; it will not be as lively as a Sun-approaching comet, but could show minor Centaur-like activity. With high-resolution AO NIR imaging of 2012 DR_{30}, we would be able to detect spalled fragments and gas streamers. 2012 DR_{30}'s body may even be partially resolved; its core has an expected angular width of $\sim 0.06''$. This would provide detail on the size, mass, thermal physics, and composition of 2012 DR_{30}.

We requested science verification time and were granted engineering time for H-band MCAO imaging of the new GeMs/GSAOI instrument on Gemini South[12]. We offered observing

[12]These were anticipated for mid-January 2013 but ended up not being possible to schedule. The planned observations did not take place. However, as of mid-2013 this kind of coma check on 2012 DR_{30} has not come

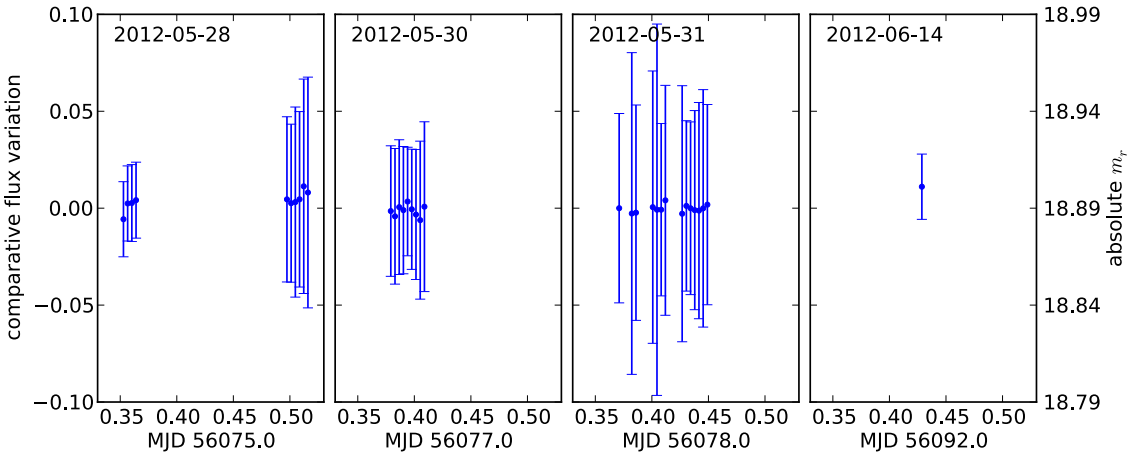

Figure 2.10 Comparative photometry of 2012 DR_{30} over four nights. The error bars for each point are given relative to the internally consistent photometry (left ordinate), and are dominated by the photon noise, found via SExtractor's FLUXERR_APER (RMS error vector for aperture flux) values. The absolute magnitude (right ordinate) is tied to the APASS catalogue, which had up to an 0.2 m_r variation in the shift required for the standard stars, so it is provided for guidance rather than high precision.

options both with non-sidereal or with sidereal tracking, as the non-sidereal capabilities of GeMs/GSAOI have not yet been commissioned on objects other than Saturn's moons. The large field of GeMS+GSAOI would make acquisition of 2012 DR_{30} straightforward; the positional uncertainty of a few arcseconds may have been why 2012 DR_{30} could not be acquired with NIRC2's 7″ FOV on Keck. Imprecise pointing on the ephemeris is therefore quite acceptable, regardless of the type of tracking.

The cadence of observations with GeMs/GSAOI is set by two requirements. The sky motion of 2012 DR_{30} must be apparent, to ensure we can correctly identify it; this can be satisfied by only a few minutes of observing time, thanks to 2012 DR_{30}'s late-2012 motion rate of ~ 11 arcsec per hour. Detecting the motion of any ejected particles is the primary control on the observing time. Over 30 minutes, spalled fragments moving at roughly 1-10% of the TNO's escape velocity could be detected. We therefore asked for as many H-band images as could be taken to give 30 minutes on 2012 DR_{30}, dithered by 4″ in a 2x2 box dither pattern, for later sky subtraction. This background removal will have to be very careful to preserve the extent of any coma around the TNO.

2012 DR_{30} brightness in H-band is set by its colour, which is very blue: $B - V$ of (19.901 − 9.254 = 0.65) (Kiss et al. 2013), kin to shiny-blue water ice (cf. Haumea, $B - V = 0.64$ (Snodgrass et al. 2010)). 2012 DR_{30}'s H-band magnitude will therefore be brighter than 16.6. AO only shrinks the central core; for a core with that magnitude surrounded by a magnitude-fainter per square arcsecond coma with perfectly even brightness distribution, we calculated that for Haumea-blueness,[13] ~ 150 10-second exposures will provide SNR~ 8 per 0.01 sq. arcsec, sufficient to detect coma and fragments 1/10th the diameter of 2012 DR_{30}.

into the literature

[13]The exposures for 2012 DR_{30} had already been submitted before the exact colour was found.

CHAPTER 3

The Uppsala southern sky survey

> The number of stars recorded per plate was appalling.
> ...Searching beyond the seventeenth magnitude would appear prohibitive; the work of blink examination would increase roughly in proportion to the number of stars.
>
> – Clyde Tombaugh
> 1961

This work has been prepared for publication in the Astronomical Journal, with authors Bannister, M. T., Brown, M. E., Schmidt, B. P., Francis, P. J., McNaught, R. H., Garradd, G. J., Larson, S. M. and Beshore, E. C. It will be submitted in early 2013.

In the previous chapter, we discussed some of the possibilities available from understanding the properties of individual trans-Neptunian objects. In this chapter, we move to the larger picture: the process of sweeping the sky to consolidate our understanding of the overall abundance of TNOs.

As discussed in § 1.3.1, surveys of the sky have not yet covered the high-latitude regions of the southern sky. A survey of this region to sufficient depth to sample well down the size distribution will add significantly to our understanding of the high-inclination TNO population. As a > 1 m-aperture wide-field telescope was not available in Australia to make this kind of wide and shallow survey, we looked for existing wide-field observations that might offer sufficient data.

The Uppsala telescope is an 0.5 m enclosed-tube equatorial mount Schmidt reflector at Siding Spring Observatory (SSO) in northern New South Wales. Placed at Mt Stromlo Observatory in 1957 as the southern telescope of the Uppsala Observatory in Sweden, it was moved to SSO in 1982 after the Swedes finished their programs of observation.

The Uppsala was completely refurbished in the early 2000s by the Catalina Sky Survey, who wanted to extend their United States-based search for near-Earth asteroids (Larson et al. 1998; Christensen et al. 2012) to the Southern Hemisphere. It has been dedicated since 2004 to the Catalina group's observing program for near-Earth asteroids, the *Siding Spring Survey*

(Larson et al. 2003), which remains the only such survey in the Southern Hemisphere. It is the most successful asteroid detection survey of its telescope size[1], and by January 2013 had also detected 92 comets,[2] including Comet McNaught (C/2006 P1), the Great Comet of 2007. Since mid-2008, the data have also been provided to Caltech for the Catalina Real-Time Transient Survey (Djorgovski et al. 2011).

These observations with the Uppsala have produced more than five hundred thousand images of the southern sky. This could potentially form a TNO survey of the bright end of the brightness distribution, though no such archival survey has ever been created on such a scale.

In this chapter, we first describe the basic parameters of the Uppsala survey operation (§ 3.1). We then collate the observational characteristics of the survey data (§ 3.2): from this assessment, we determine that its rich temporal coverage permits its resampling at a cadence that can be used to search for TNOs. This, together with the dataset's other observational characteristics, make an archival TNO survey feasible.

Given this possibility, we conceive and develop a processing pipeline to transform the data from that for an asteroid survey to a TNO survey (§ 3.3). We discuss the results and the intricacies of running this pipeline on the rawness of a large, undocumented dataset in § 3.4. We conclude our assessment and processing of the Uppsala survey in § 3.5, with consideration of the possibilities for future work on the data.

3.1. Uppsala Survey operation

The Siding Spring Survey is less automated than the other Catalina operations in California and Arizona. Two observers alternate ten-day shifts during which they schedule the observations, operate the telescope, and monitor the Catalina data pipeline's moving object output as each set of fields are observed. Each night, the observer selects a group of adjacent fields from the field list (Appendix §A.1) for observation. This selection is based on weather, time of lunation, and the area searched in the last week by the other major asteroid surveys.[3]

In the refurbishment of the Uppsala telescope by the Catalina group, the telescope mount was refitted with digital encoders, and the photographic plate holder replaced with a Newtonian-focus mounted 4k x 4k CCD. This has a field of view of 4.21 square degrees (123.3 x 122.9 arcminutes)[4] and a plate scale of 1.8″ per pixel. The plate scale is similar to Siding Spring's seeing when the effects of the Uppsala's optics and its dome seeing are taken into account: AAT logs over 2000-05 show 64% of nights are usable, with sub-1.75″ seeing 68% of the time (Keller et al. 2007).

The Catalina pipeline detects comets and supernovae as well as asteroids, but both its temporal spacing of observations (cadence) and its implementation are not structured to detect TNOs. Main-belt asteroids have apparent motion of 30-40 ″/hr, while the slowest

[1] NASA Near-Earth Asteroid Discovery Statistics.

[2] Comet discoveries from E12: "McNaught": 75, "Garradd": 17, "Siding Spring": 10, "Christiansen": 1 (shared naming rights reduce the total).

[3] Voluntarily made available by the surveys for their mutual coordination at the Minor Planet Center.

[4] The images are 4096 x 4110 pixels, ie. 7372.8″ x 7398.0″.

moving Siding Spring detections to date are $\sim 15'/\mathrm{hr}$,[5] the speed of a fast-moving Centaur, which leaves them unable to detect the slower motion of TNOs.

In the standard cadence, four unfiltered integrations of between 20 seconds and 1 minute are taken of each field, at spacings of 10-12 minutes. This gives a span between first and last image that is normally about 45 minutes. Most integrations are either 20 or 30 seconds long (Fig. 3.1). As this figure shows, the integration time does vary throughout the dataset: it is increased by the observer in non-photometric conditions to maintain an approximate limiting magnitude of $m_{clear} \sim 19$. If any unknown moving objects are detected in the realtime processing of these observations, the observer will interrupt the scheduled cadence for between three and five followup observations which track on the new discovery. At this stage, the observer may designate a new field centre, or track on the moving object. Some 800 deg^2 of sky are observed per night.

The field identification codes are classified by their initial letters as follows, with the number of unique fields in that grouping:

- N: field north of celestial equator, regularly scheduled field: 4248
- S: field south of celestial equator, regularly scheduled field: 711
- U: user-defined followup field: 1617
- F: followup field (not functionally different from U): 579

There are 4959 regularly scheduled fields, which together cover 20,870.6 square degrees of sky; 51% of the total sphere of sky. The N and S fields have constant field centres. They are occasionally trailed when on the last image of the standard cadence of four images, the field hits a software elevation limit in the west and the tracking is switched off. This is rare, but as it occurs manually, it is not recorded in the header (R. McNaught, pers. comm.)

The U and F fields are centred on newly discovered moving objects, and are frequently trailed. Usually the exposure is set so the stars barely trail, few more than a seeing diameter (3 pixels) to retain astrometric accuracy; rarely, the stars are significantly trailed to go fainter to make an initial recovery detection or to increase the signal-to-noise for details in a comet's tail. This trailing is set manually on the telescope control computer, so it is not recorded in the image header (R. McNaught, pers. comm.).

The standard cadence is repeated on each field anywhere from the next night to several weeks to months later. In its observing from March 2004 to October 2009, the data considered here, the Survey took well over half a million images: 624,484. Images were recorded to DVD at the completion of each night's observing, producing an archive of more than 1700 DVDs, stored at the dome, which were the only copy of the survey data. Some 93% of the survey data were recoverable from these disks,[6] and were transferred to a striped RAID

[5] The Siding Spring Survey discovered the 18th magnitude Centaurs 2008 YB3 and 2012 DR30 when they had a $\sim 15''/\mathrm{hr}$ motion.

[6] The 624,484 are those that were successfully recovered.

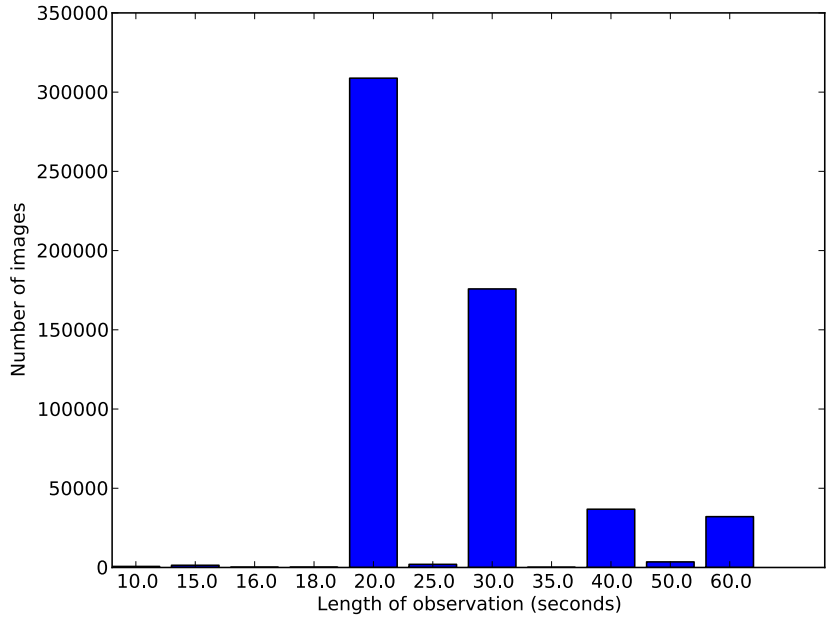

Figure 3.1 Integration times of individual images of all standard survey fields south of the ecliptic in the Siding Spring Survey dataset. The predominance of 20 and 30 second exposures give the survey an effective depth of about 19th magnitude; this is quantified in Chapter 4.

array at Mt Stromlo. These 6.5 TB of `.fits` images and their derived `SExtractor` (Bertin & Arnouts 1996) output files form the dataset for this analysis.[7]

The images are fully reduced, with flatfielding, debiasing and WCS fitting applied. Almost all of the images are compressed with the lossless settings of the Space Telescope Science Institute's image compression package `hcompress`,[8] which applies a two-dimensional Haar transform and reduces the file size to a quarter of the raw size. There are `gzip` compressed `SExtractor` 2.0 files for each image, produced with the standard Catalina pipeline `SExtractor` settings (Table 3.1).

Fortunately, the image compression leaves the headers in plain text. The images' metadata were therefore catalogued by extracting and storing the essential header information in a table of a Postgres SQL database.Queries to this database were then used to determine the revisitation cadence and the sky coverage of these years of observations.

[7]We greatly appreciate the assistance of Rob McNaught. As the survey's single copy was not to be removed from the dome, Rob copied the data from the 1700 DVDs to terabyte drives over the course of six weeks of observing runs, making this analysis possible.

[8]The images were given the non-standard suffix `.arch` or `.arch.H`

Table 3.1 Selected Catalina pipeline `SExtractor` settings.

Parameter	Setting	notes
DETECT_MINAREA	3.0	minimum number of pixels above threshold
DETECT_THRESH	1.2	sigmas
ANALYSIS_THRESH	1.5	sigmas
FILTER	Y	apply filter for detection
FILTER_NAME	gauss_1.5_3*x*3.conv	
DEBLEND_NTHRESH	64	Number of deblending sub-thresholds
DEBLEND_MINCONT	0.0	Minimum contrast parameter for deblending
CLEAN	Y	Clean spurious detections
CLEAN_PARAM	1.0	Cleaning efficiency
MASK_TYPE	CORRECT	type of detection MASKing
PHOT_APERTURES	5	aperture diameter(s) in pixels
PHOT_AUTOPARAMS	3.5, 4.5	Kron fact, min radius
SATUR_LEVEL	32000.0	level (in ADUs) at which arises saturation
MAG_ZEROPOINT	25.74	magnitude zero-point*
GAIN	1.1	detector gain in electrons per ADU
PIXEL_SCALE	1.8	size of pixel in arcsec
SEEING_FWHM	4.0	stellar FWHM in arcsec
BACK_SIZE	32	Background mesh: size
BACK_FILTERSIZE	3	Background filter: size

* Catalina chose this zero-point as it should yield Johnson V magnitudes to an accuracy of +/- 0.1 magnitudes. This value assumes a source (B-R)=0.7, a nominal value for asteroids, and (V-R)=0.5.

3.2. Observational characteristics of the survey

Surveys for trans-Neptunian objects are typically observed with dedicated time on a survey telescope, with full control over their cadence of observation and the time of observation of their field relative to opposition. As this is an archival survey, we have neither. There are therefore two considerations in assessing if this data can be adequate for detecting TNOs.

The first is the revisitation rate of each field: are there enough data to link appearances of a TNO on multiple nights on the same field into a recognisable orbital arc. The second is the elongation of each field: are the fields observed close to opposition, maximising the motion rate of any TNOs in that field due to the reflex motion of the Earth.

We chose to use only the regular (N and S) Uppsala fields in the initial analysis, as their constant field centres maximise the area that is covered by repeated observation. The irregular images observed with non-sidereal tracking could be checked later to add extra astrometry, if an object was found on a regular field. Consideration of the field selection therefore refers only to the regular fields. This gave us 568,751 images to consider.

3.2.1. Cadence and sky coverage

As discussed in § 1.3, three observations are the minimum needed to fit an orbit, and previous surveys that are sensitive to Kuiper belt objects have typically had their three observations on the same night, spaced by an hour or so, cf. the 1″/hr motion rate sensitivity of Trujillo

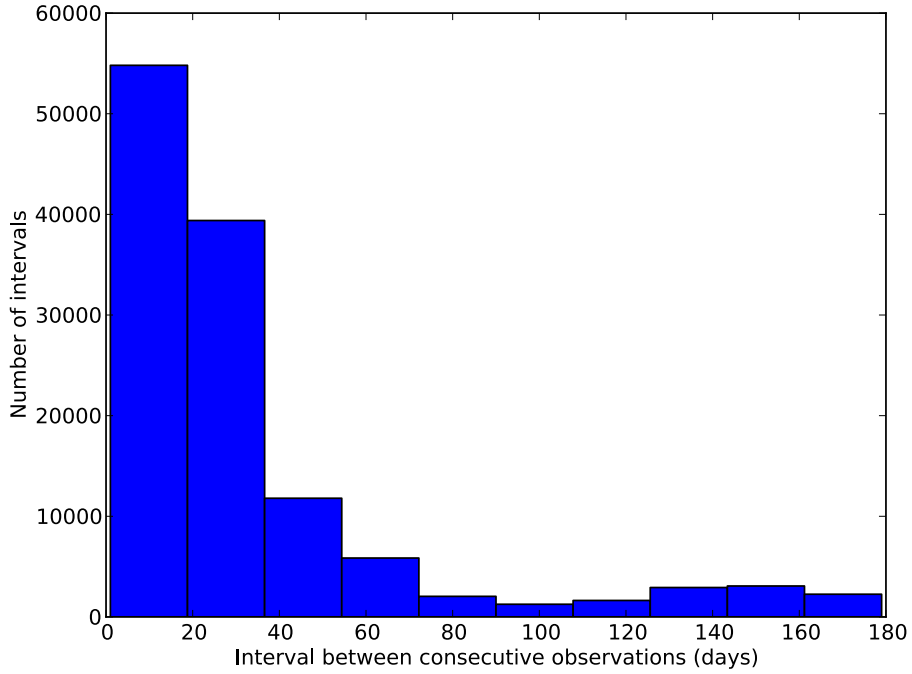

Figure 3.2 Frequency of the length of the separation between all the consecutive observations of the 4959 regular (N and S) fields. 95% of the separations are less than 180 days; note that most are revisited well within a month.

& Brown (2003). Modifying this to two observations on the same night, spaced by four hours or so, followed by another observation within a few days, allows detection of objects at Sedna's ~ 100 AU distance, cf. the 0.2″/hr motion rate sensitivity of Schwamb et al. (2009). A follow-up observation to secure orbits is made a month or so later. Since TNO detection relies on linking triplets of observations into orbital arcs, as the cadence length increases, the number of triplets to be calculated increases as n^2 permutations (Becker et al. 2008).

Examining the cadence of observation of the regular Uppsala fields shows that most are observed at spacings of between a few days and several weeks (Fig. 3.2), and this pattern is consistent in individual fields, e.g. the field shown in Fig. 3.3. These gaps are considerably larger than the surveys cited above: even a week-long gap is considerably larger than a normal survey's emphasis on revisiting its fields in a single night.

However, this extended cadence is a benefit rather than a problem, as the longer the temporal arc of the points that are used to calculate the orbit, the more certain the solution to the orbital parameters become. This gives the Uppsala TNO survey a great asset: any detections in the data will immediately have well-secured orbits.

This dense temporal sampling of objects on the same fields also offers the possibility of producing initial crude lightcurves, or at least a check for magnitude fluctuations on the scale of that of Haumea, 0.25 mag (Rabinowitz et al. 2006), for any detections.

Extending this examination of the temporal sampling to the whole data set, the overall coverage of the Uppsala survey is exceptional (Fig. 3.4). For example, 2,257 of the regular fields have 30 or more[9] nights of observation in the five years through to October 2009, giving 9,498.9 degrees^2 of highly sampled sky coverage (Fig. 3.5), 23% of the total sphere

[9]This choice of value discussed further in § 3.2.2.

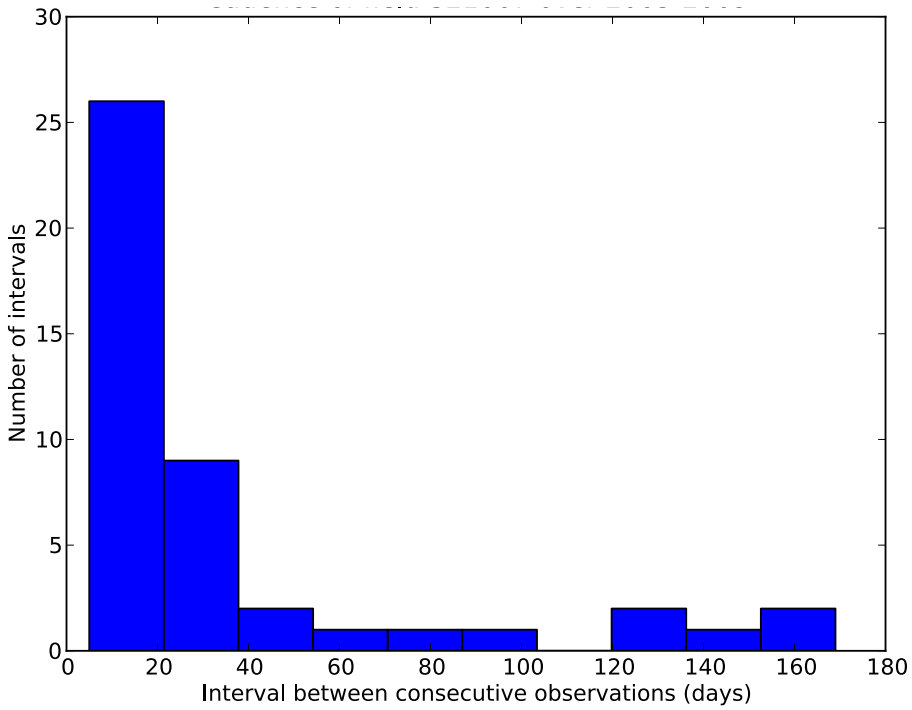

Figure 3.3 Frequency of the length of the separation between all the consecutive observations of an example field (S21067: 09:30, -21:11) with 46 observations in 2004-2009.

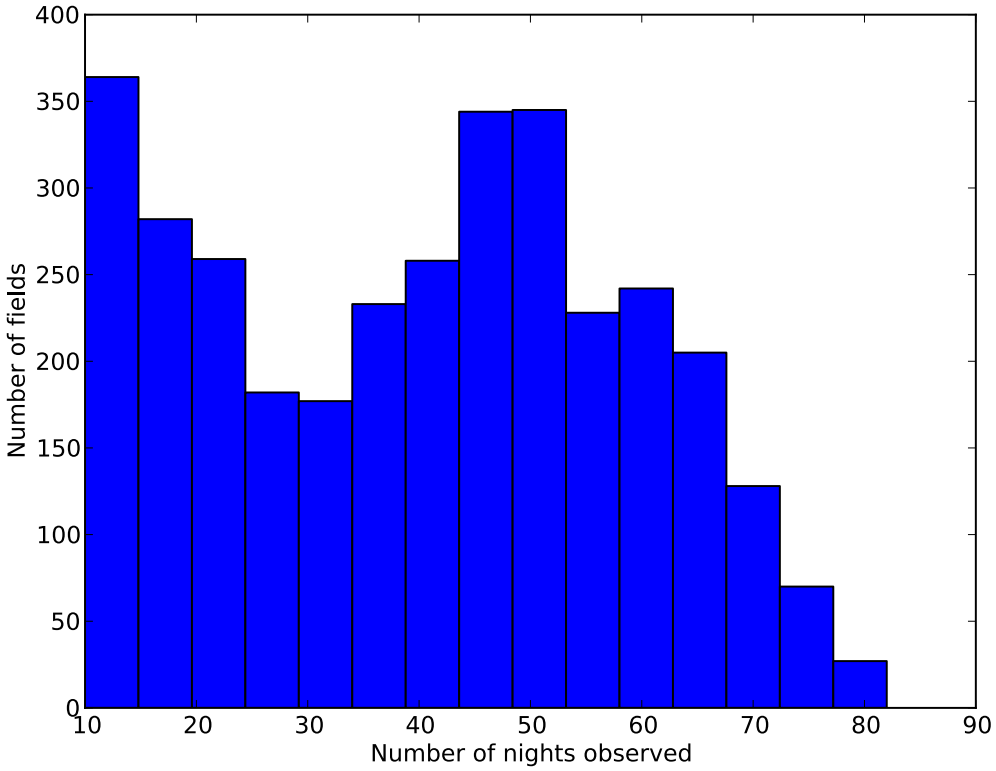

Figure 3.4 Density of temporal observation of the 4.5 deg^2 Uppsala fields. Most fields have more than 30 nights of observation over the five years of data we consider.

of the sky. Considering the sky coverage as a function of depth in magnitude with that of previous surveys, our survey, while shallow - we did not anticipate going any deeper than magnitude 19.5, given the short exposures and small aperture - had an exceptional sky coverage.

Prominent in Fig. 3.5 is the $b\pm \sim 15^\circ$ zone of galactic avoidance: this was dictated in the survey scheduling due to the high star density of the area, which would cause moving objects to fall on top of stars too frequently to be easily recovered. This 7200 deg^2 area $\sim -10 \leq b \leq \sim 10$ has generally been avoided by moving-object surveys that do not use an image subtraction data reduction technique (Fig. 1.3). Taking the Uppsala coverage to begin in earnest at $\delta = -15^\circ$ and the Uppsala galactic avoidance area of $-15 \leq b \leq 15$, placing 140° of galactic longitude within the Uppsala field of view, the area of southern sky avoided by our survey due to the Galaxy comprises 4200 deg^2. This is a substantial unsurveyed bite out of the total potential sky area that could be surveyed by a telescope located at Siding Spring, but it cannot be addressed by this survey[10].

Two calculations are essential to the smooth running of a survey: being able to project the orbits of newly discovered objects into the past and hopefully find earlier detections in this or other data that can help improve the orbit, and correctly identifying known discoveries that move across the fields. We developed a small pipeline querying JPL Horizons for precise position information for known minor planets over the five years of the Uppsala survey dataset. These positions were then matched to the observations made by Uppsala on these fields, as in our survey simulator (§ 4.3).

There are few known trans-Neptunian objects that could have been potentially recovered by this survey. If we examine the $H < 6$ TNOs known as of September 2013[11], and then restrict this subset further to those objects that are both south of the celestial equator and have a magnitude < 20 during the survey duration, we find that only nine objects are present (indicated by red crosses in Fig. 3.5). (134340) Pluto, at magnitude 14.3 the only sufficiently southern TNO bright enough to definitely be within the survey magnitude range, is unfortunately within the unobserved sky of the galactic avoidance zone for the duration of the survey (in Fig. 3.5, it falls in solid black unobserved sky). Six of the subset did fall on the survey N and S fields: 47171, 90482, 2010 EK$_{139}$, 90568 (formerly 2004 GV9), (28978) Ixion, and (50000) Quaoar. Of these, three objects fell on the 30+-epoch fields (on the white area in Fig. 3.5): the plutino (28978) Ixion, $m_V = 19.44 - 19.9$ (DES); the Centaur 2010 EK$_{139}$, at $m_r = 19.9 - 20.2$; and the classical KBO 90568, at $m = 19.0 - 20.0$[12]. They provide some spread between 19th and 20th magnitude available to test the magnitude limit of the survey and its detection efficiency in the lower part of the efficiency curve.

As detailed in Chapter 2, the newly discovered TNO 2012 DR$_{30}$ was first found by the Siding Spring Survey on very northern Uppsala fields. Though tracking steadily south since its discovery in February 2012, it was too far north to fall on the main fields with 30+ epochs that we used in the Uppsala TNO survey during the survey's span.

[10] Part of this sky has been subsequently addressed by Sheppard et al. (2011).

[11] According to the Minor Planet Center Distant Objects

[12] Magnitudes via the MPC; associated caveats regarding the quality of reported photometry and its associated uncertainties apply.

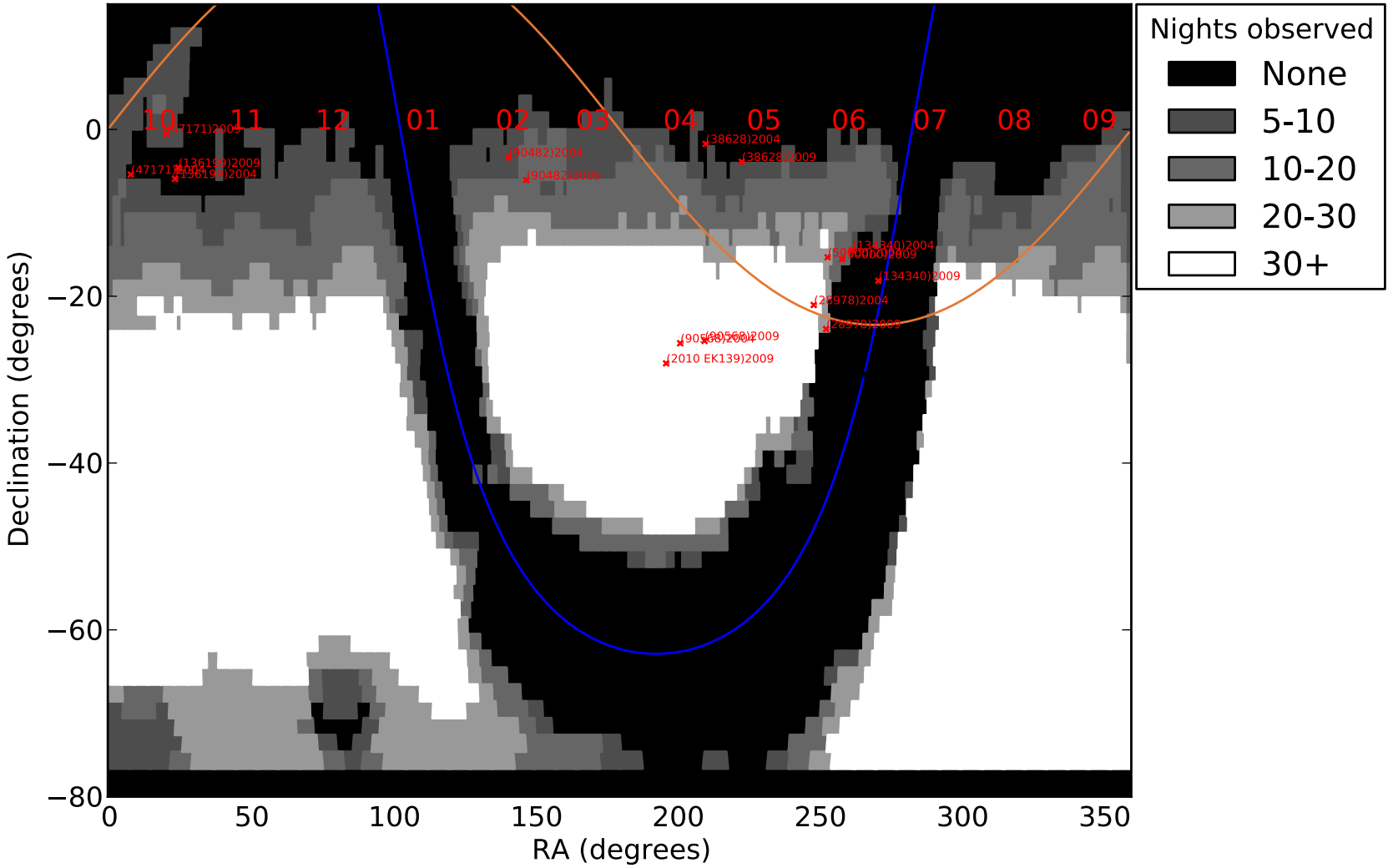

Figure 3.5 The sky coverage of the regularly scheduled fields of the Uppsala survey, 2004-2009. The brightness of a field, dark grey to white, indicates its number of observations; black indicates no observations, and the darkest shade of grey indicates at minimum 5 observations. Other shades increment up to white, which indicates fields with more than 30 observations. The ecliptic is in orange, the Galactic plane in blue in the prominent curve of the avoidance zone (solid black). The month 1-12 at which that area of sky will be at opposition is indicated across the top. $H < 6$ TNOs with $\delta < 0$ and $m < 20$ are indicated by red crosses, with positions labelled those at each end of the survey timeframe to show typical KBO motion over the span of the survey. They are labelled with their MPC designations.

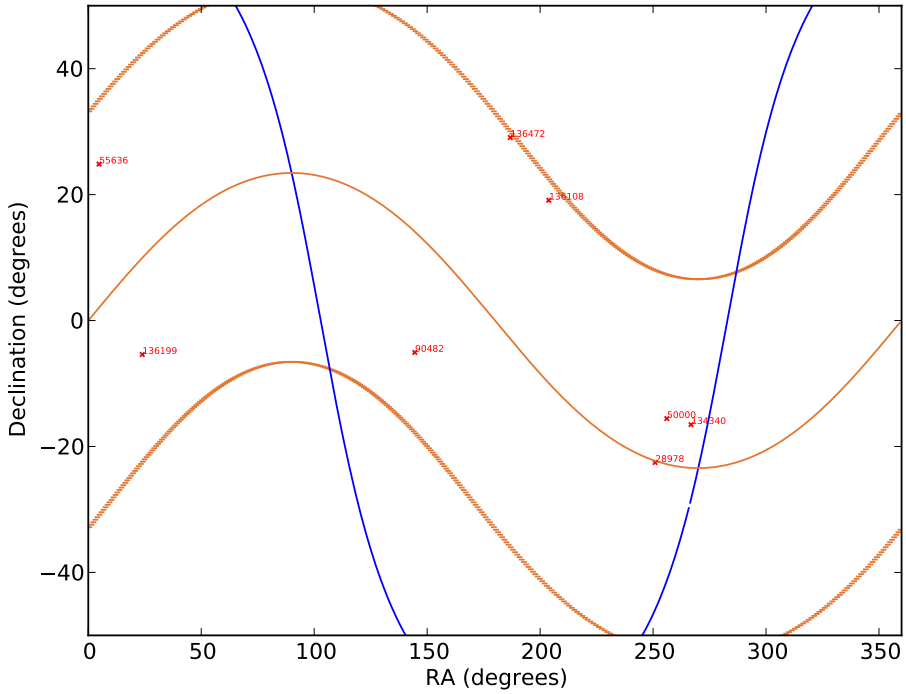

Figure 3.6 The positions of the eight $H < 4$ TNOs that are $m < 20$, on the midpoint of the Uppsala survey on 1 January 2007. In order of increasing right ascension, they are: 55636 aka 2002 TX_{300}, (136199) Eris, (90482) Orcus, (136472) Makemake, (136108) Haumea, (28978) Ixion, (50000) Quaoar, and (134340) Pluto. The declination range is restricted to that where the TNOs fall; the ecliptic is the thin orange line, the ±30° ecliptic latitude lines are heavier orange lines, and the galactic plane is in blue.

The global distribution of $H < 4$ TNOs shown in Fig. 3.6 emphasises that bright TNOs are found within ±30° of the ecliptic. The telescopes in the North that are known for TNO surveys (Table 1.2) were primarily at the sites of Mauna Kea 19.8° N, Kitt Peak 32.0° N, Palomar 33.4° N, and could therefore see south on the sky to δ -26.6 – -40.2 when observing at an airmass of 2. At altitudes below airmass 2, the degradation in depth of observations would make it impractical to continue to survey. Taking Schwamb et al. (2010)) as it has the greatest sky coverage, the big Northern surveys had a cutoff of $\delta = -30°$ and were complete northwards of that, cf. Fig. 1.3. This means that surveys in the North have scanned 91% of the 21,600 deg^2 of sky that is ±30° of the ecliptic, with 2400 deg^2 of unsurveyed sky remaining in its southernmost part.

The Uppsala survey's sky coverage is well placed to address this unsurveyed sky - except that it is cut through by the avoidance zone of $b\pm \sim 15°$ around the Galactic plane, removing $\sim$ 890 deg^2 of sky with high stellar density from the area of sky that was both within 30° of the ecliptic and north of $\delta = -30°$. With this reduction, the area of sky unique to this survey that was within the region ±30° the ecliptic, given the calculation above, was 1510 deg^2, 7% of the area within ±30° of the ecliptic.[13] This was a modest area of sky given the sky density of bright TNOs seen in Fig. 3.6: momentarily setting aside the deeper complexities of perihelion bias and population structure, eight objects at $m < 20$ in 21,600 deg^2 of sky implied a $\sim$ 50% chance of discovery of a new bright classical KBO in this patch.

[13]Much of this galactic avoidance area and surrounding sky was subsequently surveyed by Sheppard et al. (2011) and Rabinowitz et al. (2012), although the processing of our dataset was complete before these entered the literature.

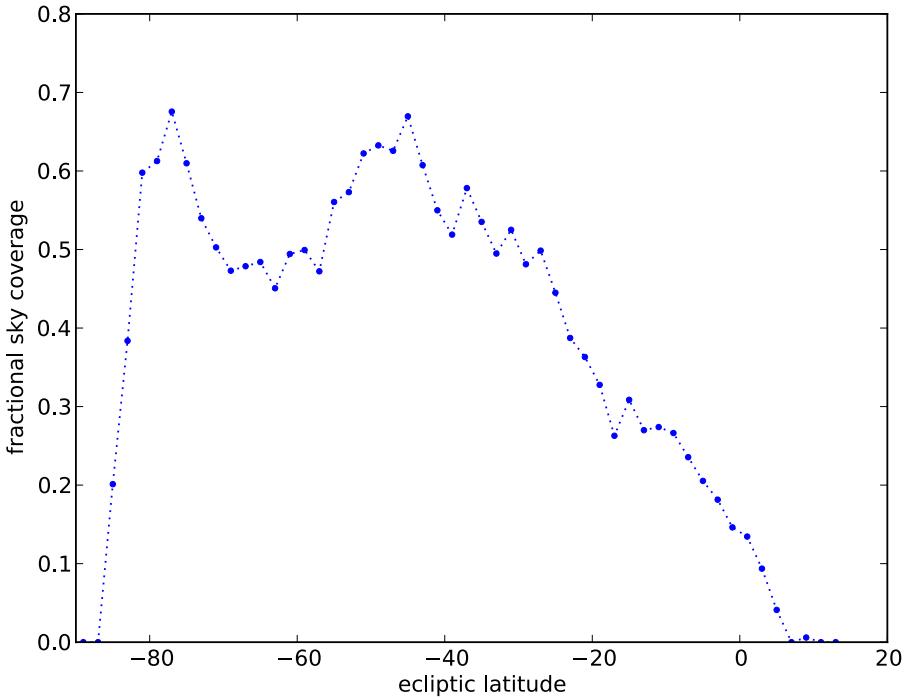

Figure 3.7 The sky coverage of the fully processed Uppsala survey fields as a function of ecliptic latitude, considered in 2° bins. This shows how strongly off-ecliptic a survey this work is compared to previous surveys; cf. Fig. 4 of Schwamb et al. (2010) and Fig. 7 of Rabinowitz et al. (2012). The influence of the Uppsala survey's avoidance of the Galactic plane region creates a prominent dip.

Most of the Uppsala survey sky coverage was far from the ecliptic, within the higher ecliptic latitudes −30 – −80° (Fig. 3.7); this lowered the density of TNOs falling on the majority of the survey fields. If (136199) Eris's inclination of 43.9° is momentarily considered as typical of scattered disk objects, such that most of its orbit will be spent at ecliptic latitudes ~ 40°, the sky at high ecliptic latitudes is where such objects would be found if sufficiently bright. Previous surveys surveying $\delta < -30°$ (Table 1.2 and Fig. 1.3) have scanned some 1970 deg^2 of sky at ecliptic latitudes > 30° (including the Galactic plane since previous surveys often have not reported the shape of the edge of their sky coverage exactly adjacent to their cutoff to the Galactic plane), one-fifth of the high-inclination population sky[14].

The Uppsala survey area went down to $\delta \sim 80$ (Fig. 3.5), sky which includes the southern ecliptic pole. Not surveyed within that part of its coverage at > 30° ecliptic were the ~ 376 deg^2 of sky at the celestial pole, due to the restriction of the Uppsala's equatorial mount, and the 3000 deg^2 of sky from the Galactic plane avoidance $b\pm \sim 15°$ that placed 100° of galactic longitude within the > 30° ecliptic part of the survey area. This survey therefore had available 7248 deg^2 of sky (70% of the sky at > 30° ecliptic), unchecked by any prior survey, to add to the census of the bright end of the scattered disk population. Given the very low sky density of such bright scattered disk objects, Eris being the only true SDO in the sample of eight indicated in in Fig. 3.6, there was probably also only an even chance of detecting a new bright SDO in this surveyed sky.

[14]Note though that Eris was not discovered in that area of sky but closer to the ecliptic.

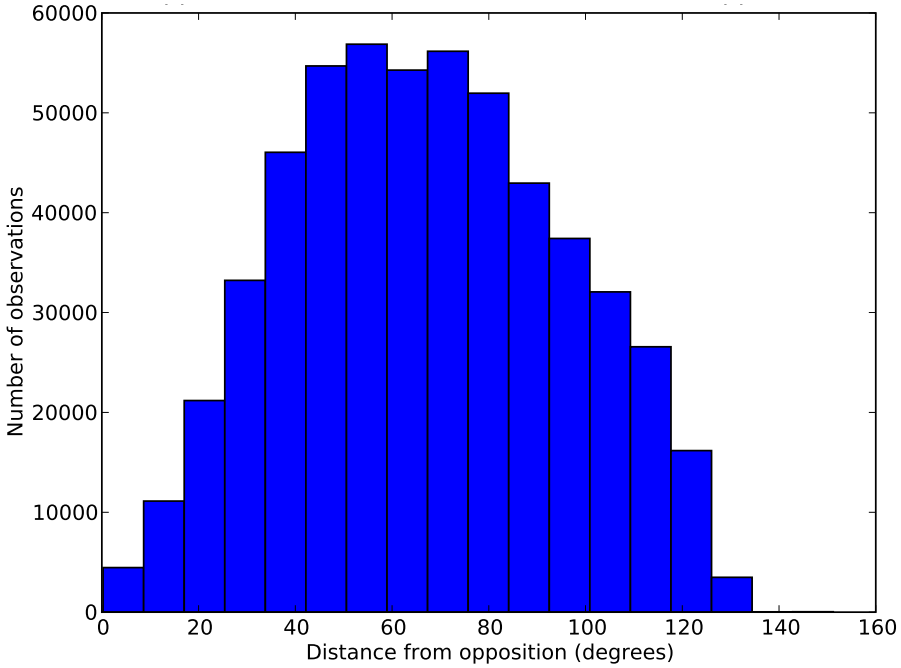

Figure 3.8 The distance from opposition of all the observations in the entire Uppsala dataset south of the ecliptic. The fields are observed at a wide range of angles from opposition, unlike a normal TNO survey that centres the fields on opposition to maximise the TNO motion rates. The dip close to opposition itself is expected in any survey, due to the small area of sky that opposition itself occupies. The highly southern sky coverage of our survey also puts its fields far from where opposition moves along the ecliptic.

3.2.2. Distance from opposition

A purpose-designed TNO survey keeps its observations within a few tens of degrees of opposition: for example, within 1.5 hours for Trujillo & Brown (2003), and 42° for Schwamb et al. (2009). As discussed earlier in § 1.3.2, this maximises the motion rate of TNOs.

However, applying a similarly strict cut to the Uppsala dataset would leave too few observations to create a highly sampled TNO survey. The elongation of the fields varied considerably (Fig. 3.8), including observations made at up to and beyond quadrature. Most fields have six to ten observations made in the 180 days (six months) centred on the time of the year that the field is at opposition, as in Fig. 3.9. Six to ten observations should allow construction of two or three orbital triplets, so the 30+ epoch fields (30 nights / 5 years ~ 6) provided sufficiently abundant data to construct intra-season arcs for potential TNOs.

We used all the data for the Uppsala fields that have 30 or more nights of observation in our analysis, choosing a six month "opposition season" as a compromise between maximising the number of observations that will initially be considered together for an arc linkage and constraining the distance that the field will be observed from its opposition. This gave us 464,703 images to consider.

As there are sufficient observations available in each season, it is possible to take the simplest approach to analysing the data for moving objects: considering in turn each season of each field.

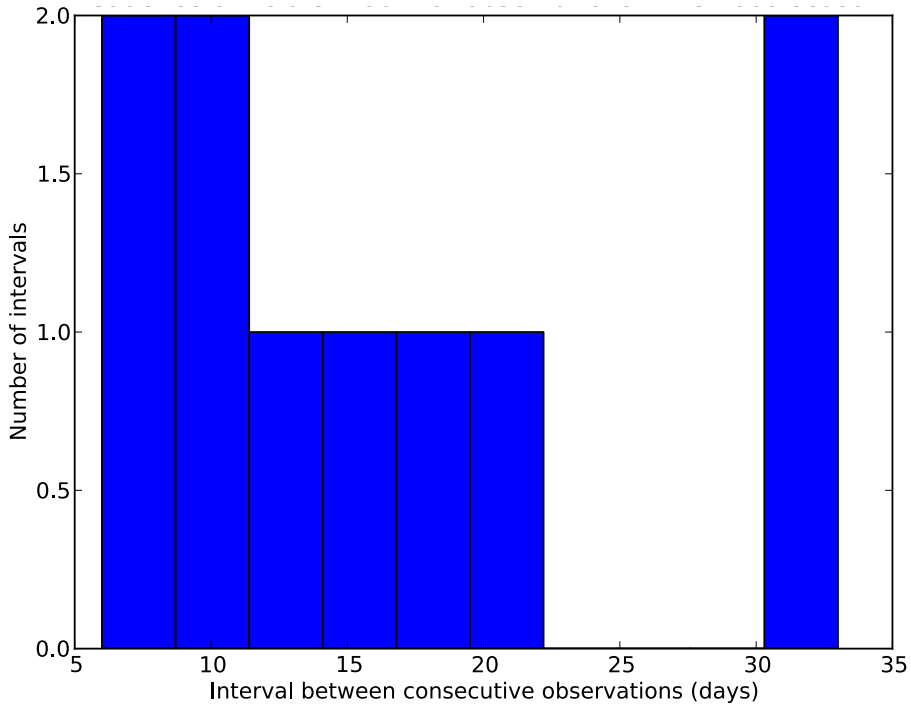

Figure 3.9 Frequency of the length of separation between the consecutive observations (46 in total) of an example field (S21067: 09:30, -21:11) made in the six months centred on its date of opposition, a period for each field that we define as its "season".

3.3. The analysis pipeline for TNOs

Having determined that the data are sufficiently highly temporally sampled and otherwise appropriate to be used as a TNO survey, we proceed to the conceptual design of the re-analysis of the data for TNOs. This is similar in principle to the traditional method of TNO surveys. A list of point sources is extracted, the points corresponding to moving objects are identified, and all plausible orbits between sets of three points (the minimum required to determine an orbit) are calculated.

Alternatively, the images of each field could be stacked and image subtracted, which will remove the stars and leave the moving objects as streaks. In this analysis, we follow the first method.

In this section, we go through the order of design and operation of the modules of the Python-based Uppsala TNO pipeline. This pipeline was run on a 32-processor machine.

§ 3.3.1 Make the master list of photometric sources for a given field, with sources grouped by night

§ 3.3.2 Group the sources across nights to allow division between stars and astronomical transients

§ 3.3.3 Find triplets of transients spaced across one opposition season that fit the orbital parameters of TNOs

§ 3.3.5 Join the surviving triplets together across the years and see if the resulting arcs still form valid TNO orbits

§ 3.3.7 Examine the transients that make up the valid arcs to confirm that all are true astronomical transients

3.3.1. Extracting and merging sources

The first part of the detection of moving objects was to find all of the astronomical sources in the survey images. The list of sources in each of the 464,703 images already existed: the Catalina `SExtractor` files were created with settings optimised for detecting asteroids (Table 3.1), so we began processing these files rather than running `SExtractor` from scratch. Catalina did use a generous 1.2σ detection threshold for a source, which would produce many more detections, most of which would be due to background noise. However, pushing that far into the noise was ideal for pushing the survey magnitude limit for TNO detection, especially as the survey has a bright magnitude limit of $m_{clear} = 13$.

`SExtractor` provided output that varied slightly across the years. The most notable difference was that part way through the survey, the RA switched from being formatted in hours to in decimal degrees. These more than four hundred and sixty thousand source files had to be cross-correlated to determine which were true astronomical sources and which were instead spurious noise, and each unique source needed tagging and tracking throughout processing. The sources therefore needed metadata.

We tested implementing the metadata via a table in our SQL database; the overhead was prohibitive for the disk space that we had available. We instead processed each source detection into instances of a purpose-built Python class, `kupeclasses.Source`. From these, we assembled a reference catalogue for each night on each field out of the sources from each image, populating a set of sources with appropriate metadata. The intranight temporal spacing of ~45 minutes from first to last observation is very short for a TNO survey: too short to leave the sky motion of a trans-Neptunian object visible. A KBO will move ~ 2.3 arcsec in this time, which at the plate scale of 1.8 arcsec per pixel creates a shift of 1.25 pixels. The median seeing at Siding Spring is 1.5-2 arcsec (Keller et al. 2007), not accounting for the dome or telescope-tube seeing. This shift was therefore too small to use for initial detection of TNOs.

However, at this point the wealth of temporal sampling of the dataset could be brought into play. It was perfectly possible to instead combine the sources that are roughly together over the span of the *intranight* cadence into single sources, and construct only *internight* triplets of sources in potential TNO orbits. This also conveniently culled out all cosmic rays and most fast-moving asteroids far from their stationary points, along with a fair amount of the noise. We could instead take advantage of the tiny intranight on-sky shift of a TNO under Siding Spring seeing, which remained too small for the merging to cause the loss of such slow-moving objects. An initial cutoff distance of a few arcseconds was therefore quite adequate to "smudge" the moving object into being correctly identified as the same candidate.

Using only this internight orbit fitting did introduce an inherent inner cutoff in heliocentric distance to the survey. We cannot detect any object that moves faster than about the 15 "/hr

perihelion speed of a Centaur, and have correspondingly poor sensitivity to Centaurs. This is quite intentional: as mentioned earlier, the slowest-moving object that can be detected with the standard Catalina pipeline is a fast-moving Centaur. The exact inner heliocentric distance limit then changed from night to night and field to field; this is accounted for in later calculations of the phase space sampled by the survey.

We therefore next created a merged set of `Sources` for each night on each field. The longest of the four `Source` lists from each image was taken as the master for comparison. Each source in that list then had the other lists checked against it to find if there was a corresponding close-by source. This was speeded by sorting the lists by RA and using a bisection algorithm to quickly find the sources that were within a surrounding box 10 arcsec on a side, then calculating the true arc distance of the sources within the box. The closest source to that on the "master" list was kept; in addition, it had to be within 6 arcsec to be kept. The sources that had corresponding twins on all of the images from that night were kept as "candidates".

Because the seeing on a given night would change the dispersion of the location of each source, the cutoff distance to determine if a given source-cluster was the same source, seen over four images, could not be set at a constant value. We constructed a cumulative frequency plot of the dispersion of the clusters to determine the dispersal caused by seeing (Fig 3.10). We then applied a cutoff at the 5σ level and used that as the maximum dispersion allowed for each cluster for the night. The position of a source was then kept as the geometric centre of the cluster.

For each such cluster, a new `Source` was instantiated with the RA and declination of the geometric centre of the four-image cluster, and the median magnitude of the cluster. The `parent` field of the `Source`, which would normally hold the `Sources` that went into making this new `Source`, were not stored in the new `Sources` to minimise memory use. This produced a .dat file for each night of each field, containing a list of `Sources`.

3.3.2. Identifying transients

Given the lists of true astronomical sources from each night, the next step was identifying the sources in each image that were "transients": sources that were not stars. We wanted to retain the transients that were the point-source appearance of a TNO in the image.

Undesired transients that could contaminate our clean list of TNO transients include cosmic rays (high-energy particles from elsewhere in the Galaxy), dead or hot pixels (pixels in the detector that are no longer sensitive to incident light), asteroids at their stationary points (removed in later filtering), optical artefacts/image ghosting from scattered light in the system, which occurred frequently but was often pointing-dependent, contaminants such as dust particles on the telescope optics, and extra detections above the noise generated by the halo surrounding saturated stars.

While the transient detection is efficient at removing cosmic rays, in retrospect it would have been useful to also filter out transients that are artefacts: bloomed pixels in halos around saturated stars (eg. Fig 3.11). This could have been done by removing those that coincided with the location of stars brighter than a certain magnitude, cf. Polishook et al. (2012) discarding transients near those stars brighter than 11th magnitude, in the Tycho-2

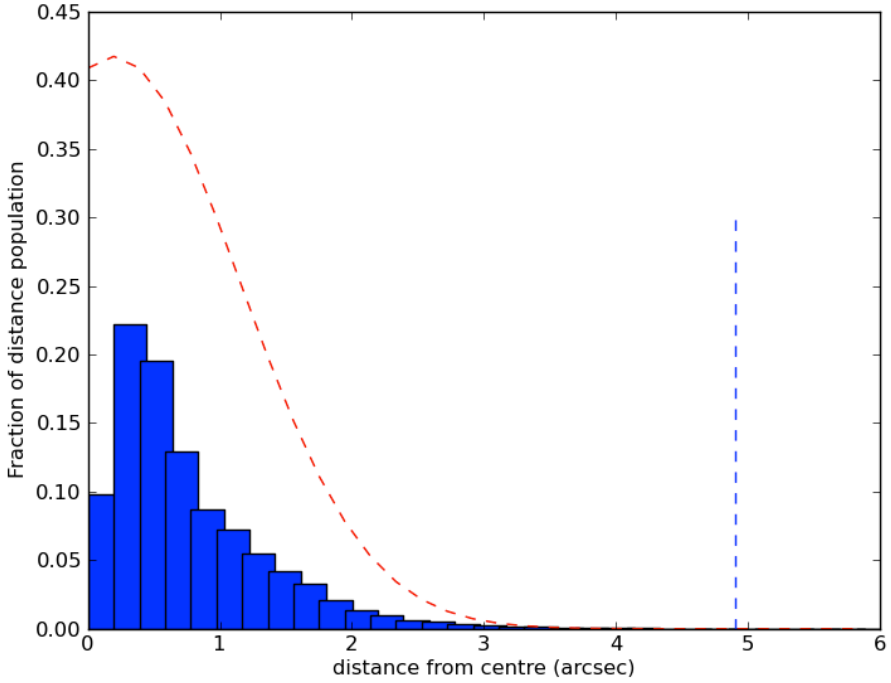

Figure 3.10 The cutoff limit for combining the four sources observed on a given field in a night into one centred source is set dynamically by the seeing on each night of observation. Here on Uppsala field S17078 (10:49, -17:10), the 95^{th} percentile limit cutoff (vertical dashed blue line) on the source dispersion (red dashed line) clearly excludes no true groups.

catalogue, when trying to detect asteroids in Palomar Transient Factory data. This would however potentially have decreased our efficiency of detection in the vicinity of the galactic plane.

Stars appear in the same location across all nights. The previous step had removed cosmic rays, hot pixels and some asteroids; this step removed most of the optical artefacts. Defining if a given source was the same source across all nights is computationally intensive: it is of $O(n^n)$ to match these lists of sources from each night across all the nights that each field had been observed. This was improved by careful implementation.

We matched the lists of `Sources` between nights with the same methodology as in the previous section. This matching differed in that the seeing conditions would have a much wider variation, so a uniform cutoff of 4" was imposed rather than a dynamic cut. If a given source-cluster appeared on only one night, it was considered a transient. Matched candidate lists and transient lists were produced for each night of each field, indexed by their night of appearance.

We then applied an internal photometric calibration to the transients of each field. We defined reference stars as those on each field that appeared on all of the nights that that field had been observed. This provided between 9,784 and 120,714 reference stars for each field. We calculated the night-by-night fluctuation of the suite of reference stars from their 30+ observation median magnitudes, and corrected the magnitudes of the transients in each night by corresponding variation. As the field is the unit of processing, the photometry remained internally consistent. These photometrically calibrated transients were used in the next step of processing: beginning to calculate orbits.

As visible in Fig. 3.12, the transients often cluster toward the edge of the fields. This is due

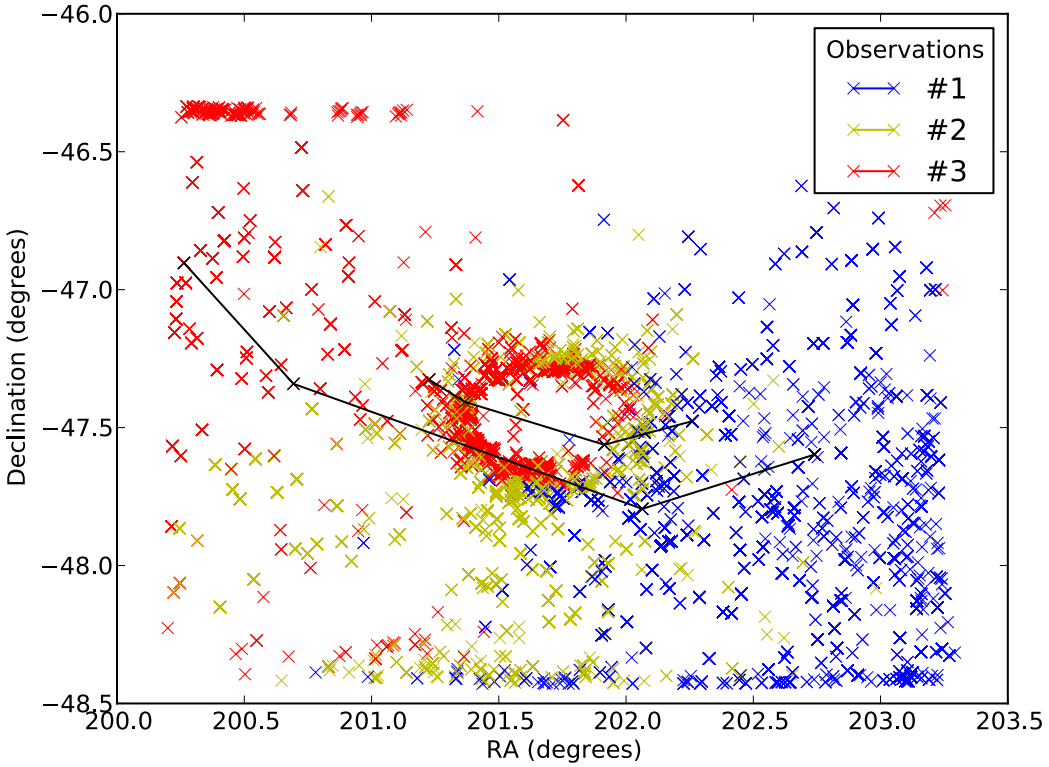

Figure 3.11 The transients on the Uppsala field S47070 (13:27, -47:20) show in a worst-case example that transients are produced in erroneous abundance around saturated stars. The colour-coding red through blue indicates the order of points within the triplets they formed; the points connected by black lines formed a valid longer arc.

to the slight variation in pointing between each image (and each night). We considered trimming transients from the edges of the fields to remove those created by these wobbles. This would certainly simplify the matching for triplets. However, it would also introduce intricate gaps in the field coverage, despite the fields' small overlaps in RA, and potentially drop real objects' observations. We left the transient lists intact.

We realised as a result of considering this, after all our processing was complete, that not all of the images had a correct world coordinate system (WCS). While the Uppsala field of view is large, and not particularly flat, with field distortions that are not consistent across the entire field, some 95% of the images have good WCS fits. There remain a small fraction of images that could not be fit with a WCS under any cajoling.

This significant problem meant that an extra step of processing was added to the production of matched sources across nights: we rejected those nights entirely from the transient lists.

3.3.3. Forming three-observation orbital arcs

Given the transients on a field, we wanted to identify all that belonged to the arcs of plausibly trans-Neptunian objects. The minimum number of points of observation needed to define an orbit is three: this allows the three spatial coordinates and the three rates of change of those

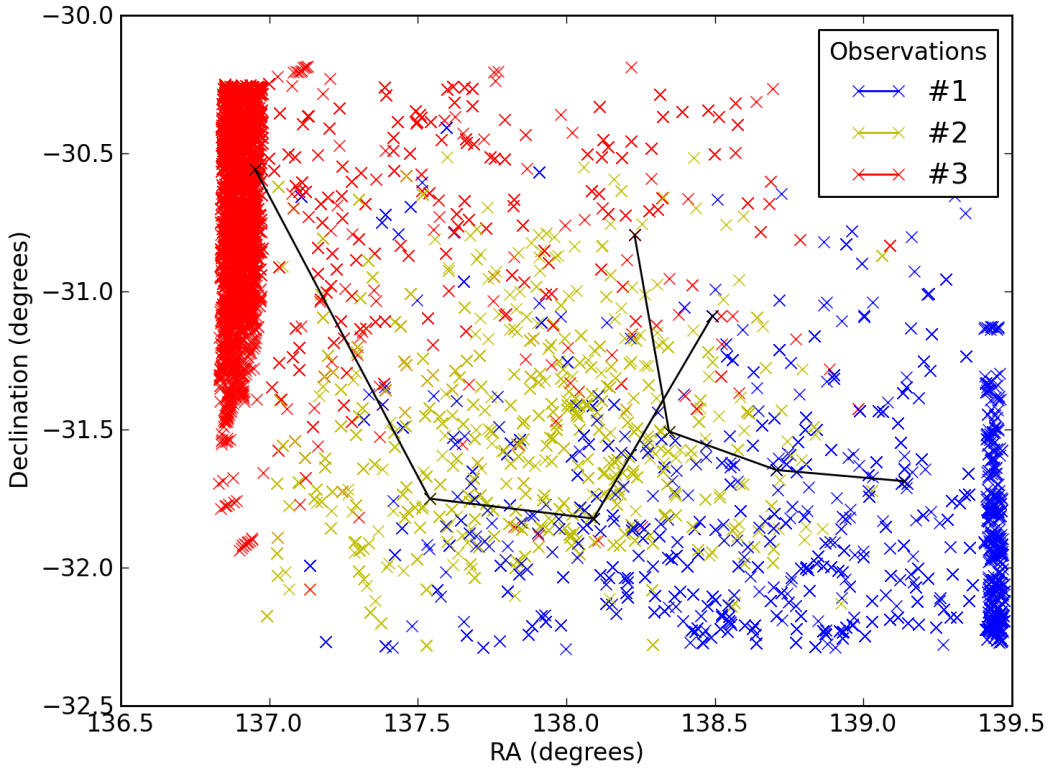

Figure 3.12 The transients extracted by stacking the nights of observation of the Uppsala field S31060 (09:12, -31:15) and removing those sources that remained within 4″ of the same location across all 30+ nights (stars). Transients cluster toward the edge of the field due to occasional nights where the telescope pointing varied. As in Fig. 3.11, the colour-coding red through blue indicates the order of points within the triplets they formed; the points connected by black lines formed a valid longer arc.

spatial coordinates to be found. Any three transients from different nights could potentially form the on-sky track of a TNO. Most triplets will not be linear, due to the Earth's motion. They will form a looping spiral on the sky: projecting a constant linear cone before and behind the midpoint observations of the triplet will therefore not minimise the number of matches that need to be tried. Our survey is unusual in that the cadence of the observations within the maximum span, which sets the maximum sky motion rate, is highly variable. The data may provide three observations spaced a day apart, or three at the span of the opposition season of 180 days, so the lengths on the sky of the triplets will also be highly varied.

Making these three-point orbital arcs leaves us with the computational challenge of calculating orbits for a permutation of the sets of transients on each night, on all of the more than two thousand standard fields where the nights number between 30 and 82 on each field. The permutation to be calculated per field is ${}^{nights}P_3$, where *nights* is the number of nights on the field, and 3 nights at a time are being checked for the formation of an orbit from their sets of transients.

Triplet constraints

However, this computational load could be reduced by filters. We applied the following straightforward spatial and temporal limits to the creation of these triplets:

Constant field The three transients were all sourced from the same field.

Chronological The three observations had to come one after each other.

Start-to-end span The observations occurred within the 180 days centred on the time of the year that their field is at opposition. This reduced the computational load in creating triplets, as opposed to trying to form and fit them across the whole survey.

This was pleasingly parsimonious. For example, if we consider one field that has forty nights of observations, each night with a list of transients, the number of sets of three nights that have to be used, where each set of nights tries its three transient lists together to form triplets, is ${}^{40}P_3 = 6 \times 10^4$ sets: this was reduced by our filters to 200 sets that had to be processed.

We also initially excluded very large combinations where all of the three nights in the set each had more than 600 transients, as they took upwards of several days to process.

Even after these initial constraints on triplet creation, we were left with a computationally extreme set of potential orbits to fit. To have the data processing completed in a reasonable time, we needed to reduce the enormous number of orbits to be fitted: on the order of a trillion. We therefore developed a least-squares orbit-fitting filter.

Keplerian filter

The most suitable trans-Neptunian orbit fitting algorithm is that of Bernstein & Khushalani (2000), which they implemented as the widely used C-based `orbfit` software: we used it as the heart of the Uppsala processing pipeline. Built with the assumptions that objects are distant, generally > 10 AU, and are observed moderately close to opposition (Bernstein & Khushalani 2000), the orbital fitting requires obtaining the parameter vector that defines a unique orbit, $\mathbf{a} = (a, e, i, \Omega, \omega, M)$.

The time-consuming part of running `orbfit` is its integration across large time spans. At its core, the main function of the software is a least-squares fit of a parabola to three points. The fit is easier to obtain by considering the coordinates in Cartesian space, but this still requires solving for a least-squares fit of the six parameters, such that the minimised χ^2 distribution testing the goodness of fit (per Eq. 15 in Bernstein & Khushalani (2000)) has six degrees of freedom. We implemented a version of these steps as a stand-alone processing script.

We first consider the coordinate system of the three observational points of the potential distant Solar System object. They are recorded in spherical coordinates, in the equatorial system, and have known times of observation. These observations form a projection onto the tangent plane, the plane of the sky (Fig. 3.13). In this flat plane, the Cartesian coordinate system is equally applicable: the orbit can still be specified in terms of a Cartesian x, y, and z. But being in Cartesian sky plane coordinates, it becomes easier to manipulate.

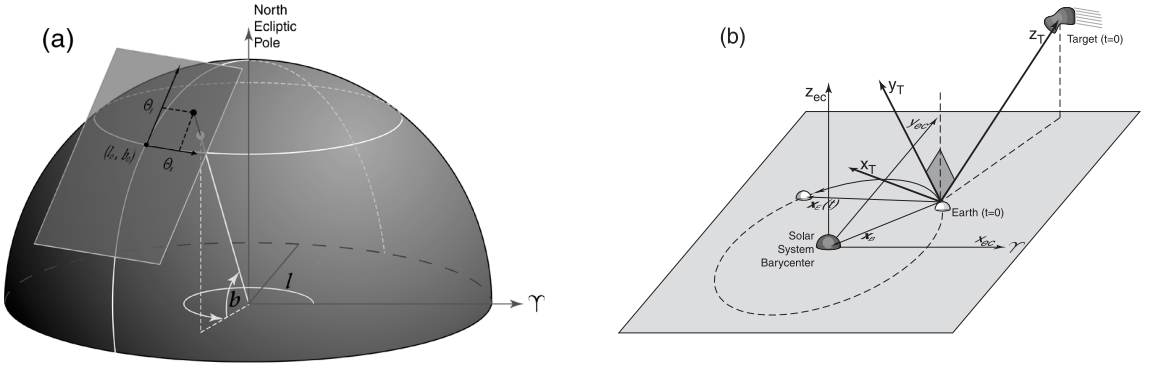

Figure 3.13 a) The spherical coordinates relate to a tangent-plane projection on the sky; tangent plane coordinates are projected about the initial line of sight to the target object; b) the geocentric, Cartesian (x, y, z) system to which the observations are transformed. This transformation from spherical (equatorial) coordinates via ecliptic coordinates to the Cartesian tangent-plane coordinate system allows the orbit to be least-squares fitted to the three points of observation. From Bernstein & Khushalani (2000).

We implement the filter as follows:

- Calculate the ecliptic coordinates of the Earth, the observing platform, on each of the three dates of observation.
- Calculate the ecliptic coordinates of the three observations (initially in equatorial coordinates).
- These produce two three-by-three matrices: of the Earth's position, and of the potential object.
- With the middle of the three observations as the temporal reference zero point:
- Transform all observations (Earth and potential object) to Cartesian tangent plane coordinates: α-vector = $(\alpha, \beta, \gamma, \dot{\alpha}, \dot{\beta}, \dot{\gamma})$, where $\gamma = 1/r_{helio}$
- Solve for $\gamma, \dot{\alpha}, \dot{\beta}$ using Cramer's rule, as these are the parameters that determine the parameter f: if the potential object is bound to the Sun.
- Calculate the residuals, which describe how well the orbit was fitted. We required the residuals to be less than 60″ for a reasonable fit.
- Conservatively retain triplets where $\gamma > 0$, and either $f < 3$ or ($\gamma < 0.020$, ie. r_{helio} more than 50 AU, and $f < 100.0$).
- Each observation in the triplet had to have $\delta mag < 3$ from their mutual median.[15]

We implemented this via index lookup of the transient `Sources` to conserve memory usage. The implementation also efficiently manipulates all the transients in each of the three nights

[15]We initially cut transients brighter than 0.5 mag of the shallowest night in the set, applied before the triplets were tested for orbits. This was seemingly too effective at removing triplets; probably it was also being applied erroneously, as the magnitude limits of the nights had not been properly calculated at that stage, and the cut was being made from the magnitude calibration applied to the transients. We changed it instead to a cut on magnitude after the Keplerian filter was applied.

being considered, least-squares fitting a large single matrix of possible triplets. We tested this carefully on single objects, scaling up from a single triplet of a known orbit to a set of several tens of triplets, then adding two and then three objects to ensure that the large single matrix was properly indexed.

Filters on fully fitted orbits

Applying the Keplerian filter left us with many fewer triplets: these were then fed to `orbfit` in batch mode for fitting for orbits in its normal manner, which makes a preliminary fit and then a full Marquandt-Levenberg fit. We considered these in million-triplet batches. Only twenty thousand were fed to `orbfit` at a time due to `orbfit`'s tendency to crash and require a restart on an input file on the occurrence of a variety of errors. We then filtered the fully fitted triplets further.

The easiest cut was to consider the size of the residuals of the fit to the orbit.

`orbfit` outputs the minimised χ^2 parameter from its goodness of fit of the orbit; a fit to a well-determined multi-opposition TNO will have a χ^2 very close to zero, and certainly less than ten. We confirmed this on fitting a range of known objects, which returned either $\chi^2 =$ 0 (an overfit) or 1 (an appropriate fit). 0.3″ generously estimates our astrometric error.

`orbfit`'s batch mode also outputs the orbital elements it found, except for inclination (which can only be obtained by fitting objects one at a time). We applied a cut on heliocentric distance, to retain some Centaurs and all TNOs,[16] while excluding asteroids, and on eccentricity to retain only bound (non-hyperbolic) objects:

$$\text{TRIPLET}_{kept} \begin{cases} r_{helio} & > & 15.0 \text{ AU} \\ a & > & 0.0 \\ e & < & 1.0 \\ \chi^2 & < & 100 \end{cases} \tag{3.1}$$

This still left a vast number of potential TNO candidates: the orbits of nearly nine million triplets passed all the requirements, too many to inspect the images of each by eye. The next step was to find if longer arcs of observation could be found, which could be more easily assessed as real TNOs.

3.3.4. The properties of triplets

We assessed the valid triplets produced by `find_planet` for any adverse characteristics (here referred to as "triplets" for brevity). The length of triplets were at least a seven-week span, and extended as long as eight months, though they peaked at 18-21 weeks (Fig. 3.14). Most triplets used the full spatial extent of the field as much as possible: most frequently, two observations would be spatially close together, and the third well further across the field, as in Fig. 3.17 and 3.12.

[16] As Tombaugh (1961) said, "[t]his nearer limit [of Saturn rather than of Neptune] was chosen because it entailed no extra work."

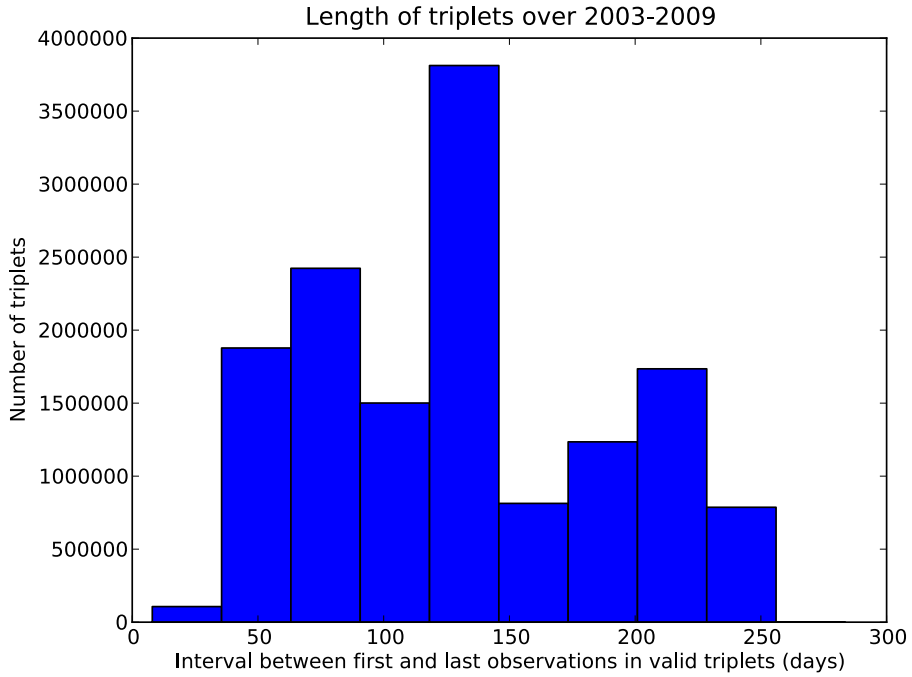

Figure 3.14 The temporal span of the valid three-observation orbital arcs that passed the filter conditions of Eq. 3.1.

3.3.5. Creating long orbital arcs

The dense temporal sampling of the Uppsala survey meant that any object appearing on a given field would reappear within the survey's five years in sufficient observations for it to be re-found in many more than one triplet (Fig. 3.15).

The smallest unit that we could link together to make a longer orbital detection arc would be two of the triplets that had passed the pipeline to this point. Intra-field linking was less computationally intensive as a first step: if its detection efficiency of TNOs was low, inter-field linking could be tried afterwards. We therefore linked all permutations of two of the "valid" triplets found on the same field into arcs, and refit and re-filtered the arcs, to see if any remained. Visual blinking could then be used to assess their validity.

Our thinking evolved in developing the arc creation filters. We first had to decide on the temporal length over which the arcs should be created. While we could have applied the single-season linking used for the triplets, there was no reason not to try linking over greater timespans: despite this requiring an n-to-n triplet matching, there were few enough triplets that it seemed plausible (once later filters were also applied).

We initially thought that the triplets to be linked should have at least one transient in common. The arc produced could then be up to five transients in length. However, this would limit the survey to creating arcs only in parts of the sky where the long opposition season would overlap year to year; arcs that would be only a little longer than a single opposition season. Large geometric areas of the sky would not meet this criteria; we did not implement it.

Finally, we added a filter for the similarity of the orbital elements of each pair of triplets. To be the same TNO, triplet orbits should have about the same orbital elements: the semimajor

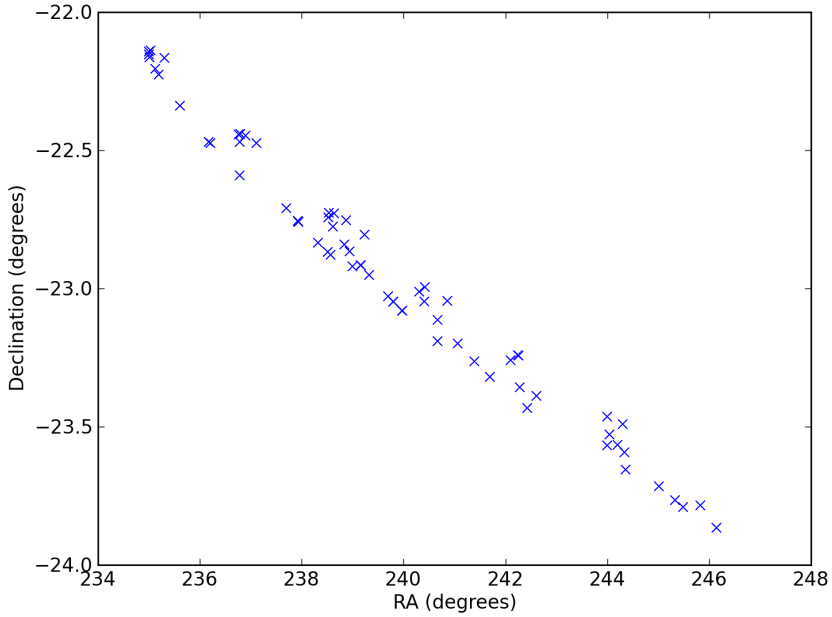

Figure 3.15 The track of a test TNO (a = 55 AU, e = 0.3, i = 3°) as it would have been seen in the Uppsala survey, 2004-9. The sky motion displays the characteristic looping retrograde pattern induced by the Earth's track around the Sun. The survey field of view is 2.048 x 2.055 degrees; e.g. one field extends the height of the plot.

axis of an orbit may be imprecise from a single-opposition triplet, but r_{helio} and the inclination of the orbit should be secure. An r_{helio} variation of < 10 AU accounts quite adequately for $\delta r_{helio}/\delta t$ for trans-Neptunian orbits in the five-year span of the Uppsala survey. We added information on each triplet's orbital inclination by reprocessing them with Bernstein & Khushalani (2000)'s `abg-to-aei` script.

We therefore decided to be bold, and linked triplets together with more wide-ranging criteria than those used for filtering the triplets:

- Two valid triplets, from any time in the survey, on the same field.
- Arc mirror-duplicates (i, j) and (j, i) were not both processed.
- Component triplets' orbits have $\delta i < 10°$ and $\delta r_{helio} < 10$ AU.
- All unique observations in the arc are from separate nights: a given TNO should only be seen once on each night. (Two triplets could share a transient, but it was not required).
- A valid arc must be at least four observations long (otherwise the triplets would be identical).

These suitable triplet pairs were then processed as a single arc in linear turn through `orbfit`, with no magnitude cuts and no Keplerian least-squares filtering at any stage. An arc was kept if it passed the same filter settings as previously used, Eq. 3.1.

3.3.6. Processing arcs

From the 2,257 fields of the the 30+ epoch dataset with which we began, 1,491 passed processing all the way to completion of arc finding: a survey of 6,275.1 square degrees. 92 of these completely processed fields produced 145 arcs (Table 3.2). The arcs showed retrograde sky motion by their potential objects, as we thought would occur, for example the arcs in Fig. 3.12 are curled. Most of the arcs were four observations long; a very few were five long, but there were no six-source arcs.

The next step was then to return to the original images and inspect these survivors.

3.3.7. Visual inspection of orbital arcs

While purely algorithmic filtering could take the 10^{12} possible 3-observation arcs of the astronomical transients down to a few hundred > 3-observation arcs, it could not provide final confirmation that the objects detected were real. Our final step in the pipeline was therefore to collect "postage stamps" of each transient from the `.fits` images from which the astronomical transients had originally been drawn by `SExtractor`.

We extracted an arcmin-square stamp centred on the location from all dates within the arc. This did assume that the pixel scale is constant across the sky, ie. a flat focal plane, which is plausible, but problematic at times near the corners of the Uppsala field (as discussed in § 3.3.2). We could normally obtain postage stamps from four images per night, and the multiplicity aided the eye in determining if the source appeared real. After trying with scripted `ds9`, this was implemented via `pyfits` and `astLib`. The overall postage-stamp generation was reasonably slow, as each compressed image took twelve seconds to decompress.

We structured the postage stamps so that the location of each of the transients in the arc was also shown for the dates of the other transients in the arc: an m-by-m grid (Fig. 3.16). This immediately showed if the transients were real minor-planet detections: they would show as a single source with blank space at the other dates. If it was instead spurious, it showed as a source at the same location that popped in and out of the noise on other dates. The squares were left black if there was no observation on that date of that location, or if that location was not within the field on that date. We found later that (Larsen et al. 2007) had used the same approach to a stamp inspection layout in their archival TNO survey.

With our visual inspection of the 145 plausible arcs completed, none of the arcs were real. The failures were due to blended sources and sources popping just out of the noise.

Given that the search of the arcs was unsuccessful, we made a second check of the triplets. One of the strengths of this survey is that it is sensitive to bright moving objects where other southern surveys would be saturated: for example, at 14^{th} magnitude, Pluto would saturate in the surveys of Sheppard et al. (2011) and of Rabinowitz et al. (2012).

We therefore checked the initial ~ 14 million triplets for any such exceedingly bright objects: we generated image stamps of the triplets that had mean magnitudes < 16 with a standard deviation across the triplet of < 0.25 magnitudes. This produced 747 triplets. Investigating the image stamps of these triplets showed no likely objects.

The survey therefore detected no new TNOs.

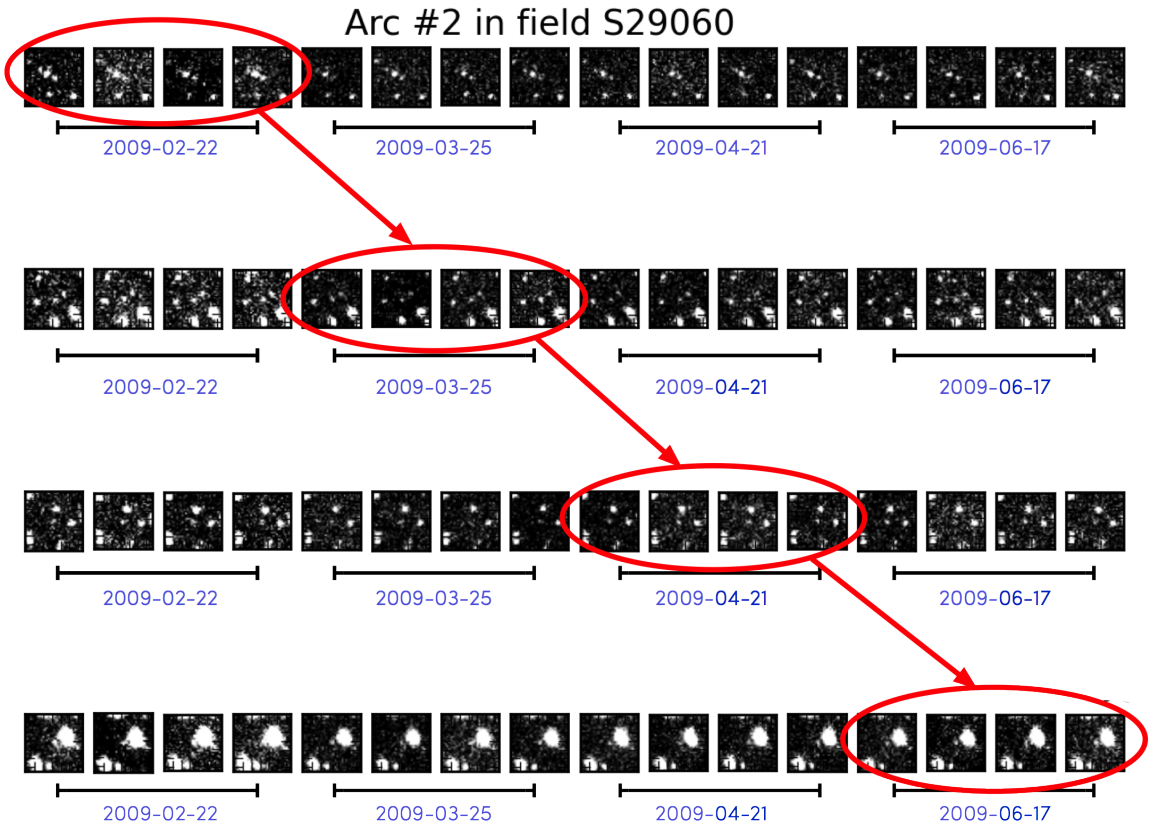

Figure 3.16 Structure of the inspection of what the pipeline considered a valid arc. The arc as a whole is indicated by the linked chain of red circles forming a left-to-right diagonal. The transient's four images on a given night are circled in red; the rest of the images in its row show that sky location on the other dates that were selected for the arc. This immediately showed if a transient was truly temporary: the transient would appear as a new central point source in the "postage stamps" within the red circle, but would not be present when compared to the stamps in the rest of the row. A newly discovered TNO would show such a new point source in all of the arc's red circles. This example arc is a false positive, not a discovery, as the component transients reappear in their rows.

3.4. Results

We developed and ran the Uppsala pipeline while iteratively improving the design and rerunning each module, before passing the output on to the subsequent module. The successfully processed fields contained pleasingly few outcomes given the vast quantity of data that had to be sifted.

For example, we consider one of the 92 fields that generated at least quadruplet-length orbital arcs, the field S25021 (03:01, -25:12), which had 35 nights of observation. This field produced one quadruplet-arc from the filtered 28 TNO orbits of the 39219 that survived the initial least-squares orbit filtering from the 956026 possible triplets of its 6561 transients (Fig. 3.17). This arc had $r_{helio} = 38.5$, $e = 0.59$, $\chi^2 = 73.8$, with a mean magnitude of 19.9: in principle it seemed very KBO-like, but it was not a real object.

The amount of data processed and the result of the processing are shown in Table 3.2: this computational effort took on the order of 10^5 CPU-hours. This table forms the primary overview of the analysis requirements of the Uppsala TNO survey.

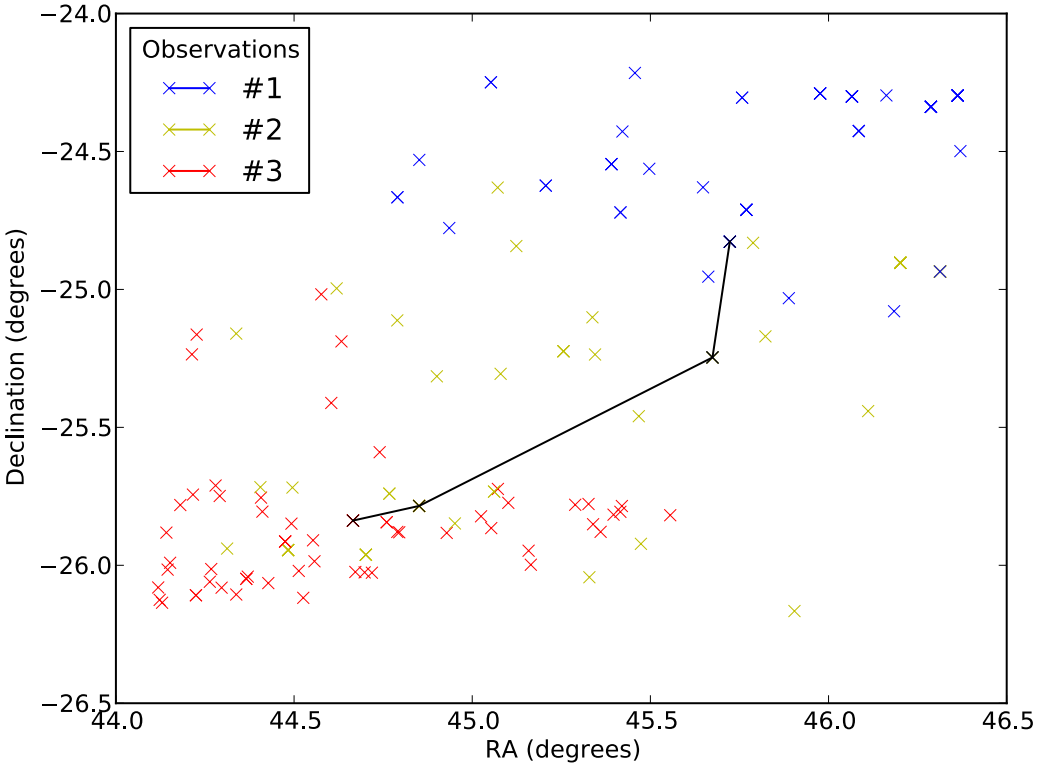

Figure 3.17 The spatial distribution of the `Sources` in the valid orbital triplets found for an example Uppsala field, S25021 (03:01, -25:12). Blue, yellow, red crosses indicate the first, second and third observations in the triplet. The overlaid black line is the longer arc, four observations long, that was found on the field: it did not prove to be a real object under inspection by `stamp_collector`.

Table 3.2 Results of the Uppsala TNO pipeline.

Input	Output	discussed
4.6×10^5 images	2.3×10^9 `Sources`*	§ 3.3.1
2.3×10^9 `Sources`	1.3×10^7 transients	§ 3.3.2
	7.2×10^7 stars	
10^{12} possible 3-obs arcs‡	8.7×10^6 valid 3-obs arcs	§ 3.3.3
2.0×10^7 plausible > 3-obs arcs$^\#$	145 valid > 3-obs arcs	§ 3.3.5
145 valid arcs	0 real arcs	§ 3.3.7
114727 nights†	**No TNO detections**	**taking 10^5 CPU-hours**

* These are the `Sources` produced by combining the `SExtractor` output from the images of a single field taken on a single night.

‡ 1.4×10^9 3-observation arcs (triplets) passed the Keplerian least-squares filter; the output are those of these that passed all `orbfit` and orbital-parameter-cut filtering.

$^\#$ Survived the r_{helio} and i-matching requirement of the component triplets and were fitted by `orbfit`. Valid arcs are those that then passed the Eq. 3.1 parameter cuts.

† Each of the 2257 4.21 square degree fields had between 30 and 82 nights of observation; the pipeline treats a night (four combined images) as its basic unit of processing.

3.5. Summary

To determine if a given source was transient, the source lists from the four images of a field on a night were compared and combined: this step was possible due to the slow object motion rate and the seeing-matched plate scale of 1.2 arcsec/pixel. This introduced cutoff in minimum heliocentric distance is intentionally close to the motion detection limit of the standard Catalina pipeline: a 15 ″/hr fast-moving Centaur. Filtering via a plausible-orbit least-squares fit was necessary to reduce the sheer quantity of potential orbits from considering sets of three of these sources.

This filter kept bound orbits with suitable orbital parameters and quality of fit; the filtered triplet orbits were then fully fit using the `orbfit` code of Bernstein & Khushalani (2000), and selected under the criteria of heliocentric distance > 15 AU, $a > 0$, $e < 1$, $\chi^2 < 100$. This still left too large a number of potential candidates to blink visually. The dense temporal coverage meant that any object appearing on a given field would reappear within the survey's five years in many more than one triplet. We subsequently linked all permutations of two triplets into arcs and refit the arcs, to see if any arcs remained. Visual blinking was used to assess the validity of the arc.

No TNOs were detected in the Uppsala dataset with our pipeline. We completely processed 6,275.1 square degrees of sky; the remainder of the initial 9,498.9 square degrees that began in the processing await the resolution of various irregularities in the data, particularly occasional nights where the WCS did not solve.

3.5.1. Future work

Remaining parts of the survey dataset

There were 766 fields that had sufficient nights, but for various reasons did not make it all the way through the pipeline: 2,257 standard fields had more than 30 nights, 2,193 had night-by-night `Source` lists, 2,136 survived to producing fully matched lists of stationary sources across the observed nights of the field, but only 1,491 produced output from finding arcs, with 92 containing > 3-observation arcs. The pipeline needs tweaking to account for the unfinished fields' peculiarities and complete their processing.

For completeness, the fields with fewer than 30 nights of observation also need to be processed. This may be less than effective due to their sparse observations. However, there are 441 fields with between 20 and 29 nights of observation. Twenty nights spread across the Uppsala timespan in theory could provide the minimum four observations per opposition season needed to find arcs with this pipeline design. Processing these fields would add another 1856.0 square degrees to the survey, above and beyond the 9,498.9 of initial input, bringing the survey sky coverage up to 28% of the sky.

Arcs across multiple fields

Our triplet creation dealt only with orbital motion on individual fields, though across the whole timespan of the survey. Linking triplets across multiple fields is a plausible

progression: objects continue to move, and every successful linkage found increases the chance of finding a real object.

However, extending our method to the computationally demanding task of processing adjacent fields as single units is difficult: while adjacent fields are generally observed together on the same night, the tessellation unit would vary much more in size over the course of the survey than does the observation of a single field. It would be difficult to find multi-field tessellation units constant across the whole survey that could be used as the base units of computation. It would also be more difficult to determine magnitude limits for the tessellations, which cannot be found as easily as that of the individual fields. The transients drawn from the tessellations would be biased toward faint objects, so would not provide an adequate calibration dataset.

We refrained from implementing this technique until after testing the geometric losses of the survey in full; the loss of distant objects would have to be severe to justify adding this complexity.

Image subtraction

Image subtraction could be added as a final step of data analysis: after being confident that the pipeline was working accurately and well, this processing could remove clutter from the images, to produce a clean list of transients from each night that would confirm the results from the other processing method. Image subtraction would only be tried if the detection efficiency of the current pipeline turns out to be unacceptable. We therefore proceed to our analysis of the Uppsala TNO survey detection efficiency.

CHAPTER 4

Analysis of the Uppsala TNO survey

> And whatever islands may be
> Under or over the sea
> It is something different, something
> Nobody counted on.
>
> – Allen Curnow
> *The Unhistoric Story*

A wide-field all-sky survey for trans-Neptunian objects is useful only when we can define its effectiveness at finding these distant moving objects. With the initial characterisation of the Uppsala survey dataset complete, with no TNO detections, the next step was to assess the detection efficiency of the survey.

The Uppsala TNO survey is useful once we can say how accurately, and how precisely, it examined the survey area of the southern sky. The lack of bright objects it found can then be considered as a constraint on the sky density of large TNOs, which also provides its corollary, a measurement on the upper end of the luminosity function of TNOs. This constraint provides a check on existing models of TNO size distribution, which are normally fit by a power law (Fraser & Kavelaars 2008).

To calculate this sky density, certain parameters of the survey must be found. In the previous chapter, we determined the temporal and the spatial coverage of the survey. Here, we add our examination of the calibrated magnitudes (§ 4.1) and calculation of the magnitude limits (§ 4.2) of a subset of the 114,727 nights of the 9,498.9 degrees^2 that we analysed, specifically the subset of 6,275 degrees^2 that we examined in the previous chapter for TNO arcs.

These parameters of the survey were then used as input to a survey simulator (§ 4.3). We created this simulator to apply the exact observations of the Uppsala survey to a synthetic population of several tens of thousands of TNOs. We selected the populations built by Grav et al. (2011), and measured how many were recovered in our observations according to our pipeline's design restrictions. This allows us to define the detection limits of the Uppsala

TNO survey and its efficiency of TNO detection (§ 4.4). With those, we place constraints on the trans-Neptunian populations, in particular bright objects in the orbital parameter space occupied by the scattered disk and Kuiper belt (§ 4.5).

This chapter then concludes in § 4.6, with a short outline of future work in § 4.7.

4.1. Magnitude calibration

The magnitudes recorded in our images are not necessarily accurate. The values obtained by `SExtractor` are converted from the incident photon flux via the known gain of the detector and the assumptions of choosing a suitable aperture within which to gather the flux, and setting a magnitude zero-point (Table 3.1). To have a known true apparent flux and corresponding apparent magnitude for our sources, they required photometric calibration.

Observing photometric standard stars was the most straightforward way to calibrate our Uppsala TNO survey. The Uppsala survey did not make supplementary observations of photometric standard stars as part of its operations, so serendipitous imaging of some standard stars was the best that could be hoped. These standards would need to be comparatively faint, > 14^{th} and if possible up to 19^{th} magnitude, distributed across a very wide range of southerly declinations, and at sufficient density to provide at least one and preferably many more per Uppsala field.

Working with the limited numbers of standard stars is unproductive. For example, the half-thousand 11.5–16.0 magnitude standards of Landolt (1992) are near the celestial equator, offering calibration to only a few Uppsala fields. Likewise, the standards of Graham (1982), while at -45 declination, are few in number beyond 14^{th} magnitude.

Our calibration instead needed to use an all-sky catalogue that has calibrated the magnitudes of its stars. Stetson (2000)'s Landolt-derived set of fifteen thousand fainter standards began to approach this requirement, but not enough were sufficiently faint. Of the more extensive surveys, the catalogue observed by the Hipparcos satellite, Tycho 2.0 (Høg et al. 2000), with a density of ~ 60 stars/deg^2, only goes to 12^{th} magnitude. Its use would require the < 12^{th} magnitude stars to be unsaturated, which does not happen with Uppsala data.

In the north, the Sloan Digital Sky Survey (SDSS) offers better than 2% photometric accuracy in a catalogue that goes to magnitude 22.2 in g and r across a quarter of the whole sky (Aihara et al. 2011). While this would seem ideal for calibrating TNO surveys, its sky coverage (Fig. 4.1) is actually insufficient to provide photometry for the whole of the sky coverage of the wide-field TNO surveys that have been made since SDSS. None of them have used it for calibration.

The southern sky lacks a similarly spatially dense, exquisitely accurate photometric catalogue like SDSS; remedying this lack is one of the tasks of SkyMapper's Southern Sky Survey (Keller et al. 2007). Eventually, the Gaia satellite will also provide a dense all-sky faint catalogue. As our analysis is modular, once a catalogue of SDSS-level precision is available for all our survey fields, it will be possible to easily rerun the calculation of the survey efficiency with the improved calibration.

The reduced Uppsala images, with which we constructed the Uppsala TNO survey, had been calibrated against the USNO-A2.0 stellar catalogue. This catalogue is known to be

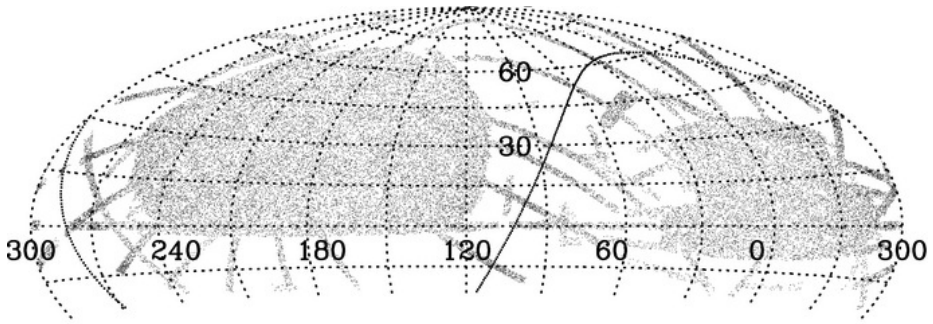

Figure 4.1 The sky coverage in J2000 Equatorial coordinates of the imagery of the SDSS Data Release 8, centred on $\alpha = 120°$, from Aihara et al. (2011). The Galactic plane is indicated by a solid line.

less than ideal: like its predecessor catalogue USNO-A1.0, the source magnitudes have an 0.3 magnitude uncertainty when faintward of 16^{th} magnitude (Monet 1998), and there are systematic zero point variations of up to 0.5 magnitude depending on the position on the sky (Sesar et al. 2006). This is sufficient to term the Uppsala TNO survey "calibrated", but leaves open the possibility of future improvements. We invoke this calibration in determining our magnitude limits.

4.2. Magnitude limits of each night

With sufficiently accurate magnitudes available for all our detected sources, we could then consider what were the faintest objects that we saw. The faintest objects visible on a field on a given night determine the sensitivity of that temporal fractional steradian of the survey.

The Uppsala observations were made in a wide range of photometric and seeing conditions, and during all lunations; this meant the magnitude depth of the images could change by up to half a magnitude from night to night. As the survey is archival, we did not have the liberty available to dedicated-telescope real-time TNO surveys of requesting that fields that did not meet a semi-arbitrary ideal depth in a night be re-observed, to produce a survey with a consistent overall spread of observations all known to reach a given minimum depth. We account for the limitations of the poor Uppsala nights, but do not otherwise exclude them: they provide some sensitivity at the bright end, and we need to understand our retention of bright objects at all magnitudes, down to our images' saturation limit at about 13^{th} magnitude.

As images go fainter, more stars are visible: the density of stars on a field increases with magnitude as a power-law function, modulated by the field's distance from the Galactic plane. The effect of an integration is to detect all stars from the image's saturation magnitude faintward. This constant efficiency of detection continues until the magnitude where the astronomical sources are faint enough that too few photons are received over the length of the integration to raise the sources above the level of noise: this point, indicated by a sudden drop-off in the number of stars of that magnitude that are detected, is the limiting magnitude. The large pixel scale of the Uppsala detector smooths the seeing, so the turnoff does not vary too greatly.

The s-shape of the detection efficiency function is typically fit by an hyperbolic tangent

function (as per Gladman et al. (1998), and widely used in the literature e.g. Trujillo et al. (2001a)) for the detection efficiency η of astronomical sources of magnitude m:

$$\eta = \frac{\eta_{max}}{2}\left(1 - \tanh\frac{m - m^*}{g}\right) \tag{4.1}$$

where η_{max} is the maximum efficiency, $\eta_{max}/2$ is the efficiency at which the magnitude is m^*, and g is the half width (difference between the magnitude at the point of divergence from η_{max} and the magnitude at the half-maximum point).

To determine the stellar efficiency function for each of the nights of our survey, we defined our stars as those that appeared in more than three of the 30+ nights observed on each field. This subsample was taken from the matched candidates obtained in § 3.3.2, and the limit of > 3 nights set to remove noise. (This is a more generous cutoff than the requirement for selection for calibration stars for the internal field-based calibration that we made in § 3.3.2, when we extracted the transients from the Uppsala images to perform our search for TNOs, because we need only count the abundance of stars).

We binned the calibrated magnitudes of the stars finely for each night, using 0.1 magnitude intervals. From these histograms, we needed to obtain the divergence point: where the curve of sensitivity ran into the power increase in number of stars. The fifty percent drop in detections from this point, $\eta_{max}/2$, defined our magnitude limit.

We tried modelling the abundance of stars detected as a power law, but this fit very poorly. This may have been because these detections are still in the bright regime of less than 20^{th} magnitude.

We also tried checking the density of stars on the sky in each magnitude range against the data with the TRILEGAL model (Girardi et al. 2011), which simulates the photometric properties of stars along a given line of sight from a Galactic model that includes a halo, thin and thick disks, and a bulge. As our fields are deliberately more than 10-15 degrees from the Galactic plane, we did not initially expect to see a strong gradient in background stellar density across individual fields; this might have been overly optimistic given the lumpy asymmetry seen in the SDSS Milky Way stellar number density distribution (Juric et al. 2008). Indeed, at (0 RA, -20) we found 250 stars on a field, while at (60, -40), there were 32,000 stars: TRILEGAL did not fit well to these observations, as shown in Fig. 4.2. Clearly a comprehensive all-sky survey like SkyMapper (Keller et al. 2007) is needed to improve such models.

For each night of each field, we instead applied two fits. First, a third-degree polynomial to all the binned stars of the field (eg. Fig. 4.3), and second, an hyperbolic tangent function to the fraction of the total $n > 3$ stars of the field that occurred in each magnitude bin on that night (as in Fig. 4.4).

First, for the polynomial fit, we compared the abundance of stars of each night to that of all the stars that existed on the field for each mag bin, retaining the peaks of the histograms (if the histogram had a flat top, we retained the fainter point). These showed as anticipated the s-curve of the dropping sensitivity of the fractional detections faintward of the histogram peak of each night.

The polynomial was fitted to the detections between the lower saturation limit at $m = 13.0$ and the magnitude of the top of the histogram; after this magnitude the detections would

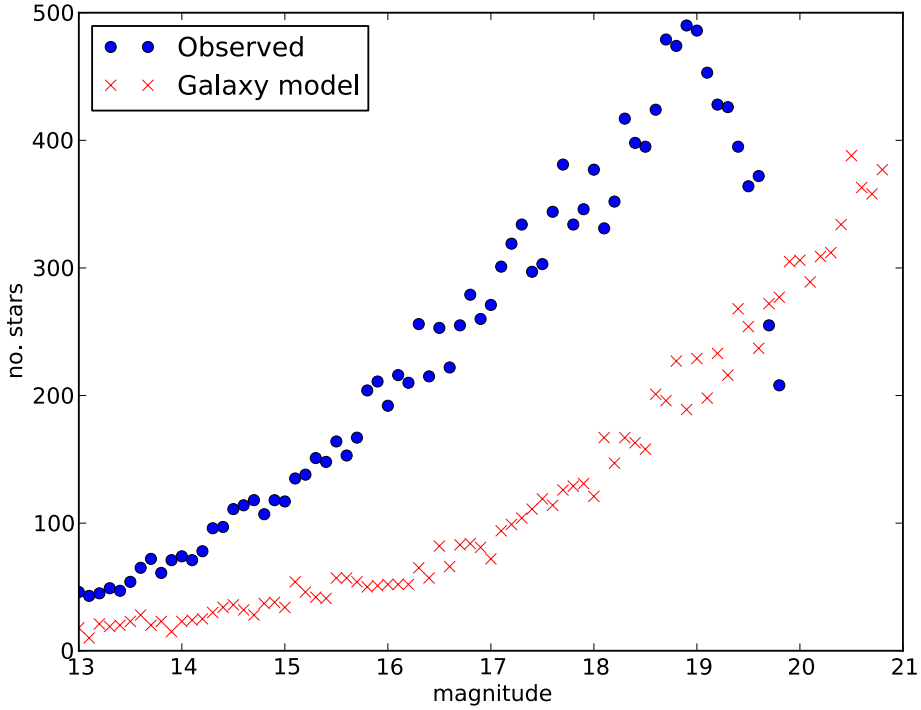

Figure 4.2 The TRILEGAL model of stellar density as a function of location on the sky did not well fit the observed Uppsala stellar density, here shown for the magnitudes of stars seen ≥ 3 nights on example field S17078 (10:49, -17:10).

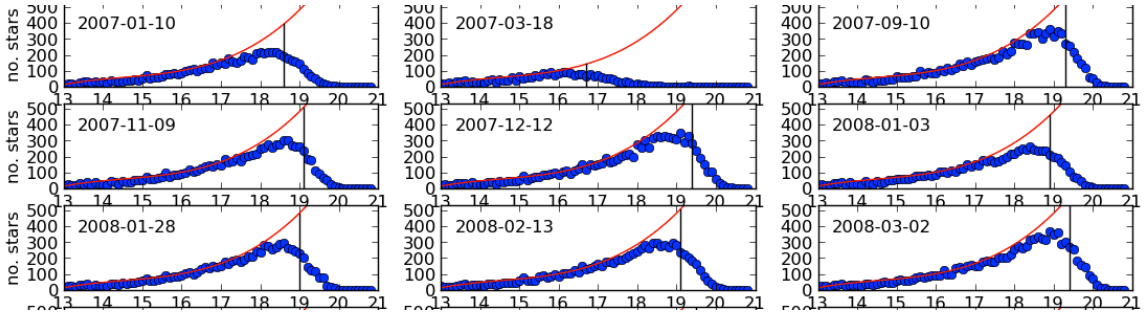

Figure 4.3 Polynomial fit to the binned histograms of stars seen from magnitude 13–21 on example field S39022 (03:39, -39:19) on a subset of all of the nights the field was observed; vertical line shows the 50% cutoff.

diverge and warp the fitting. We then extrapolated it faintward, to where the measured stars detected dropped below 50% of the extrapolation.

The polynomial's magnitude limit and half-width formed the initial seed for the least-squares fitting of an hyperbolic tangent function to the fractional abundance of stars per magnitude bin. This hyperbolic tangent function gave the maximum detection efficiency, the half-maximum magnitude (magnitude limit), and its half-width. The success of the fit was also flagged, based on its residuals, to allow poor fits to be rejected. Successful nights were required to have a maximum efficiency above 0.8. The magnitude limits for several nights of an example field can be seen in Fig. 4.4.

As Sesar et al. (2006) found that the RMS scatter in the photometric error of the USNO-A2.0 magnitudes which which this survey is calibrated is 0.234 magnitudes, we take the

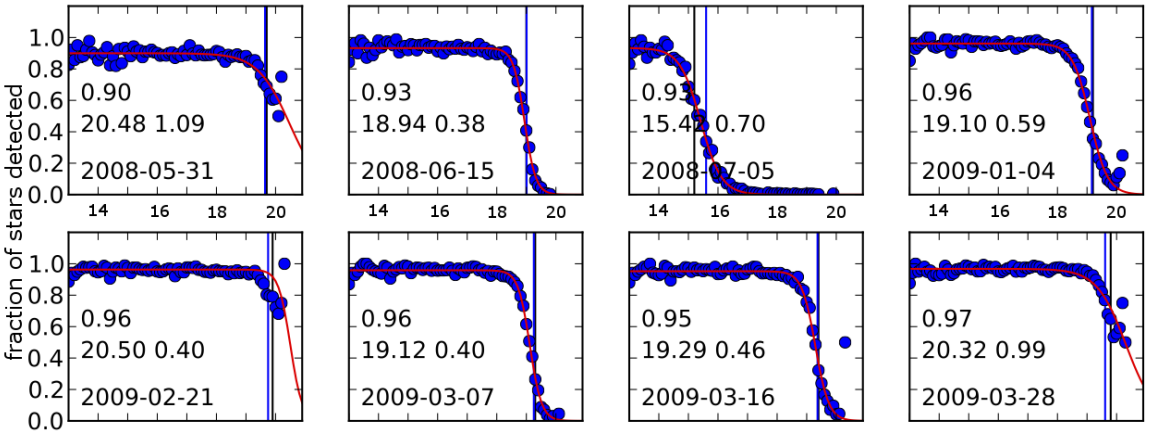

Figure 4.4 Magnitude limits for a subset of the observed nights of S17073 (10:07, -17:08), from fitting to the fractional proportion of the stars on the field detected that night over the magnitude ranges m = 13.0–21.0. Each night indicates its maximum efficiency η_{max}, the limiting magnitude where $\eta_{max}/2$ occurs, and the half-width g of the hyperbolic tangent fit on its plot. Vertical lines indicate the 50% cutoff calculated by fitting the fractional proportion of stars detected with a polynomial (black) or with a hyperbolic tangent function (blue). Note the poor seeing on 2008-07-05.

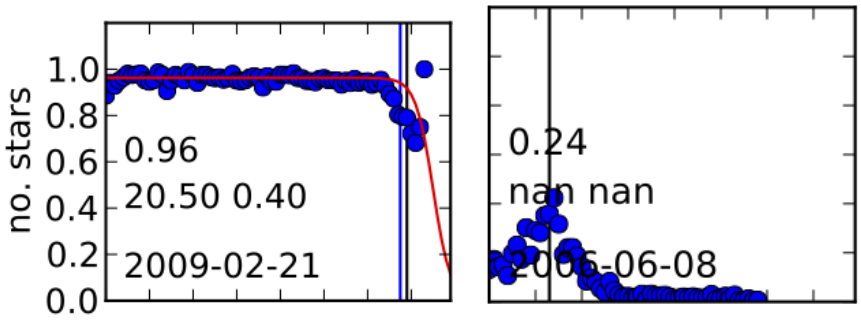

(a) S17073, 2009-02-21 **(b)** S17073, 2006-06-08

Figure 4.5 The two causes of failure to fit the brightness sensitivity of individual nights, shown as stellar fraction on the field as a function of observed magnitude m =13.0-21.0. Left: an exceedingly good night, one of the better of the field's forty nights; right: a highly non-photometric night, not used in determining the survey efficiency.

uncertainty in our limiting magnitude for each night to be 0.2 magnitudes.

The more fortunate situations of nights that went unusually deep were also flagged: those with a magnitude limit deeper than 20.5 and a half-width greater than 0.5 magnitude. We reset these to the more justifiable values of a magnitude limit of 20.5 and a half-width of 0.4 (empirically drawn values from inspection of many fits) (Fig. 4.5a). The paradoxical problem was that as the deepest nights form the baseline for the star catalogue of each field, the deepest nights appear as near-straight lines as fractions of the total stars, such as Fig. 4.5a, and so were very hard to fit with an hyperbolic tangent function: the stars simply suddenly disappear after a point very close to $m \sim 20.5$.

A very small proportion of nights of some fields were not well fit, as seen in Fig. 4.5b. For these, we noted which were anomalous — primarily due to primarily poor seeing — and skipped the night, permissible due to the temporal density of our coverage.

With the nightly magnitude limits found, we could move to calculating our survey's efficiency of object detection.

4.3. The survey simulator

The lack of detections found from the data reduction in Chapter 3 places a restriction on the usefulness of the Uppsala survey: it is hard to accept the validity and trust the survey when there are no objects to provide "sky truth" that the pipeline works. The testing to show that it would detect objects if they were there has to be both comprehensive and robust. For this, we built a survey simulator.

This comprehensive structure applies the known Uppsala survey, exactly as it was observed, to a population of outer Solar System objects. It then provides detailed information on which objects it was able to recover, and the reasons for object loss.

Once the Uppsala TNO survey was processed (Ch. 3), we needed a way to determine for any given object in the outer Solar System, if it fell on our fields, the probability that it would have been found. Tombaugh (1961) could rely on the effectiveness of his eyes and mind to claim that "[t]he planet search work was done with such care and thoroughness that the author believes that no unknown distant planets brighter than the sixteenth magnitude exist and that any planet between magnitudes 16 and 17 had a good chance to be discovered." Subsequent researchers have quantified this process.

The uncertainty in the efficiency of TNO surveys is often estimated by the number of known objects, particularly multi-opposition TNOs, that they recover: this forms the ultimate proof of survey effectiveness for surveys that over at least part of their sky coverage reexamine shallower-surveyed sky.

We did not detect any TNOs in our survey. In addition, the known trans-Neptunian objects according to the Minor Planet Center's classifications[1] showed no multi-opposition objects with $a > 30$ AU and visual magnitudes < 20.5 that fell on our survey images.

Unrecovered known objects, and the corresponding reasons for their loss, offer a measure of the uncertainty in a survey's efficiency: detection of known objects can suitably be considered rare events, so Poisson counting statistics apply. For example, Schwamb et al. (2010) use their detection statistics of KBOs $\leq 21^{st}$ magnitude, those that were below their median image limiting magnitude, to obtain an efficiency of 68% for their survey; this value was Poisson-uncertain to 1σ between the range 51–89%. Using this technique does produce large uncertainties in efficiency. We did not have this option for constraining our efficiency for the Uppsala TNO survey.

The TNO magnitude distribution is sufficiently steep, with a fourfold increase in object abundance per magnitude of depth, that most known objects found will be right at the limiting magnitude of a TNO survey (Trujillo & Brown 2003). Assessing the offset between the observed magnitudes and the known magnitudes of recovered objects thus also permits calibration of the survey magnitude limits, though only crudely, as the object magnitudes retained by the Minor Planet Center (MPC) are themselves generally uncalibrated. Under

[1] The MPC's List of Transneptunian Objects and List of Centaurs and Scattered-Disk Objects, Feb. 2013.

testing by Romanishin & Tegler (2005), ninety of the MPC TNOs were systematically 0.3 magnitudes fainter than their MPC-recorded values.

We therefore cannot use the discovery statistics to calibrate both efficiency and magnitude limits, as did Trujillo & Brown (2003) and numerous other wide-field surveys, cf. Schwamb et al. (2010); Rabinowitz et al. (2012). In addition, our search technique's requirement to merge together the observations made within a single night (§ 3.3.2) purposely removes asteroids, known and unknown alike. We did this to minimise their otherwise overwhelming abundance in observations made under motion rate confusion conditions. Unfortunately, this means we cannot use comparisons of their serendipitous occurrence in the observations to known well-measured asteroids to calibrate,[2] as did Rabinowitz et al. (2012).

4.3.1. Selecting a population model

The Uppsala TNO survey can provide constraints on the existence of TNOs within the strictly defined region of orbital parameter phase space within which it could detect objects: this is the capability of the survey that can be characterised. The orbital phase space is parameterised in terms of semimajor axis a, eccentricity e and inclination i space; the other three parameters of longitude of the ascending node, argument of perihelion, and mean anomaly (Ω, ω, M respectively) are secondary.

The survey's lack of new TNO detections prevent it from providing sufficient fine-grained resolution to distinguish between models of Solar System formation; it is possible for multiple models to imply that we would have had zero detections. We therefore do not try to overstretch the dataset to provide these kinds of answers. However, this survey can provide strict definitions on the existence of bright TNOs within a constrained region.

We therefore use a test population of small bodies that fulfils the requirement of testing if the survey is complete in each quantum of phase space, without being too concerned whether it is the "best" possible outer Solar System population model available at this point in time to test the survey against. It need only well sample the orbital phase space.

The test populations we chose were those of Grav et al. (2011): their Centaurs and classical, resonant, and scattered trans-Neptunian objects. They built each population by convolving a well-known dynamical model with the best available observed size distribution (equivalently, absolute magnitude distribution). With this, they generated objects sampling the population's orbital distributions of a, e and i, then randomised uniformly on Ω and ω in their 0-360 degree ranges, and selected M based on the time of perihelion passage, all in abundances corresponding to the size distributions. The random orbital orientations rendered the orbital epochs unimportant (Grav et al. 2011). They retained objects that when at perihelion had apparent magnitudes that were brighter than the limiting magnitude of their survey of interest, Pan-Starrs, at $V = 24.5$. This cutoff is unimportant for our application, as we are only concerned with sampling their orbital distributions.

The Grav et al. (2011) TNO population is substantial, with 108,022 Centaurs, 48,682 KBOs (predominantly classical; only about six thousand are resonant objects), and 10,951 scattered

[2] In theory we could; in practise it would require reprocessing the whole dataset again only to specifically extract them, taking some large part of 10^5 hours processing time.

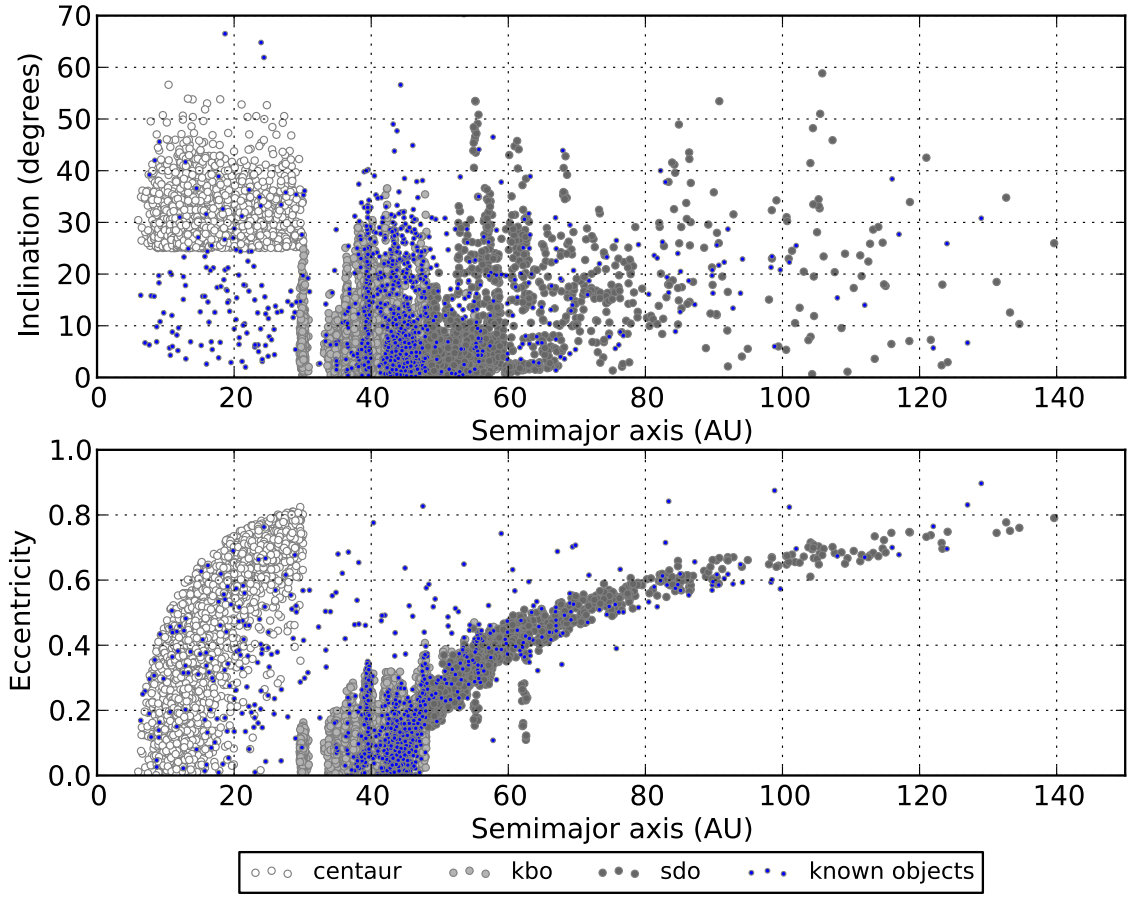

Figure 4.6 The orbital distribution of the artificial objects that could be observed by the Uppsala survey: 1,821 Centaurs (a subset, all have $i > 25°$), 8,898 KBOs and 2,077 scattered disk objects from the population model of Grav et al. (2011); shading identifies population. These are shown in more detail, with their parent populations, in Figs. 4.7, 4.8 and 4.9. Smaller blue dots are the TNOs known by the Minor Planet Center as of 9 February 2013.

disk objects.[3] Unfortunately, this abundance of 167,655 objects leaves us with too many objects to be run through the survey simulator in a practical amount of time. A subset of the Grav et al. (2011) populations, those that would be visible in Uppsala observations (as determined subsequently in § 4.3.3), are shown in Fig. 4.6, together with the entire set of known TNOs for comparison. The less numerous scattered disk and Kuiper belt are tractable to process, but it was possible to consider only a subset of the multitudinous Centaurs in this thesis; the rest may follow later.

The more than a hundred thousand Grav et al. (2011) Centaurs are defined as $5.5 \leq a \leq 30$ AU and $q > 5.2$ AU, many of which would be excluded by being too northern on the sky to fall on our fields. We will be able to better detect the higher-inclination population, as the sky density of a given inclination of objects peaks just below the ecliptic latitude corresponding to that inclination (Gladman et al. 2012). Given our survey coverage is of a significantly larger fraction of the sky above $\sim 20°$ (Fig. 3.7), it was reasonable to first test our sensitivity to this subset. Of the overall 108,022 objects, there are 35,628 Centaurs with $i > 20°$, 20,375 with $i > 25°$ and 10,499 with $i > 30°$. We opted to assess the Centaurs with $i > 25°$; this proportion provided a good sample that could be processed in a feasible amount of time

[3] As obtained from the now-defunct website listed in their paper.

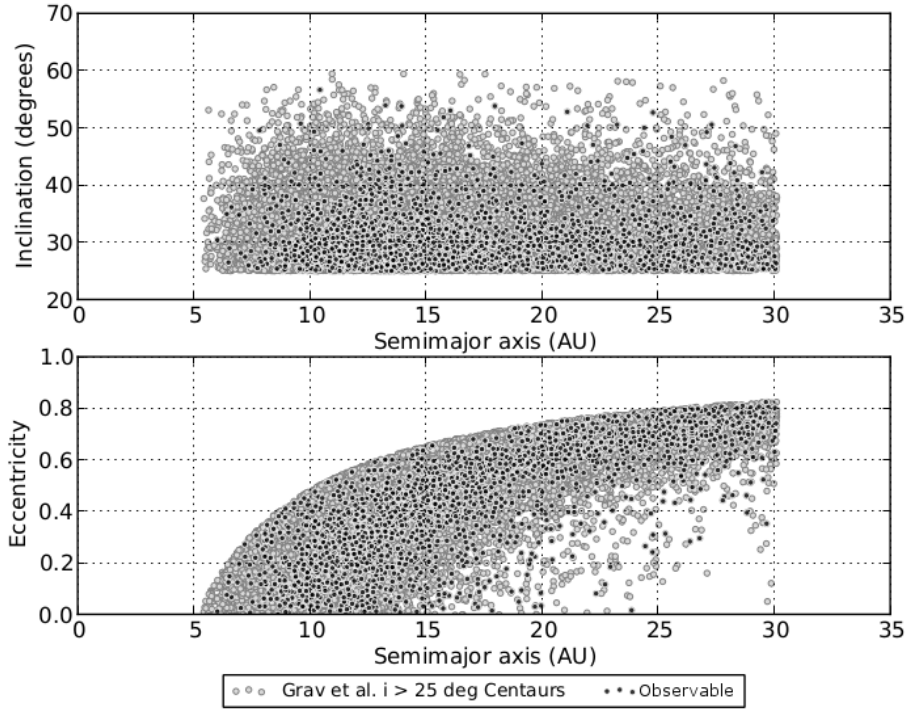

Figure 4.7 The orbital distribution of the 20,375 Centaurs with $i > 25°$ in the population model of Grav et al. (2011) (note the artificial trimming this imposes across the lower end of the inclination distribution). Those 1,821 objects that are observable by the Uppsala survey are darker.

(Fig. 4.7) and was well matched to our fractional sky coverage.

The Kuiper belt population of Grav et al. (2011) display the expected low dispersion of inclinations of this comparatively minimally-excited population; of the 48,682 KBOs in the population model, 8,898 objects are observable by the Uppsala survey (Fig. 4.8). They occur densely on the survey's low-ecliptic-latitude fields.

The scattered disk of the Grav et al. (2011) model is our population of primary interest, as it offers abundant high-inclination objects not present in the Kuiper belt; about two thousand of these fall within our survey's predominantly high-latitude coverage (Fig. 4.9). This synthetic population are the survivors of integrating the Nice model's simulation B (Levison et al. 2008; Morbidelli et al. 2008) over billions of years: they are less excited than the known real population, lacking the high-inclination and high-eccentricity objects, as the only mechanism available for orbital excitation in the model is resonance pumping (Grav et al. 2011). The synthetic SDOs also lack large-perihelion objects like (90377) Sedna (q = 76.3 AU).

This is partly due to being based on a set of test TNOs that date from the early days of modelling in the field of TNO studies. The late-1990s survey of Trujillo et al. (2000) prompted Duncan (1998) to model the dynamics of the scattered disk, but they used a small population of seven objects. These objects have been used by all further workers to extrapolate a population for the scattered disk. In principle this may introduce biases as it is based on a small limited survey; Trujillo et al. (2000) were well aware of their limitations. The comprehensive and comparable modern such survey is CFEPS (Petit et al. 2011); the scattered disk size distribution has been modelled from that survey by Shankman et al. (2013), though

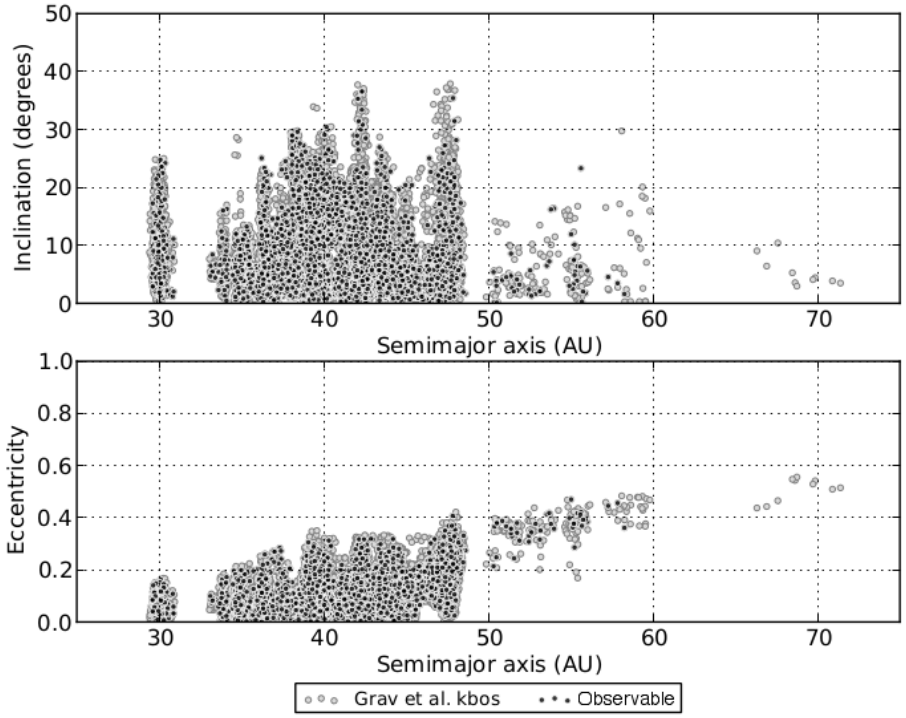

Figure 4.8 The orbital distribution of the 48,682 KBOs in the population model of Grav et al. (2011); those 8,898 objects that are observable by the Uppsala survey are darker.

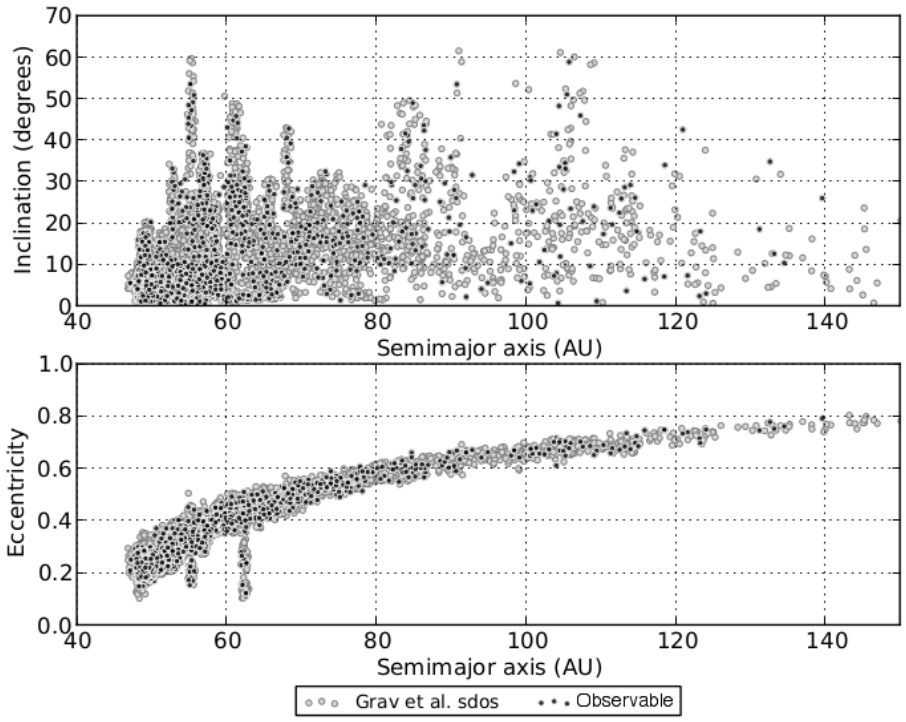

Figure 4.9 The orbital distribution of the 10,951 scattered disk objects in the population model of Grav et al. (2011); the semimajor axis range is truncated at 140 AU for legibility of detail in the denser parts of the population, though the maximum a in the population is 1181 AU. Those 2,077 objects that are observable by the Uppsala survey are darker.

no appropriate population model from that work to replace the late-90s model has yet been published.

Given that the Uppsala survey has such incredible time baselines, it should be sensitive to motions at great distances; the orbital model is inadequate to characterise the survey's sensitivity to this potential population. We appreciate this weakness in the orbital model, and consider how it might be addressed in § 4.7.2.

4.3.2. Input

There are different stages at which we could have added the synthetic TNOs into the pipeline. Adding sources with appropriate point-spread functions to the images, rerunning `SExtractor`, and regenerating the matched candidates and subsequent survey processing would confirm that randomly located transients were found correctly by the transient identifying scripts. However, this complete reprocessing of the survey, with its associated 10^5 CPU-hours, is counterproductive if future workers ever wished to try different TNO models against the Uppsala survey.

We instead took the approach of assuming that the survey's transient and matched candidate lists were adequate, due to our earlier testing. We instead chose to deal with individual synthetic objects on an object-by-object basis, which allowed us to consider them merely as very small transient lists, which were run through the entire pipeline as were the normal transient lists, with a few extra checks and simplifications that are detailed in later sections. In this approach, the synthetic objects first encounter the temporal sampling of the observations that the survey made, which allowed us to sub-select a population that meet our geometric constraints. We then assessed the survival of this subset through the processing pipeline.

We adopt the orbital elements of the Grav et al. (2011) population to our requirements: we ensure each synthetic object has a known semimajor axis, eccentricity, inclination, longitude of the ascending node, argument of perihelion, mean anomaly, epoch in Modified Julian Date (MJD) and identification string. We then determined the sky position and sky motion of these objects over the duration of the Uppsala observations.

4.3.3. Populating the Uppsala fields

A survey can be considered 100% efficient at detection if it found all objects that were detectable, by falling within the geometric and magnitude constraints of its imaging; what always remains undetectable is the orbital-element phase space that produces geometric locations that fall outside the survey area during the span of the survey. To determine our survey's efficiency we must first know what part of orbital phase space is detectable; for our survey to detect an object, it must first fall on the main Uppsala survey fields.

The span of time over which we had to work was sufficiently large that the quality of the propagation of the elements from the epoch of the orbital elements became significant. We noticed this when our test calculations of the ephemerides of known objects had better than arcsecond accuracy at the end of the survey, which was within a year or so of the current epoch, but on calculating celestial positions at the beginning of the Uppsala survey in 2004

showed an inaccuracy of several arcseconds when compared to those predicted by the equivalent web-based service of JPL HORIZONS. This seemed odd as we used the C-language routines of the SLALIB library,[4] which is used for most major telescope control systems, to obtain geocentric J2000 coordinates with correction for annual aberration and light-time.[5]

The few-arcsecond deviation was eventually found to be due to the lack of calculating full-planetary perturbation in the SLALIB wrapper: it simply assumes that the orbit for the object is entirely defined by the orbital elements. JPL HORIZONS starts with the orbital elements at their epoch and iterates forwards or backwards in time to the point requested, taking into account gravitational perturbations from other Solar System bodies and using the DE405 data from JPL.[6]

We therefore acknowledge that our 2004 ephemerides are less precise, by a few arcseconds, than those later in the survey. However, this is not overly significant, because later in the pipeline we create our initial triplets of orbital arcs only within each opposition season, so the tolerance did not have to be meticulous.

Each object was projected against the night sky over the duration of the survey; an initial rough subset of objects in the synthetic population were retained based on their ephemerides as calculated every seven days. This interval was chosen as a Centaur's maximum motion rate of 15″ per hour, or 6 arcmin per day, would produce a minimum side-to-side field crossing time of 20.5 days, modulo the looping effects of retrograde motion; for three observations to occur, this required an ephemeris calculation interval of 6.83 days, which we rounded. With 2061 nights between 2004-03-03 and 2009-10-24 (padding the span of the survey by a day in each direction for careful overlap), this required the calculation of 295 ephemerides for each synthetic object. From these celestial positions, synthetic TNOs were kept for further processing if they fell within the corner-to-centre distance of 1.4506 deg of the field centre of any Uppsala field (according to the field centre list, Appendix A.1).

Once the synthetic TNO was determined to be on a field, we refined this rough cut, precisely matching to the exact cadence of the observed survey. For each observation on each night made of each of these fields, we obtained the positions of the synthetic TNOs at the moment the field was observed, confirmed that they were indeed within the image that was made, were within a seeing disk each night, and finally calculated which of those would have blended with a star on the field.

As the search radius forms a circle, and the Uppsala fields are near-square in spherical coordinate space and overlapped longitudinally (as visible in Fig. 4.10), reducing the area corresponding to the field from that of our initial search, we reconfirmed that each given

[4]We appreciate the suggestion of Jon Nielsen to use SLALIB and his subsequent assistance in repackaging this portion of SLALIB into a standalone command line utility, `orbephem`.

[5]While it does not correct for leap seconds, this made only a very slight difference as calculations are only back to 2004.

[6]This shows up an interesting hole in the development of the field of TNO studies: dynamicists develop full-perturbation n-body models of the outer Solar System populations, observers require near-epoch celestial coordinates for single or small numbers of objects, but there is seldom a requirement for models that fully propagate great numbers of orbital elements with perturbation to produce accurate celestial coordinates on a significant scale far from the current epoch. JPL HORIZONS is easily scripted for such coordinates for individual known objects, but it is not currently possible (or computationally feasible if it were) to script it for arbitrary orbital elements for the quantity of ephemeris calculations that we require. LSST are implementing this kind of large-scale ephemeris generation for their survey (L. Jones, pers. comm.).

observation of a synthetic TNO did actually fall on the field in question. We loaded the star list for the field and kept the synthetic TNO observation if it was within the maximal (RA, dec) box of the stars. This was a necessary finesse over merely calculating the field corner locations from the declared field centres as the telescope pointing was not perfectly stable from night to night, and varied by up to an arcminute (cf. the alignment problems seen in § 3.3.2).

As in the processing in § 3.3.1, we also only retained observations where the change in position of the synthetic TNO between the start and the end of the observation of that field on that night (generally about 40 minutes elapsed) kept the TNO within the night's seeing disk. This as before placed a constraint on objects' motion rate, but one that only substantially affects Centaurs: the simulator would quantify it.

Paradoxically, this design choice, imposed to optimise detection of objects more distant than asteroids and taking advantage of our preferentially poor-seeing site, penalises nights with good seeing: the smaller seeing disk restricts retention to slow-moving objects, which is suited to our survey's aims, but leads to the occasional loss even of scattered disk observations. This is less than ideal, but our dense cadence sampling makes up for it to a great degree.

The lack of image subtraction in our pipeline design meant that there was a possibility of losing transients if they were superimposed on the fixed stars[7]. If any observations of these synthetic TNOs fell on top of a star, defined as the centre of the stellar PSF and the TNO having an arc separation of less than four arcseconds, the TNO was defined as merged with the star and therefore lost. This was exactly the same test as that used in § 3.3.2 to construct the intranight `Sources` in the original pipeline processing.

We made one simplification from the § 3.3.2 pipeline: loading the star list (matched candidates) of each field was highly time-consuming because the files were so large and complex, so we calculated stellar merges based only on the sky positions of all sources present in the deepest night of that field, rather than on the sources present in that night of that field. The astrometry of the images of the nights of each field varies very little through time, just the pointing, so this seemed an acceptable tradeoff to increase processing speed, balanced in possible missed merges from any astrometric wobbles by the greater density of sources on the deepest night.

Finally, we made a simplification not present in the original pipeline, that is possible only because the synthetic objects are defined in advance: we removed observations where the opposition season of the field on which they fell contained fewer than three observations. Three points are the minimum needed to construct a valid orbital triplet in § 3.3.3, so the overly sparse points would not have survived past that part of the original pipeline. Applying this constraint to the synthetic observations retained only data that would permit a triplet to be linked to a triplet from another opposition season of that field so that longer orbital arcs might be found, as in § 3.3.5. This speeded our processing.

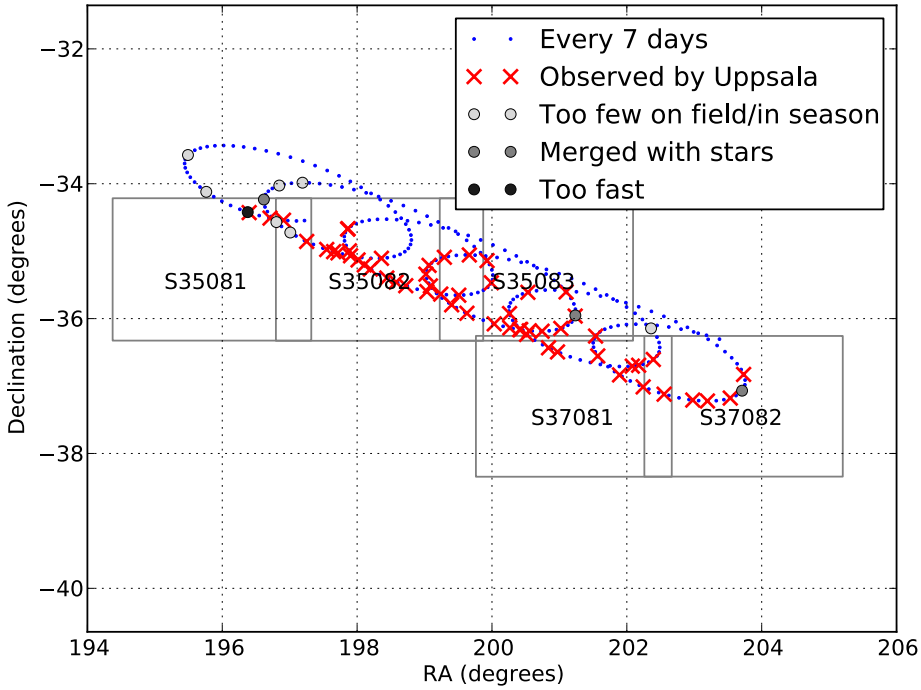

Figure 4.10 The ephemerides of the classical KBO 2010 FX_{86}, $r_h \sim 47$ AU , as it would have been observed by the Uppsala TNO survey if it were bright enough to fall within the survey magnitude limits. Labelled grey boundaries indicate the maximum field boundaries as extracted from the 30+ nights of observation and the name within the Uppsala field naming scheme, for fields that contained Uppsala observations that could be used in the rest of the pipeline. Dots indicate the ephemeris of the TNO every seven days, filled spots the Uppsala observations that could not be used due to selection requirements of the pipeline and the starfield, and crosses the Uppsala observations that definitely could be used for synthetic object recovery in the rest of the pipeline.

4.3.4. Geometric losses

Our constraints produced pleasantly high TNO survival rates. For example, if we consider the simulated Uppsala observation of a known TNO that has a magnitude too faint to detect in our survey, 2010 FX_{86}, we find that its ephemerides are well recovered by the survey (Fig. 4.10). Initial appraisal of its position every seven days showed it to cross nine fields in the span of the survey; 713 of the 2,474 Uppsala images of these fields were made while 2010 FX_{86} nominally crossed these fields. After calculating 356 positions of the TNO for those images' nightly start and stop times, and confirming according to the exact field boundaries which were on their fields, 134 start-stop intranight positions were combined to make 67 single-night observations.

One observation was removed; as discussed above, good seeing can work against our pipeline design, and the on-sky motion rate of the TNO that night of 4.8″ exceeded the required 5σ limit set by the night's seeing of 2.3″. Three observations were lost to merging with stars, by falling within the 4″ separation required in the construction of transients. Seven were subtracted as the opposition season of the field on which they fell contained fewer than three observations, preventing triplet creation.

After these eleven observations were removed, 56 observations, all within sufficiently popu-

[7] We do not distinguish here between stars and galaxies; 'star' is used to mean a sidereal-motion source extracted as a point source by `SExtractor`

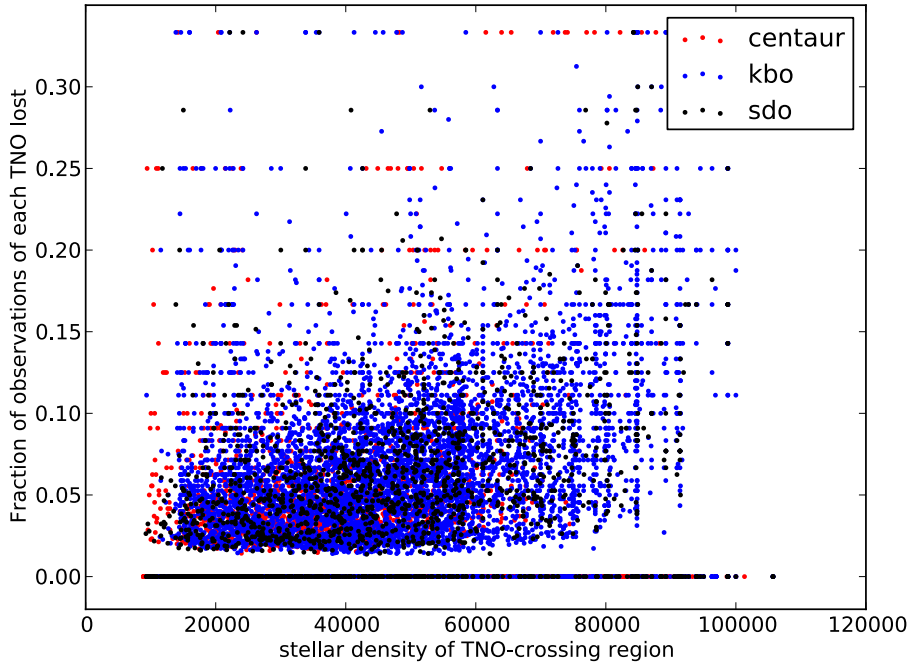

Figure 4.11 Individual observations of the synthetic TNOs of our test populations that crossed the fields of the Uppsala survey that could not be retained as observations of the TNOs due to merges with stars: the predicted TNO position on a given image was within the seeing disc of a known star on that image. The y-axis (and a very small amount of data occurring at a loss fraction of > 0.35) is truncated to better show how the loss of observations is in proportion to the stellar density of the field. The apparent linear structure in places is an artefact of the similar, relatively small numbers of observations.

lated (3+ observations) opposition seasons, on 5 fields, were ready for further processing (Fig. 4.10, red crosses).

Having outlined the survival of a single object, we could then consider the effects of our processing on the observability of each of the three Grav et al. (2011) populations due to geometric effects. We consider each of three geometric causes of loss in turn.

First, the losses due to stellar overlap did not change noticeably — indeed, it should not show variation across the various populations of synthetic TNOs, but should increase linearly with increasing stellar density on the fields. As seen earlier in § 4.2, the survey covers a range of Galactic latitudes and has a corresponding variability in source number density on the fields. If we approximate between the ends of the range of our observed stellar number density per field (a few hundred to 40,000 stars per 4.21 deg^2 field), and assume a point-spread function for each star covering 4″ x 4″, commensurate with our 4″ internight source combination limit, the area of each field covered by stars ranges between 0.01–1%. This probably underestimates the PSF coverage of stars toward the brighter end of the magnitude range: a star close to saturation would cover far more sky. We therefore estimated that there would be on the order of 5% loss of all TNO observations due to stellar mergers. Our full analytical simulator quantification shows that the loss rate was indeed in the 5-10% vicinity for all populations (Fig. 4.11). No synthetic KBO or SDO lost more than one to three of its Uppsala observations to stellar merges, and many lost none. The increase in loss as a function of stellar density of the field was not quite geometrically fourfold as expected, but closely approximated it.

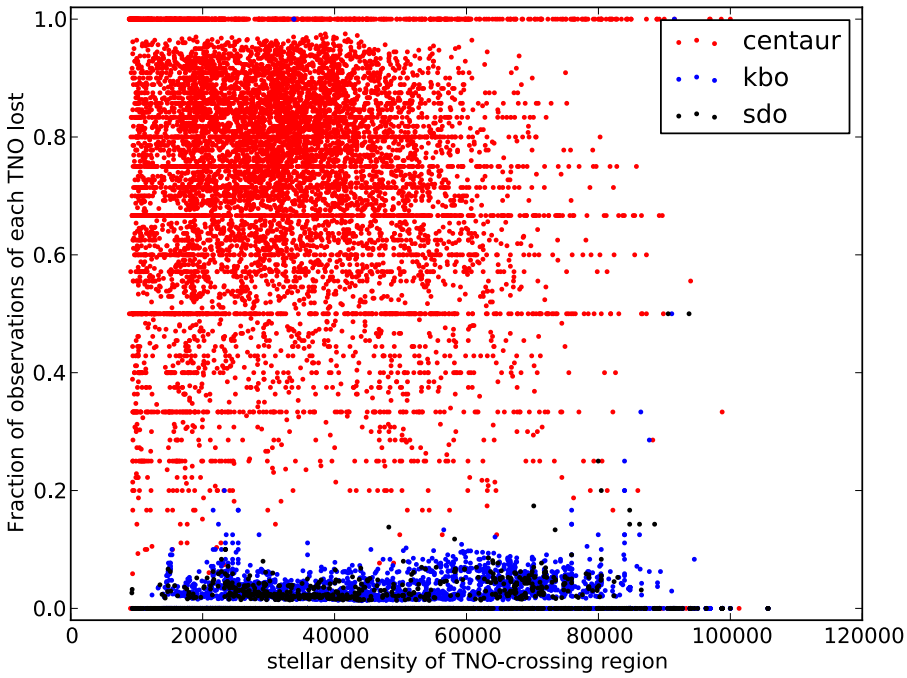

Figure 4.12 Individual observations of the synthetic TNOs of our test populations that crossed the fields of the Uppsala survey that our algorithms deliberately removed: these were eliminated because the TNO motion rate on a given night spread its intranight span out larger than the seeing disk calculated for the night. As expected, the most substantial effect of this imposed condition was on the closest and fastest-moving objects, Centaurs. The apparent linear structure in places is an artefact of the similar, relatively small numbers of observations.

Second, the effect of on-sky motion rate varied strongly between populations (Fig. 4.12). The most-affected population was, as expected, the Centaurs, where there was a severe loss of observations. This was due to the Centaurs' swift on-sky motion from their smaller geocentric distance, which affected their retention: the high motion rate caused the first and last observation of each Centaur on each night to shift outside the night's seeing disk. The KBOs and scattered disk were minimally affected, as intended, losing $< 5\%$ of observations.

Third and finally, our requirement for our initial orbit formation of three or more observations in each field's opposition season affected populations moderately evenly (Fig 4.13), and caused the loss of up to 40% of observations. This may only be a problem if the overall detection efficiency is quite low. Here, interfield linking to form arcs would substantially have improved the retention of observations; this would probably be the easiest way to retrieve enough observations to balance those lost to intranight geometric loss and increase the Centaur detection efficiency.

However, our survey would have been geometrically sensitive to some Centaurs: applying our constraints to the 20,375 Centaurs with $i > 25^\circ$ in the population model of Grav et al. (2011) (Fig. 4.7), we retained 1,821 observable Centaurs, with 9,750 too northern or in the Galactic avoidance zone of the Uppsala survey. 8,738 fell on Uppsala fields, but were too sparsely observed to be further considered for detection, lost for the reasons above.[8] The ephemerides of these observable Centaurs are shown in Fig. 4.14.

[8]There were also 66 Centaurs lost where the ephemeris generation failed; this was how we found that the Grav et al. (2011) model has allowed in some very slightly negative eccentricities (-0.001– -0.004).

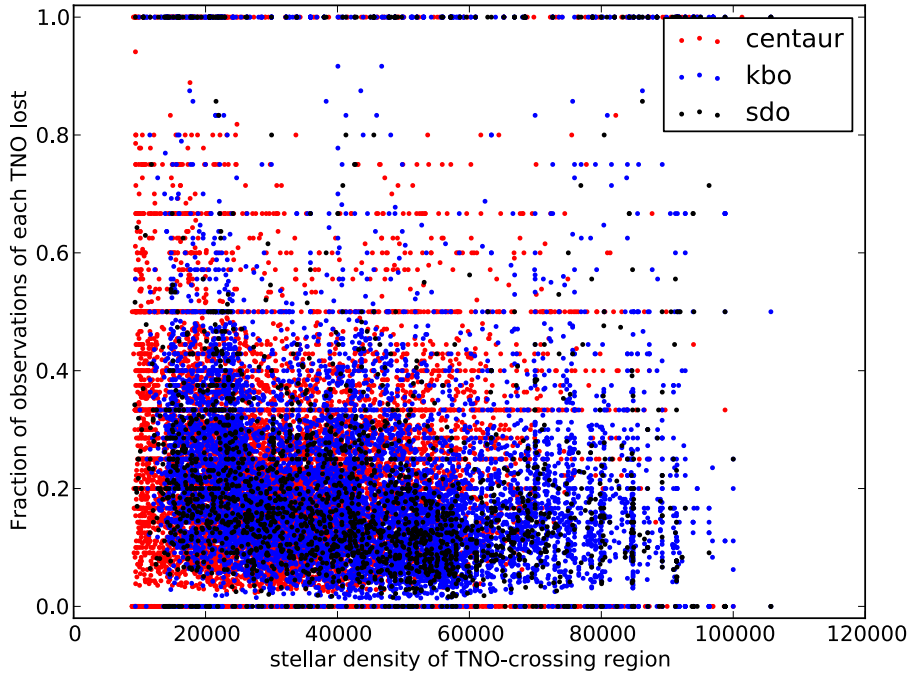

Figure 4.13 Individual observations of the synthetic TNOs of our test populations that crossed the fields of the Uppsala survey that our algorithms deliberately removed: these had to be eliminated due to our algorithmic requirement for orbit calculation that for a given TNO , there had to be more than three observations of it in each opposition on each field. The imposition of this condition produced relatively even geometric losses of individual observations across the three TNO populations, as would be expected given this is a result of the survey cadence sampling rather than the orbital motion. The apparent linear structure in places is an artefact of the similar, relatively small numbers of observations.

The much more numerous KBOs are less orbitally inclined, and highly inclined objects spend most of their time distant from the ecliptic plane. This puts them at a disadvantage for detection in our highly off-ecliptic survey (Fig. 3.7 in the previous chapter indicates how far from the ecliptic most of our sky coverage falls).

Of the initial 48,682 (Fig. 4.8), we retained 8,898 observable KBOs, with 38,353 too northern or in the Galactic avoidance zone, and 1,431 too sparsely observed on our survey fields to be processed any further. This predominantly flat inclination distribution tightly packs the observable KBOs close to the ecliptic (Fig. 4.15).

In contrast, the scattered disk objects have a wider spread of inclinations: of the 10,951 scattered disk objects of Grav et al. (2011), 2,077 became observable TNOs, 8,550 were too northern or fell in the Uppsala galactic avoidance zone, and 324 were on Uppsala fields but too sparsely observed to be processed any further in our pipeline. The observable SDOs are shown in Fig. 4.16. The looping retrograde motion of the scattered disk objects each year is visible, though minute given the scale of sky involved. It can be seen more clearly by considering the motion of individual objects: for example, Fig. 4.17 shows a synthetic scattered disk object that crosses sixteen fields over the course of the survey.

Following this processing of the Grav et al. (2011) outer Solar System populations, we had 1,821 Centaurs, 8,898 KBOs, and 2,077 SDOs, 12,796 in total, for the next stage: determining the detection efficiency by taking into account how these orbits would be observed when

magnitudes are applied.

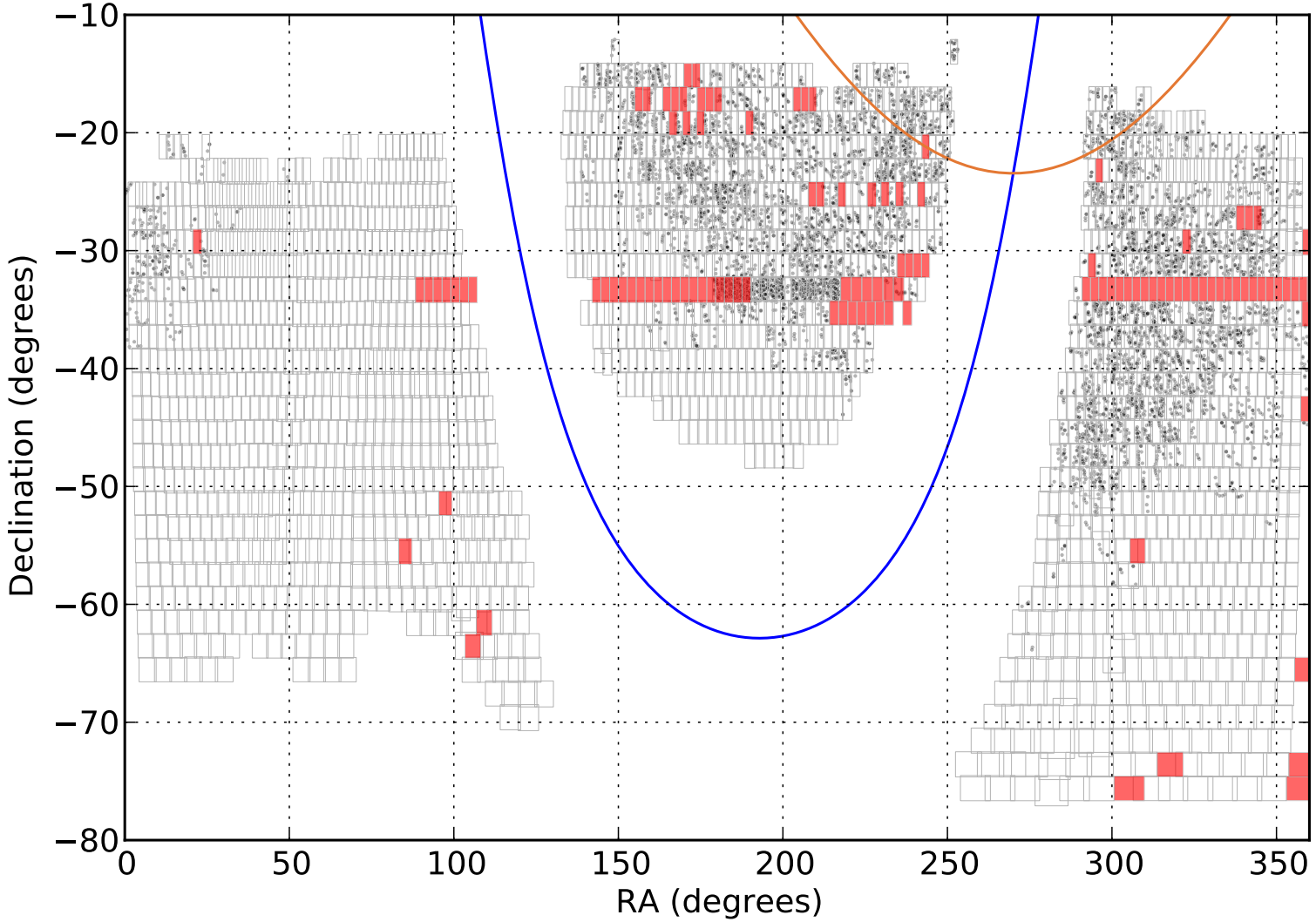

Figure 4.14 The distribution on the sky of the 1,821 Centaurs with $i > 25°$ of Grav et al. (2011) that retained 3+ observations in one opposition on one field when their observation over the span 2004-2009 by the Uppsala survey was simulated. Solid-filled fields indicate un-processable fields, which are considered as gaps in the TNO survey coverage. The galactic plane is the lower, blue solid line; the ecliptic plane is the orange solid line in the upper right.

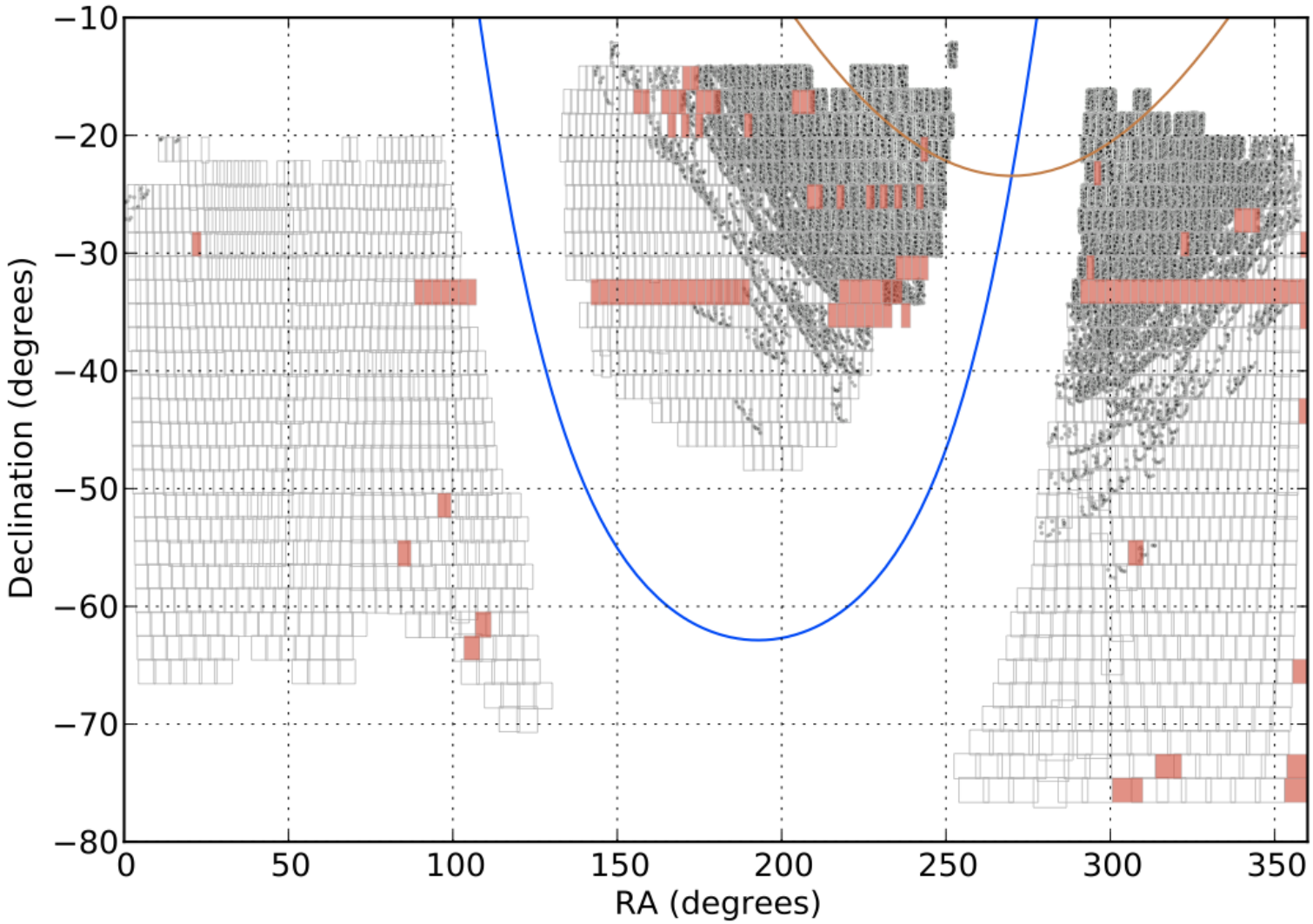

Figure 4.15 The distribution on the sky of the 8,898 objects in the 48,682 KBOs in the population model of Grav et al. (2011) that retained a minimum of three observations in one opposition on one field when their observation over the span 2004-2009 by the Uppsala survey was simulated. Solid fields were not processed and are considered as gaps in coverage. The galactic plane is the lower, blue solid line; the ecliptic plane is the orange solid line in the upper right.

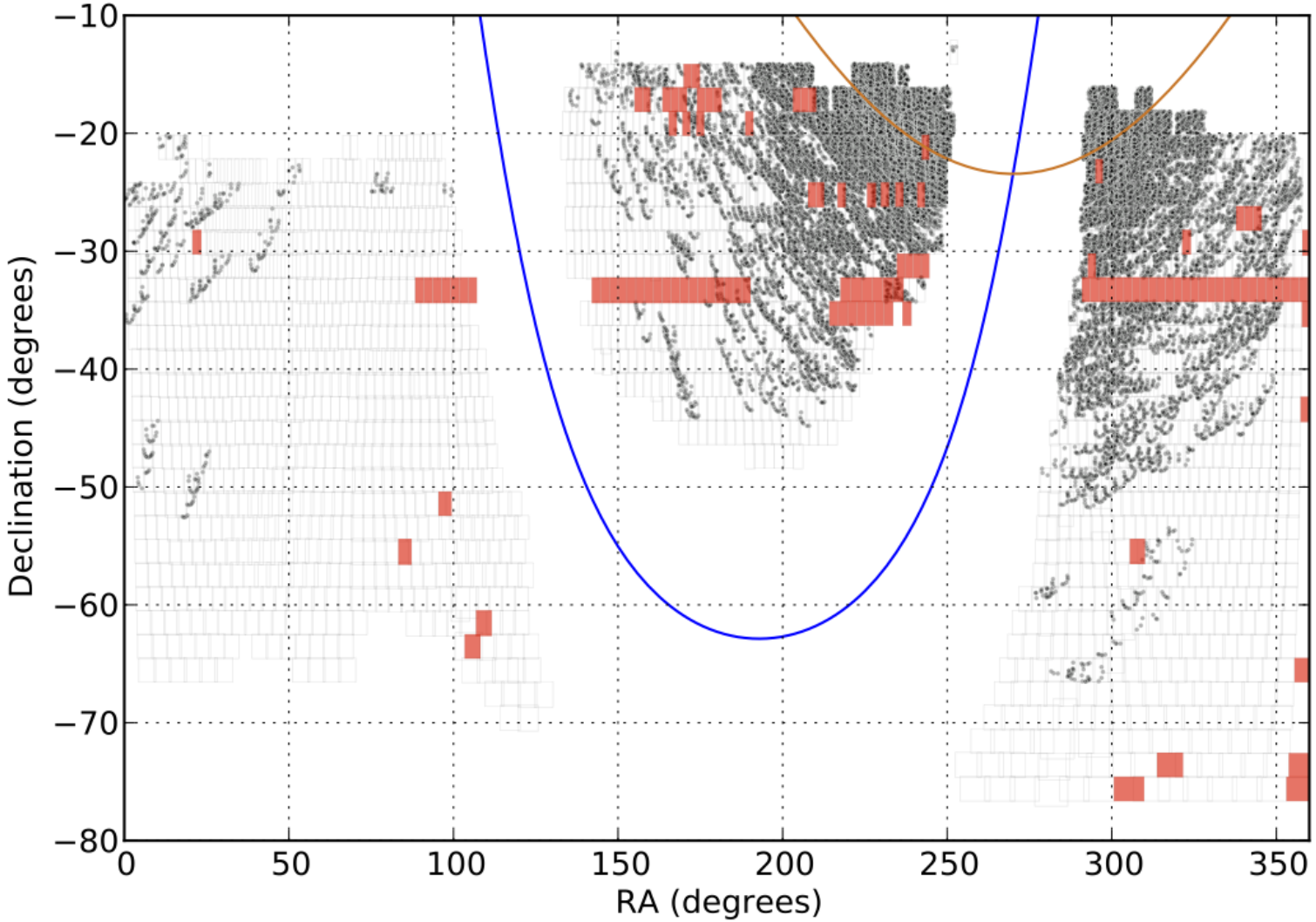

Figure 4.16 The distribution on the sky of the 2,077 objects of the 10,951 scattered disk objects in the population model of Grav et al. (2011) that retained 3+ observations in one opposition on one field when their observation over the span 2004-2009 by the Uppsala survey was simulated. Solid-filled fields indicate unprocessable fields, considered as gaps in coverage. The galactic plane is the lower, blue solid line; the ecliptic plane is the orange solid line in the upper right. Note the scarcity of high-inclination objects, a known flaw in the input population.

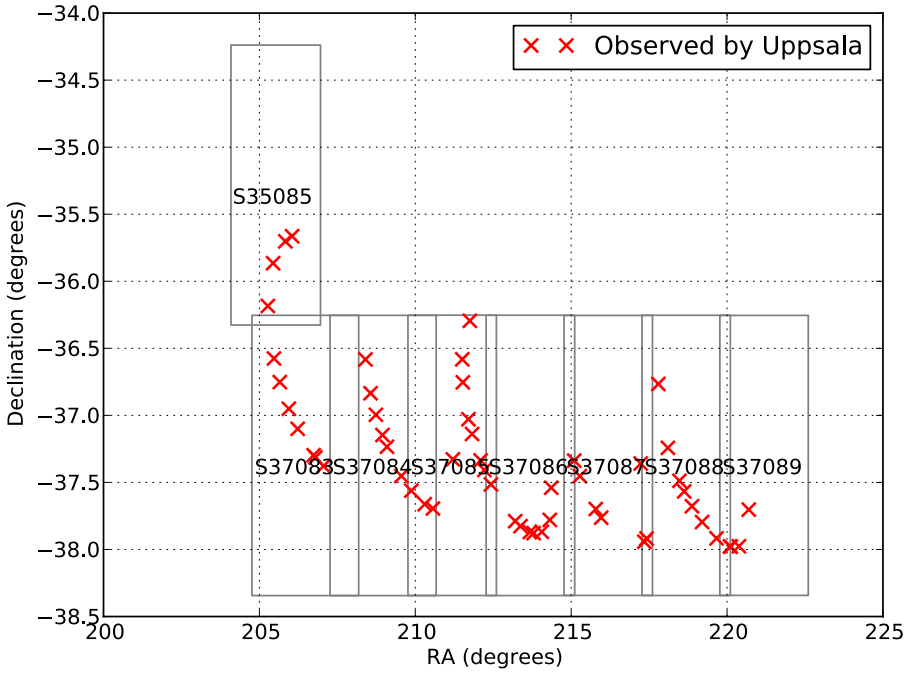

Figure 4.17 The distribution on the sky of the Uppsala observations that meet the requirements of the Uppsala TNO survey of a single Grav et al. (2011) scattered disk object, SS00001na. This TNO crosses sixteen fields in the course of the Uppsala survey: the eight labelled fields (grey rectangles) are those that contain observations with three or more observations in each opposition season.

4.3.5. Assigning absolute magnitudes

Each observable synthetic TNO represented an opportunity to examine a slice in outer Solar System a, e, i orbital parameter space. However, having the piece of parameter space was only part of the picture: we also needed information about the range of brightness within which each of these slices would be detectable, according to the magnitude limits that we had ascertained earlier. As albedo can vary significantly for dwarf-planet size TNOs due to their complex surface processes (§ 1.4.1), we assigned a brightness distribution based on absolute magnitude rather than on object size, and explored the extremes of this distribution within our visible magnitude range.

We assigned each of the nearly thirteen thousand observable TNOs an absolute magnitude range $H_{min} \leq H \leq H_{max}$ according to their parent population, set such that at each end of the H-range the TNO would either saturate or vanish into the noise on all of its confirmed Uppsala-plausible observations. We used $4.5 \leq H_{Centaur} \leq 12.0$, $-3.0 \leq H_{KBO} \leq 5.5$ and $-6.0 \leq H_{SDO} \leq 6.0$. We chose a step within the absolute magnitude range of 0.25 magnitudes as a reasonable compromise between the time for processing and a good resolution of the population.

For each of the synthetic TNOs at each assigned H, we calculated its apparent magnitude due to its heliocentric distance at the time when each of its Uppsala observations were made, using the albedo-independent relationship for rotationally-averaged apparent magnitude

cf. Petit et al. (2008), after Bowell et al. (1989):

$$H =< m_{\text{TNO}} > +2.5log\left[\frac{\phi(\gamma)}{r_H^2\Delta^2}\right] \tag{4.2}$$

$$m_{\text{TNO}} = H_{\text{TNO}} + 2.5\log_{10}(r_H^2(r_H-1)^2) \tag{4.3}$$

with the assumption that the phase angle $\phi(0) = 1$, as at opposition, and the approximation of geocentric distance as $r_H - 1$, with r_H in AU.

We then confirmed that this apparent magnitude was brighter than the magnitude limit for that night on that field. The observation was also labelled with the probability of its detection at that magnitude, according to the sensitivity function for each night found in § 4.2.

This resampled object-observation-subset — often more sparsely sampled, if an object's new magnitude prevented it being observed on many nights — then formed an individual TNO processing unit. Units were filtered by abundance of observations in opposition seasons of fields, and as before, retained for orbital arc processing where at least one field retained three observations of the TNO in one opposition season.

Not all observable objects were run against the magnitude limits, especially in the KBOs, as their fields required the calculation of some fields' magnitude limits that were exceedingly time-consuming relative to the magnitude limits of most fields. 8820 of the 8898 KBOs and 1965 of the 2077 SDOs were processed at the range of H magnitudes. The absolute magnitude range proved slightly too great at the faint end for the scattered disk objects, though this didn't affect the results except to pad with zero detections at $H > 4.5$. The range chosen for the KBOs seemed better suited.

We now had the exact test population that fell on the survey fields: nearly eleven thousand test TNOs retained from the full phase space, each of which had at minimum three observations on one opposition season of one field, moderately well distributed across the fields (Figs. 4.14–4.15). Each TNO, for all its assigned H-magnitudes, now knew its observations of existence in the Uppsala dataset.

4.3.6. Monte Carlo orbital arc creation

We wished to be able to report the reasons for loss or retention of the synthetic TNOs object by object. The Uppsala TNO pipeline (§ 3.3) is structured to process observations in a multiplexed batch manner, with the field as the basic unit. Each TNO had just had the observations per field calculated, so each TNO's fields were fed individually to the Keplerian filter for triplet creation, subsequent orbit-fitting and survivors arc-fitted in the same manner as the normal Uppsala TNO pipeline (§ 3.3.3–3.3.5).

The detection of a TNO requires it to be bright enough to be seen on the observation; however, there is the added complication that the sensitivity curves for any night of any Uppsala field have < 100% efficiency. Many of the transient detections we made in each image fall toward the magnitude limit of each night of each field, where the efficiency is even less.

While the probability of survival of each constituent observation bright enough to be in the flat regime of maximal efficiency is up in the range 0.85–0.97, the overall probability of a

triplet of such observations drops to 0.61–0.91. Those transients at the magnitude limit, on sensitivities of 0.5, sharply lower the overall survivability of triplets and their subsequently linked arcs. A quadruplet orbital arc with all `Sources` scraping in just above the level of noise, at the magnitude limit of 0.5 sensitivity, has just an 0.06 chance of survivability. This means the sensitivity function probabilities cannot be treated as absolute even when the synthetic TNO observations are brighter than the field's magnitude limit.

We therefore took a Monte Carlo approach to the triplet creation and the sensitivity function probabilities. The small, but cumulatively time-consuming need to run `orbfit` in each of the Monte Carlo iterations led to adding an abundance of heuristic constraints that minimised unnecessary computation. With the sets of observations for each absolute magnitude for each TNO, we took the following approach:

- For each iteration, create a set of random probabilities, a P_{night} (0-1) for each night.
- Assess every `Source` against their respective P_{night}: $P_{Source} \geq P_{night}$ = detected.
- Assign detected `Sources` a positional uncertainty, drawn from a normal distribution with μ = 0.3", characteristic of the survey's astrometric uncertainty.
- This forms a new subset of the synthetic TNO's observations, retaining those fields with > 3 observations (arcs require a minimum of four observations and are only formed intrafield).
- Fields are sorted by abundance of observations; we first try finding an arc on the sparsest-observed field, which will process most quickly.
- Run as normal on each field's portion of these observations for triplet creation/arc determination.
- Try triplet creation only if at least one set of three nights within an opposition season existed.
- First try arc creation after finding nine triplets, or vast quantities of arcs were found and processing time became prohibitive.
- Retry with all triplets if the first nine didn't find an arc.
- Collate number of arcs produced for each iteration for each tno.
- If even one arc is found for each tno, cease further examination of the iteration's fields, and record that in this iteration, we detected the TNO in the survey.
- The TNO detection efficiency at that H is the fraction of iterations where an arc was found.

We counted a given synthetic TNO, assigned a certain H-magnitude, as successfully recovered if a minimum of one arc was found on one of its fields. The apparent magnitude corresponding to that H-magnitude's efficiency was counted as the mean of the TNO's apparent magnitude over its fields; the heliocentric distance of these TNOs changed little over the course of the survey, with the maximum variation of any object about 0.1 magnitudes.

Running a thousand of these Monte Carlo iterations would give a 3% uncertainty to the outcome for each H for each TNO, but to perform that for the whole survey, at a thousand per thirty to fifty H-magnitudes per twelve thousand synthetic TNOs, required the calculation of approximately 600 million iterations. We erred on the side of computational accessibility and ran 100 iterations per absolute magnitude value, which gave a 10% uncertainty to each H-magnitude outcome. This dropped the required calculation of confirmed detectability to some 60 million iterations, requiring a few 10^3 CPU-hours.

4.3.7. Output

We could then report the outcomes for individual successful TNOs with the following level of detail, tracking all component `Sources`:

- TNO always too northern to reach any Uppsala fields, or southern but fell in the Galactic avoidance zone.
- TNO fell on an Uppsala field
  - the field was in the main survey
  - observations were made in the timespan when the TNO crossed the field
  - the TNO position was within the field box bounds and had no star merge
  - the TNO 's H-magnitude produced > 3 observations brighter than their nights' magnitude limits: Monte Carlo testing could commence
    - a field contained > 3 observations of a TNO when randomised per-night probabilities were applied to it
    - the TNO had enough observations to form in-season triplets on at least one field
    - the triplets survived the Keplerian filter and orbit fitting
    - there were enough triplets to form at least an arc.

This allowed us to identify the efficiency of the pipeline at every level.

We also examined the recovery of arcs on a field-by-field efficiency before implementing the efficiency as a function of each TNO's detection in the whole survey: this allowed us to confirm how effective the field-by-field checking worked. For example, the synthetic scattered disk object SS00015Aa had Uppsala observations on seven fields: between $H = -2.0$ and 4.25, five of the fields had detection efficiencies that began at saturation apparent magnitudes as 80-100%, and stayed roughly constant at that maximum efficiency on each field over the next several absolute magnitudes. The greatest absolute magnitude at which the TNO's efficiency remained above zero subsequently varied between fields. This was a product of the variation in magnitude depth and density of the temporal sampling of each field.

From this, we could move to the overall survey detection efficiencies, computed from the per-TNO efficiency.

4.4. Survey efficiency

Our pipeline detection efficiency is the fraction of the synthetic objects detected: for each synthetic TNO, did at least one orbital arc make it through to the final stage in the pipeline. Even if the throughput efficiency is very low otherwise, if at least one arc survives so that the TNO counts as detected at that apparent magnitude, the efficiency is sufficient to be well covering the orbital phase space of the Solar System and the survey is adequate to its purpose.

However, we found that most synthetic objects as distant as the Kuiper belt or further produced several hundred arcs at the final stage. This verification confirmed that any real bright TNO, such as a dwarf planet, within the survey parameter space would have emblazoned itself across the output.

Having obtained the outcomes of running the survey against our test populations, we binned the brightnesses of the objects by 0.1 mag intervals; they spanned from the saturation magnitude at 13.0 to about 20^{th} magnitude. From the mean efficiency in each magnitude bin, we produced an overall survey efficiency as a function of magnitude (Fig. 4.18). The slight stepwise effect around maximum efficiency is due to the absolute magnitudes at which the TNOs were checked having been sampled at 0.25 magnitude intervals. As mentioned earlier in § 4.2, Sesar et al. (2006) found that the RMS scatter in the photometric error of the USNO-A2.0 magnitudes which which this survey is calibrated was 0.234 magnitudes when calibrated against the 0.02 mag scatter SDSS; we therefore take the uncertainty in our survey limiting magnitude per population to be 0.2 magnitudes.

A least-squares fit to these efficiencies with the function in Eq. 4.1 showed that the maximum survey efficiency was 0.90 ± 0.01 for Kuiper belt objects, 0.92 ± 0.01 for scattered disk objects; effectively identical. The 50% detection efficiency, which we take as our limiting magnitude $m*$, was also effectively identical for the two orbital classes: $m*_{kb's} = 18.9 \pm 0.2$ and $m*_{sdos} = 19.0 \pm 0.2$.

The plot of Centaur efficiency is not shown in Fig. 4.18, as the detection efficiency of this population was astonishingly near-zero: a sample of several hundred of the 1,821 nominally observable Centaurs did not find any retrievable under the Monte Carlo methodology applied above. The optimisation of our survey design to the outermost Solar System proved too restrictive to this population.

As we add small positional uncertainties and calculate orbital arcs with `orbfit`, we are testing the effectiveness of Bernstein & Khushalani (2000)'s implementation. However, the majority of the objects missed were lost because of undersampling within opposition seasons rather than from `orbfit` errors; the sheer density of revisitation of the fields was enough to pull past the rare triplet or arc loss seen in individual `orbfit` attempts, preventing the 5% loss of synthetic objects found in Bernstein & Khushalani (2000)-computed Sedna simulations by Schwamb et al. (2010). While full confirmation of the correct operation of the Uppsala TNO survey would come on running known TNOs through the full pipeline, prevented as none bright enough existed within the survey coverage, this 90% efficiency confirms that our survey is useful for characterising the distant Solar System.

Our overall survey efficiency for distant objects improves slightly (by 0.05 to 0.15) on that

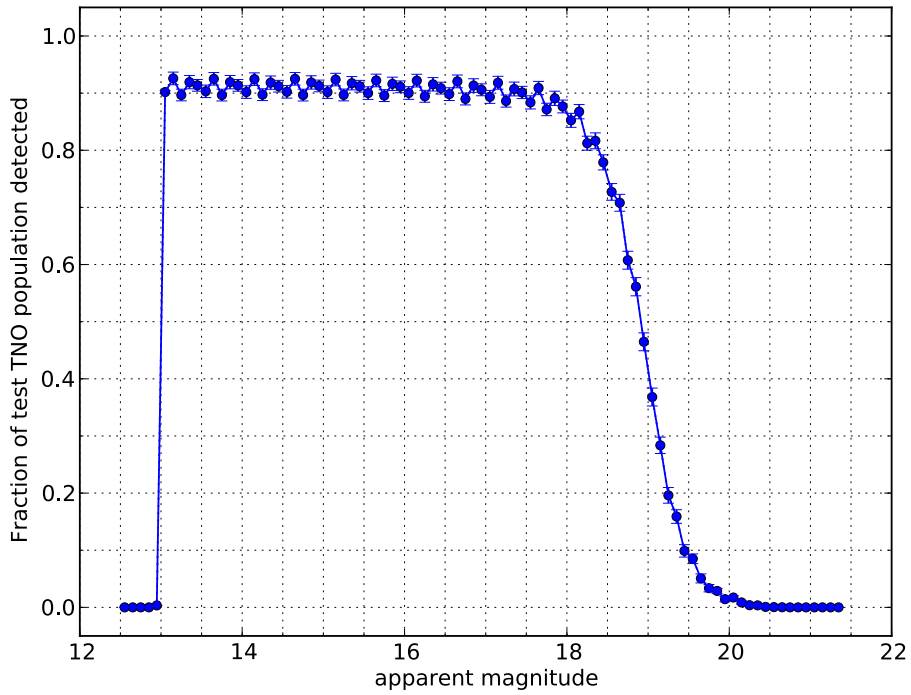

(a) Kuiper belt objects: 1459 objects (drawn from the 8898 observable), with an efficiency function with $\eta_{max} = 0.90, \eta_{max}/2 = 18.90, g = 0.52$.

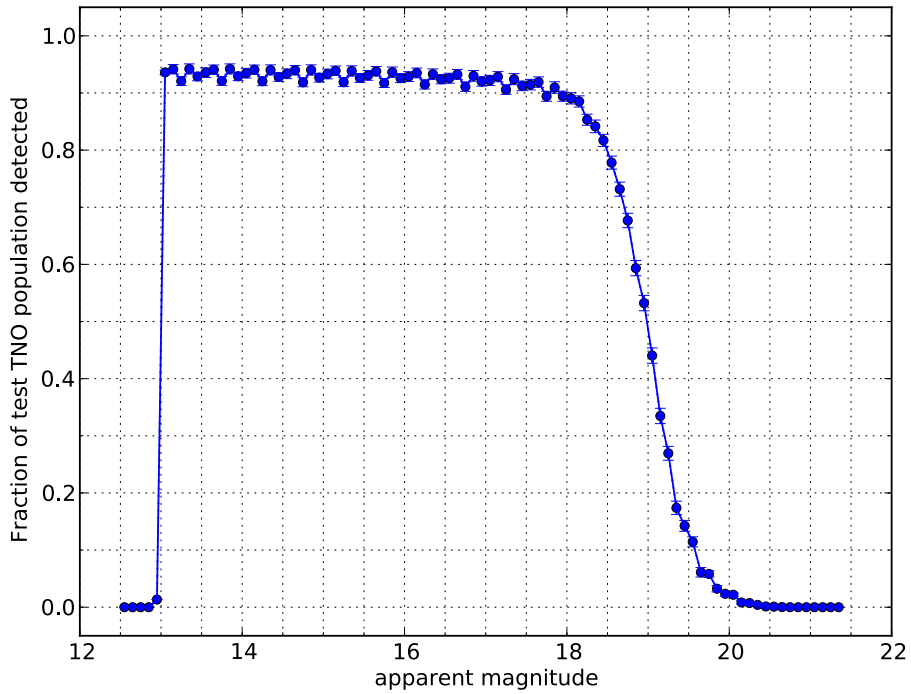

(b) Scattered disk objects: 1965 (drawn from the 2077 objects observable), with an efficiency function with $\eta_{max} = 0.92, \eta_{max}/2 = 18.96, g = 0.53$.

Figure 4.18 The efficiency of detection of the synthetic TNOs re-detected in the survey simulator via Monte Carlo iteration per absolute magnitude unit and comparison of the resulting apparent magnitudes against the nightly magnitude limits. The blue line is the mean population detection efficiency per 0.1 apparent mag bin, with its uncertainty the standard error of the mean.

of Rabinowitz et al. (2012), over the visible magnitude range of m = 15–19 where we are comparable. We presume that the efficiency of Sheppard et al. (2011) in the overlapping range with our own is comparable, as at m = 20.5 it is identical to ours, but they do not show their efficiencies over our magnitude range. (Both surveys' limiting magnitudes are $m_r \geq 21$.)

The earlier, smaller sky survey of Sheppard et al. (2000) with the Automated Patrol Telescope at SSO obtained a 50% KBO detection efficiency at a similar limiting magnitude of m_r = 18.8. It is interesting to note that their calculation of their efficiency used 100 objects randomly placed on a subset of their 1428 sq. deg. sky coverage; our computation of $\sim$ 60 million simulations of TNO detection to determine our our detection efficiency is a reflection of the increased computational power available twelve years later.

The constraints that we applied to the creation of triplets and subsequent arcs made our survey less sensitive to faster-moving objects. With the lack of recovery and exceedingly low detection efficiency of Centaurs, our survey examines only the orbital properties of the Kuiper belt and scattered disk.

4.5. Constraints on the trans-Neptunian population

With this survey, we provide constraints on where bright TNOs cannot exist in the outer Solar System: if they existed, we would have had a 90% chance of seeing them, within our carefully defined boundaries. The elaborate check of absolute magnitude as a function of orbital parameter space allows us to confirm our sensitivities to the various trans-Neptunian populations: which objects, at which distances, of which brightnesses, would be observable by the survey. We wish to constrain both what the brightest object is that could be in the south, and what bright objects we can rule out.

We proceed by assuming that our 90% maximum detection rate applies out to our limiting magnitude, at which point the efficiency drops entirely to zero. From our saturation magnitude of m = 13.0 to our completeness limit of m = 19.0, Kuiper belt objects with absolute magnitudes $-2.42 \leq H \leq 3.52$ and scattered disk objects with $-2.60 \leq H \leq 3.35$ would have been detected in our survey 90% of the time.

We note for interest that the tails of the Kuiper belt detectability were slightly truncated by the absolute magnitude range that we applied to each KBO; the scattered disk range extended beyond the detectability of its objects at both ends, but after processing we found that the Kuiper belt one did not. In retrospect the range should have been made a little wider than H = -3–5.25 to ensure we covered the detection of objects falling fully to zero; we underestimated the range of r_H of the Grav et al. (2011) KBOs. Projecting from the drop in object detectability seen in the scattered disk when binned per H, the Kuiper belt absolute magnitude visibility should go another 0.75–1 magnitudes brighter and 0.5 fainter. This does not affect the 90% detection limit given above, as the KBO limits went below the 50% detection limit within the range of absolute magnitude that we used, just the magnitudes at which our survey could have seen no KBOs at all.

Our survey places a constraint on the bright end of the TNO size distribution. Given our survey detection efficiency function, and the sky area of 6,275.08 square degrees that we

surveyed,[9], 15% of the $4\pi\left(\frac{180}{\pi}^2\right)$ (41,252.96 sq. degrees) of the total sky sphere,[10] we can compute statistical upper limits to the cumulative surface densities of bright $a > 30$ TNOs.

Using the well-defined Grav et al. (2011) populations in our simulator allowed us to consider our survey's sensitivity to population subgroups; for example, we could determine the brightest plutino our survey could have missed.

For the plutinos, we selected the Grav et al. (2011) KBOs with $39.3 \leq a \leq 39.7$ and $0.1 \leq e \leq 0.35$, based on the regions where plutinos are statistically most likely to spend time in the De Elía et al. (2008) map of the orbital distribution of plutinos, as a proxy for identification by full orbital integration. There were 2,816 such objects; 510 were visible in the Uppsala survey and had apparent magnitudes calculated. We computed their detection efficiency as a function of absolute magnitude: after 216 plutinos had processed, the efficiency function, unsurprisingly, was the same as that for the greater KBO population: 90% efficiency, $m = 19$ limiting magnitude. The brightest plutino is (134340) Pluto at $H = -0.7$ ($m_r = 13.6$); our detectability range for plutinos was $-2.0 \leq H \leq 3.9$, so we easily encompass Pluto as expected.

Applying our absence of plutino detections to our sky coverage is a little tricky as plutinos, like other resonant populations, are highly longitude-dependent, and debiasing survey coverage to account for this clumping on the sky with respect to Neptune is a major effort, cf. Gulbis et al. (2010); Gladman et al. (2012). However, we have the advantage of being able to see this population (those of it within our absolute magnitude range) in all parts of their orbits — a big $e = 0.3$ plutino will still be visible to us at aphelion — unlike for the scattered disk, where the objects are only visible for the part of their orbit near perihelion. We therefore do not have flux bias affecting our survey of those plutinos $H < 3.9$ at least.

TNOs of a given inclination i where i is large will as they travel on their orbits spend most of their time near their ecliptic latitudes close to i, not near the ecliptic, so we should be particularly sensitive to the abundance of high-i ($> 23°$) plutinos, a part of the population preferentially lost by surveys that did not make recovery observations a few months after discovery (Gladman et al. 2012). Of these $i > 23°$ plutinos, only four were seen by CFEPS (Gladman et al. 2012) and none by the DES (Gulbis et al. 2010).

Is the null detection of our survey reasonable? Currently, only some ten known TNOs are sufficiently bright and close that, if within our survey coverage, we would have been able to detect them. Estimates of the numbers of objects of these magnitudes remaining undetected vary. As Sheppard et al. (2011) point out, there are only one or two TNOs with $m < 21^{st}$ that could exist in sky unexamined to that time. Of the recent $H < 4.0$ "dwarf planet" discoveries, since those of 2007 JJ_{43}, 2007 OR_{10} ($H = 1.9$) and 2007 UK_{126} ($H = 3.4$) by Schwamb et al. (2010), the only subsequent discoveries have been 2010 EK_{139} ($H = 3.8$) and 2010 KZ_{39} ($H = 3.9$) by Sheppard et al. (2011); Rabinowitz et al. (2012) found no new TNOs with $H < 4$ (though one at $H = 4$) after surveying an area of ~7,500 sq. deg. comparable to

[9] 8,989.66 square degrees is the area of fields where all nights for the field were successfully processed to match astronomical sources together over the span of the survey, and for which we calculated detection efficiencies. We expect the pipeline difficulties between this step and processing for arcs to be overcome. The 1491 fields that have been checked for arcs comprise 6,275.08 square degrees, so we use this value.

[10] Processing to 8,989.66 sq. deg. will bring this to 22% of the sky; after that we can work toward the originally intended 9,498.9 sq. degrees, 23%.

that processed in our own survey.

Our survey searched one of the unexamined regions that Sheppard et al. (2011) mention, the southern fields > 20° in ecliptic latitude (Fig. 3.7), and as was discussed in § 3.2.1, could reasonably have expected to find 1 ± 1 objects in either the KBO or scattered disk populations of these magnitudes, given the proportion of southern hemisphere sky that has not previously been examined for such objects. Our nondetection is therefore not overly surprising, and does not provide any evidence that might contravene the current understanding of early Solar System formation that currently produces these observed small numbers of large TNOs (Kenyon & Bromley 2008; Schlichting & Sari 2011).

How much does this non-detection depress the bright end of the TNO size distribution? As we are sensitive only to the bright end, we consider only its size distribution. This can be further subdivided into the populations of KBOs and the scattered disk, to which we had differing sensitivities due to the flux bias of only being able to see SDOs for part of their orbit. For KBOs, our non-detection does not affect the differential power-law radius distribution given in Eqn. 1.15 for $H < 4.5$ as per Sheppard et al. (2011): $q = 3.3 \pm 0.7$ (main Kuiper belt) and $q = 2.2 \pm 0.5$ (Plutinos), as we add only 7% of sky coverage relevant to these populations (§ 3.2.1).

For the scattered disk, the effect may be more significant as we covered much more of the sky sensitive to their phase space (§ 3.2.1 and area covered as discussed above): $q = 3.3 \pm 0.7$ for SDOs of Sheppard et al. (2011) is based on completeness of objects $H < 4.1$ and $r < 50$ AU due to the population's aphelion bias. However, Sheppard et al. (2011) were covering similar sky to our survey. We conclude that their size distribution for the scattered disk based on the known objects in that absolute magnitude range (Eris, 2007 OR_{10}) is appropriate.

How well qualified are our H-magnitude limits? Fig. 3.5 shows that the plutino (28978) Ixion, $H = 3.3$, would be on the survey, but at magnitude 19.6, it fails to be detected in our survey. Physically, Ixion is 650^{+260}_{-220} km in diameter (Stansberry et al. 2008). Using the time-honoured proxy for TNO size of parts of the author's local landmass, this means the Uppsala TNO survey is sensitive to objects larger in diameter than about three times the size of Victoria, but not to an object with the cross-sectional area of Tasmania.[11]

What yet remains to be searched? Our survey and those of Sheppard et al. (2011) and Rabinowitz et al. (2012) have left only the few thousand square-degree area of the Galactic plane for future surveys to examine for bright TNOs. We agree with Sheppard et al. (2011) that the outer Solar System is effectively complete to $m = 19.0$ and selectively to $m = 21$. This flux limit does not entirely however take into account the biases on which detection is dependent: it describes only the flux bias.

What can be said about this survey's sensitivity to distant objects, those sufficiently large that their H would bring them within our magnitude limit even at several hundred AU ? The test population of Grav et al. (2011) that we used did not contain a population reproducing this, so we did not directly test it with the survey's simulator. Adding a more distant population is discussed in § 4.7.2.

Such distant objects would not have been lost as stars: the constraint we applied in § 3.3.2

[11] Using the upper size estimate for Ixion of a 455 km radius, ie. 650,388 km^2. Victoria is 237,629 km^2, Tasmania (main island) is 62,409 km^2.

was that when dividing stars from transients, for a source to be considered as in the same position, the closest source to that position on a different night had to be at a distance that was also within 4″ of the position. In theory this could mean that the sensitivity of the survey would be limited in the distant case to only the motion rate of objects moving > 4″ between nights, i.e. faster than 0.17 ″/hr: Sedna-at-discovery distances, equivalent to the sensitivity of Schwamb et al. (2010) (Rabinowitz et al. (2012) required a motion rate greater than 0.0044 degrees per day, rejecting objects at distances greater than 200 AU). In practice, Uppsala fields were revisited mostly at intervals between 5 and 20 days (Fig. 3.9) so very few observations of distant objects would be lost from this immediate-night constraint, cf. § 4.3.4.

In practice, the combination of the widely spread Uppsala cadence and the multi-tens-of-days duration of valid triplets shown in Fig. 3.14) offered a proxy for our distant sensitivity. If the implied maximum of valid surviving triplets at temporal spans of 130 days is taken to be representative, and given two triplets have to occur within a single opposition season of 180 days to create a detectable triplet, a motion rate of 4″ in the 180-day maximum span corresponds to a heliocentric distance of many hundreds of AU. This is far beyond where any object of reasonable TNO size would have an apparent magnitude visible to the survey.

The flux limit of the survey is therefore far more significant a factor on distant object detection than their motion rate. We made these calculations of detectability purposefully to exclude the incorporation of albedo; the largest diameter $D > 1000$ km objects have particularly high albedos, $\rho = 0.6$–0.8, influenced by sublimation frost-thaw cycles of their volatile ices refreshing their surfaces (Brown 2008). The theoretical detection limits can be plotted as object diameter (km) (assuming uniform albedo) against detection distance at opposition: Fig. 4.19. Clearly dwarf-planet-sized objects of all reasonable albedos are not detectable by this survey beyond ~ 150 AU, but this survey is easily sensitive to such objects out to there.

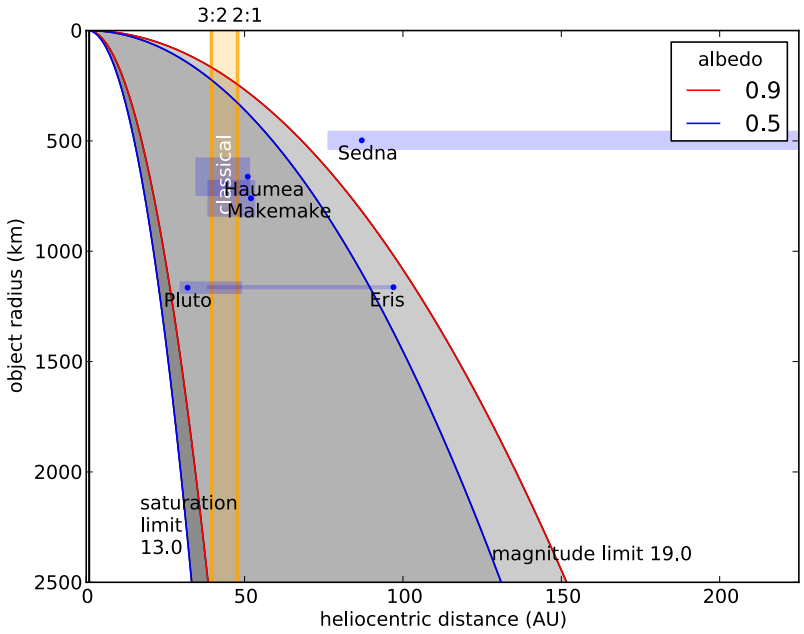

Figure 4.19 At two typical albedos of large TNOs, how the 13.0 saturation and 19.0 limiting magnitudes of this survey affect the .

4.6. Summary

We have surveyed 6,275.1 square degrees to $m = 19.0 \pm 0.2$ with an efficiency of 90%, and tested the effectiveness of our detection strategy on 8,989.7 square degrees to the same detection efficiency and limiting magnitude. With a Monte Carlo approach to testing whether any given TNO would pass our observations's magnitude limits, we found that from a population of several thousand synthetic orbits, we would detect Kuiper belt objects between $-2.43 \leq H \leq 3.51$ and scattered disk objects with $-2.60 \leq H \leq 3.35$. Our survey design is sensitive to bright dwarf planets in these more distant populations, but the constraint of combining intranight observations together to form a single point per night proved geometrically restrictive to Centaurs, and we are not sensitive at all to them.

4.7. Future work

4.7.1. Refinement of magnitude calibration

There is one sky catalogue available with sufficient stellar density and better photometric precision than the USNO-A2.0 that encompasses our Uppsala sky coverage. The AAVSO's APASS Data Release 6 has a density of > 1000 stars/deg^2, providing good flux calibrators from 10^{th} up to 17^{th} magnitude to a photometric accuracy of about 3% in $BVg'r'i'$ filters. Its sky coverage is shown in Fig. 4.20. APASS DR6 has been successfully used for calibration for spot observations by LCOGT, who have obtained better than 3% accuracy on flat-fielded data across a wide range of atmospheric conditions (Pickles & Rosing 2013).

As digital detectors have a linear response, tying the Uppsala stellar magnitudes to APASS

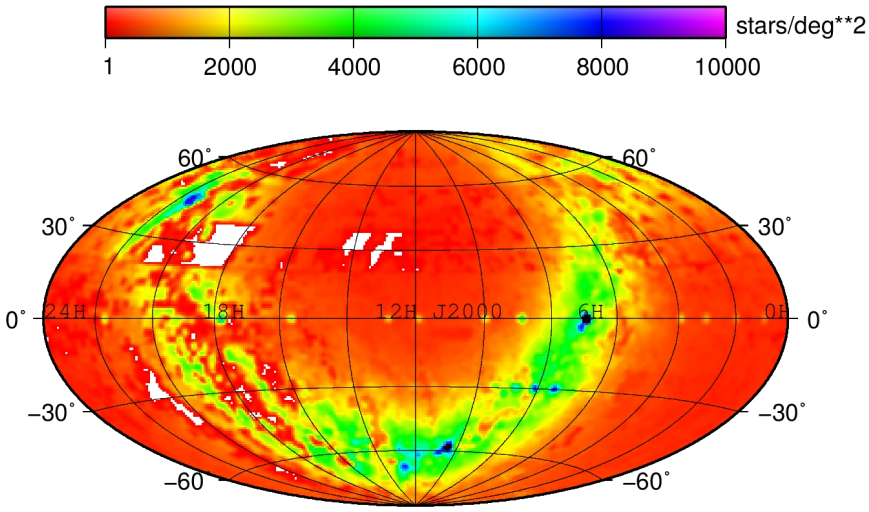

Figure 4.20 The stellar density of the APASS Data Release 6 catalogue across the sky, from the AAVSO website. Note the comprehensive sky coverage.

stars throughout the magnitude range in which they are visible will allow us to calibrate our survey. Our clear filter is roughly equivalent to a V; the APASS provides Johnson V magnitudes, so while we do not have colour information for any stars in the Uppsala survey, we could compare to these APASS V magnitudes by computing a field-by-field direct offset, rather than needing to perform a full colour-dependent transform.

Would the effort produce a noticeable improvement in the survey's usefulness? Sesar et al. (2006) brought the USNO-A2.0 from .234 magnitudes RMS scatter to 0.17 rms after calibrating against the SDSS. So the uncertainties on the magnitude limits for each night that are used to get the overall detectability of an object are 0.2 magnitudes, as given here: this could be improved to ±0.1 by the technique of Sesar et al. (2006). This would have little effect on the overall limits on absolute magnitude-range detectability — this survey operates in the shallowest part of the power law curve of the TNO size distribution, so its sensitivity is not at the point in the range where adding a tenth of an absolute magnitude of precision would greatly affect the survey's sensitivity to the number density of bright objects. The effort to recalibrate the survey may therefore not be necessary for the data the survey can provide.

4.7.2. Improvements to the survey simulator

We would consider in the future generating our ephemerides via `OpenOrb` rather than SLALIB. SLALIB handles only one object at a time, while `OpenOrb` could propagate all $> 170,000$ TNOs in the Grav et al. (2011) model, plus an artificial high-inclination TNO population, for all of the survey's 114,727 nights, and then generate the projection against the sky for ephemeris generation. This would be computationally intensive, but would close off the assumption that our single-year linking prevents the propagation problem being significant.

As most of the Uppsala fields are far from the ecliptic plane, using only the Grav et al. (2011) TNOs left many fields without any synthetic objects falling on them. To counter this, we would create an arbitrary high-inclination, high-eccentricity population with a, e and i,

perhaps e 0.5–0.95, i 30–120°, a 35–150 AU, again with uniform randomisation on Ω, ω, M within their 0-360 degree ranges, and compute the efficiency of detection of these objects over an absolute magnitude range where they would be visible within the $m < 19.0$ regime we determined for the survey. The computational requirements of several 10^6 CPU-hours prevented this as part of our primary analysis.

It would be useful to confirm the restrictions of the survey on its sensitivity to distant objects at several hundreds of AU . Ensuring the population of high-e, high-i objects covers an H range sufficient to check the survey's sensitivity at the objects' aphelion (settling what H was necessary to bring the objects' apparent magnitude within the survey magnitude limits of $m = 19.0 \pm 0.2$) would provide this test.

4.7.3. Serendipitous observation of unknown main-belt comets

Main-belt comets are a recently discovered class of objects that orbit within the asteroid Main Belt, but display episodic low-level cometary activity, ejecting water vapour plumes and developing a short tail, though often with no coma. The discovery of main-belt comets in their cometary phase remains sparse, despite recent surveys (Hsieh & Jewitt 2006; Gilbert & Wiegert 2009; Hsieh 2009; Sonnett et al. 2011; Waszczak et al. 2013); see also the review of Bertini (2011). Long-term photometry could potentially show us the start of their activity and any previous periods of activity: the rotation curves of the known main-belt comets are sufficiently well characterised to be able to see if there are flares in brightness on timescales of months (seasonal effects as the object comes to perihelion appear to play a role (Bertini 2011)) that would indicate cometary activity. More data on these little-understood objects is needed.[12]

The Uppsala data are unlikely to have the resolution or the magnitude depth to show comae around these objects, but they do sample frequently enough to potentially produce long-term photometry on known objects. Four known main-belt comets fell on Uppsala survey fields: Scheila, 133P/Elst-Pizarro, P-2008-R1[13], and P-2010-R2, and we briefly inspected their observations. Scheila, the brightest of the four at magnitude 11.9–15.1 over the course of the survey, was easily detected, but it showed no visually noticeable point-spread function variation in its Uppsala observations on four nights in 2007 and six nights in 2008[14]. Our survey's $m = 19.0$ magnitude limit proved too bright for the other three main-belt comets: they were either too faint for detection, or too faint for any high-quality cometary-activity searching photometry. This is further verification of the TNO survey magnitude limit. For example, the Pan-Starrs-discovered main-belt comet 2006 VW_{139} would in principle have fallen on Uppsala fields on 15 nights between late 2004 and late 2005; in practice, at expected magnitude 19.8 to 22.5, it was too faint for the survey's individual images, with those nights' limiting magnitudes being between 17.8 and 19.5.

Though our brief individual-image examination of the known main-belt comets showed no cometary activity, it might be feasible to use the Siding Spring Survey archive data to search

[12]This search was suggested by Dave Jewitt and Carey Jones while I was at the 2011 Gordon Research Conference on Origin of Solar Systems.

[13]Discovered by G. Garradd at the Uppsala at magnitude 18.3-18.7 on 2008-09-02 (Garradd et al. 2008)

[14]Initial assessment of moving object PSFs for anomalous variability from a point source is often done visually, cf. (Hsieh 2009) and(Gilbert & Wiegert 2009).

for new main-belt comets. The best search strategy would be to take main-belt asteroids from the Minor Planet Center records with appropriate orbits, the Beagle family and other high-r_H main-belt asteroids, and take advantage of the four 30-second images available per night for up to ninety epochs, image stacking and algorithmically searching the stacks for "fuzz". Development of a suitable algorithm for careful statistical checking of PSF variation, to determine if a given source is a point source, would be aided by having the APASS calibrators matched to the data to provide stars as comparators to the PSFs of the moving objects; the similar search of Waszczak et al. (2013) had the advantage that their survey with the Palomar Transient Factory was restricted to only the area with Sloan Digital Sky Survey coverage.

4.7.4. Calibrating the long-period comet record

It would also be possible to track the long-period comets that fell on Uppsala fields, to produce a calibrated record of their changing brightness with heliocentric distance. This photometry would allow a debiasing of the size distribution of the long-period comet population. This task had been originally envisioned for the SkyMapper survey, but the Uppsala dataset should provide more than sufficient photometric coverage.

CHAPTER 5

Conclusions and future directions

> Although the Universe is under no obligation to make sense,
> students in pursuit of the Ph.D. are.
>
> – Robert P. Kirshner[1]

The trans-Neptunian small body populations offer unique insight into the protoplanetary disk of the Solar System. Their present orbits have been sculpted by the giant planets' ancient migrations; their surfaces reflect the strange weathering of a deep space environment on volatile ices. Roughly forty thousand objects are larger than 100 km in diameter; perhaps ten are more than a thousand kilometres in diameter. This portrait of small distant worlds has been primarily constructed through many surveys of the sky, most of which have searched the Northern Hemisphere.

We have completed a comprehensive examination for TNOs that has a 90% detection efficiency of 6,275 sq. deg. of the southern sky, between $13.0 - -19.0 \pm 0.2$ magnitudes in clear. This survey presents an innovative archival approach, using five years of densely revisited data from a near-Earth asteroid survey with the 0.5 m Uppsala telescope and resampling its cadence for much more distant objects. The only slightly similar approach is that of Larsen et al. (2001, 2007), but they retain searching for TNOs by motion within a single night as well as inter-night, and are focussed on the ecliptic. We have created the first large-area fully off-ecliptic bright TNO survey. This gives us sensitivity to bright, potentially large objects with high orbital inclinations.

Our survey pipeline takes a list of point sources in each Siding Spring Survey image, produced by software such as SExtractor, and processes the lists for all images of a given field, restricting potential linkages between points in the field through a limit on the maximum rate of motion. The pipeline initially finds the plausible intrafield orbits for all sets of three points, using a pre-filtering algorithm that selects only for bound orbits. Plausible-orbit prefiltering was necessary to reduce the sheer quantity — a trillion potential orbits — from

[1] *Quarterly Journal of the Royal Astronomical Society.* 1991, Vol. 32, No. 3, p233

considering sets of three of these sources. This prefilter kept bound orbits with suitable orbital parameters and quality of fit: heliocentric distance > 15 AU, a > 0, e < 1, $\chi^2 < 500$. The filtered triplet orbits were then fully fit using the Bernstein & Khushalani (2000) `orbfit` package and reselected under the same criteria. This still left too large a number of potential candidates to blink visually. We subsequently link all permutations of two triplets into arcs and refit the arcs to see if any longer orbital arcs are present, and winnow candidates in the same manner. Finally, we visually inspected the remaining potential candidates to minimise false positives: no trans-Neptunian objects were detected.

Processing the appropriate set of some 568,000 images with this survey design took a hundred thousand CPU-hours. Concluding this thesis in 2013, eighty-three years after the first discovery in the trans-Neptunian region, it may be of interest to compare that Tombaugh (1961) took seven thousand hours of person-time for his ninety million image survey of 30,000 sq. deg. to 17^{th} magnitude. Tombaugh estimated that scanning 5,000 sq. deg. along the ecliptic to 20^{th} magnitude would take three man-years; we note that, like any good astronomer, he was out by a factor of ten.

We place limits on the existence of bright TNOs: we had sensitivity to the absolute magnitude ranges $-2.42 \leq H \leq 3.52$ for the Kuiper belt, and $-2.60 \leq H \leq 3.35$ for scattered disk objects, but detected no new objects. We hope that this constraint on the upper end of the large bright TNO population will inform the development of models of planetesimal formation, and the orbital phase space vacant of such objects may aid in understanding the conditions that gave rise to the dynamical structure of the current Solar System giant and terrestrial planetary arrangement.

The limitations of the Uppsala TNO survey are clear when compared to the ambitious surveys planned in the next decade. SkyMapper, a 1.35 m dedicated survey telescope at Siding Spring which will survey the southern sky to $g = 21.9$ and $r = 21.6$; OSSOS on the CFHT 4 m; HyperSuprimeCam on Subaru, and the fabled 8 m LSST: all offer the promise of expanding and redefining our Solar System's distant reaches. This thesis only concludes our first step.

5.1. Future prospects: SkyMapper

We end this chapter and the thesis with a discussion of the successor survey to our Uppsala TNO survey, the TNO survey that will be part of the forthcoming[2] SkyMapper Southern Sky Survey, and which was the original motivation for this thesis.

The new SkyMapper telescope at Siding Spring has a 1.35 m diameter wide-field primary and a single instrument: the 5.7 deg^2 field of view[3] imager, which has 32 CCDs and 268 megapixels at a filling factor of 91%, with a plate scale of 0.497″ per pixel. This matches well to the median 1.5″ seeing at Siding Spring, providing the appropriate near-Nyquist sampling. A six filter set, *uvgriz*, covers most of the same wavelength bands as the Sloan Digital Sky Survey, with one extra short-wavelength filter, *v*, providing extra information on the position of the Balmer jump for stellar classification (Keller et al. 2007; Bessell et al. 2011).

[2]SkyMapper saw first light in 2009. Vibrations in the telescope which degrade the image quality have prevented the Southern Sky Survey from starting, as of July 2013.

[3]2.373 x 2.395 deg, Granend et al 2006.

The SkyMapper Southern Sky Survey aims to repeatedly image the entire southern sky in these six colours, observing every pointing at temporal spacings with a roughly logarithmic time interval such that all fields are eventually imaged in all filters for either three or six epochs (Keller et al. 2007). The main survey's cadence is set independently for each filter based on the science requirements in that passband. Each filter's cadence is modified by the scheduler software's careful manipulations to avoid the moon, planets, bad weather, poor seeing, and minimise the field's airmass.

One of the main science objectives of the Southern Sky Survey is to provide a photometrically calibrated survey of trans-Neptunian objects. The filters of interest for TNO studies are the *g* and *r* filters, as the reflected light from the objects is brightest in that part of the solar spectrum. Some information could also be provided by the *i* and *z* filters, but TNOs will be much fainter at those wavelengths. The responsibility for setting the cadence of the *g* and *r* filters is therefore entirely controlled by the requirements of the TNO survey. We determined a design for the survey.

5.1.1. The SkyMapper Southern Sky Survey

The initial images taken will be observations for the 5-second-survey. This survey, made only under photometric conditions, will provide the framework of bright stars that will be used to lock all subsequent SkyMapper observations into a world coordinate system (WCS). The magnitude range of this survey will be from 8.5 to 15.5 in *g* (Keller et al. 2007), prohibitively bright for detection of any TNOs much smaller than Pluto. It would provide a check on the existence of any astoundingly large TNOs: as an all-sky survey, it would be able to definitively confirm the absence of such large worlds, at magnitudes where other surveys would have their detectors saturate.

The Southern Sky Survey will occupy 75% of the telescope time, with the remainder given to other proposals, including a dedicated ~ 1200 deg^2 area of supernova surveying. The supernova survey will revisit its fields several times per week in *g* through *z*, with slightly shorter exposure times; this dataset will be mined for colours and photometry of known asteroids, identification of new asteroids, and supplementary data for the TNO survey. 20% of the SkyMapper main sky survey is expected to take place in the first year, although the 5-second survey that provides information to set the world coordinate system for the main survey will take priority. The full initial SkyMapper sky survey is expected to be completed within about three to four years.

The main survey can be made in conditions that are non-photometric but with adequate seeing. Its 110-second integrations will reach up to a depth of 21.9 and 21.6 respectively in each *g* and *r* observation (Table 5.1), with systematics of 0.03 mag and astrometry of 50 mas (Keller et al. 2007). These photometrically calibrated observations form the main dataset for the TNO survey, and set its depth. There are 3845 fields in the Main Survey[4]. The overhead for each observation is 12 seconds, including readout and filter change: this can be accommodated within the time to shift in pointing when the next field is selected.

The approximate depth of the TNO survey is fixed, as the integration time in the Southern Sky Survey is constant across all filters. The primary part of the survey design is therefore

[4]Their centres are given at `https://www.mso.anu.edu.au/local/skymapper/fieldcentres.dat`

Table 5.1 SkyMapper main survey depth in AB magnitudes, 1 epoch[a]

u	v	g	r	i	z
21.5	21.3	21.9	21.6	21.0	20.6

[a] From Keller et al. (2007). Signal-to-noise of 5, 110-second exposures, 1.5″ seeing.

to decide which temporal spacing should be chosen in making the multiple observations required to show that an object is moving. The TNO survey design's requirements are to choose an optimum (g, r) cadence given factors including the range of observed sky positions relative to opposition, the survey sensitivity to asteroids and their amount of contamination of the detection of real TNOs, allowable noise limits in each observation, and the characteristics of `orbfit`, the orbit fitting code of Bernstein & Khushalani (2000) when fitting both real and synthetic Solar System objects with observational errors added. We examine each of these factors, and the tradeoff between the optimal and the practical solutions, in the succeeding sections of § 5.1.2.

5.1.2. SkyMapper TNO survey cadence design

SkyMapper will observe in three cadences:

- (u, v): 3 epochs consecutively
- (g, r): 3 epochs with δt approximately 3 days, exact spacing to be determined by this work
- (i, z): 3 epochs with 5 day spacing.

The SkyMapper survey's temporal spacing of observations, its cadence, is set for each filter independently. The filters of interest for TNO studies are the g and r filters, as the reflected light from the objects is brightest in that part of the solar spectrum. Some information could also be provided by the i and z filters, but TNOs will be much less bright in those wavelengths. The responsibility for setting the cadence of the g and r filters is therefore entirely controlled by the requirements of the TNO survey. In this section, we describe our choices for the TNO survey cadence, outlining the survey's filters and scheduler constraints.

The filters that encompass most of the Sun's light are the b, g, r, i, z set; TNOs are almost all too faint to be observed in u and v.[5] These broad-band filter observations give a few spectral points along the wavelength range, enough to provide the gradient of the wavelength-dependent surface reflectance. This gradient or spectral slope S is expressed as the percentage change in reflectance per unit of wavelength (Doressoundiram et al. 2008):

$$S = \frac{R_{F_1} - R_{F_0}}{\lambda_1 - \lambda_0} \tag{5.1}$$

[5] The passbands of the *uvbri* filters are discussed in Bessell (1990)

where R_{F_0} and R_{F_1} are the reflectances measured in filters F_0 and F_1 with the central wavelengths of λ_0 and λ_1. Often these are given as the various colour indices. The spectral slope and colour indices are used to classify the object. Various taxonomies have been proposed, for example Barucci & Peixinho (2006), but these are not yet widely used. Generic descriptions use two states: a "blue" object has a spectral slope that either decreases with wavelength or is near-flat, which makes it grey in true visual appearance, while a "red" object has a reflectance that increases at longer wavelengths, and which would appear red to the naked eye. Ultrared KBOs and Centaurs exist that have $S > 25\%/100nm$.

The meaning of colours is a hotly debated topic. They correspond to an average of the surface, which could be thrown off significantly by strongly varying regions.

Survey filters

The g filter is solid glass, while the r filter is dielectric-coated glass; both are single-piece at 309 x 309 mm. These filters are close to but not identical to the Sloan bandpasses: the r is nearly unchanged, but the g has its blue edge moved redward to allow a v band to be inserted for fine detection of stellar metallicities (Bessell et al. 2011). This allows easy comparison of the sufficiently southern known TNOs to their well-characterised Sloan colours (Ofek 2012).

We considered sequencing observations as $(g), (u, v), (u, v), (u, v), (i, z), (r)$ to separate the g and r enough to add asteroid detection to the science case, but scheduling this extra complication added too much overhead in filter wheel moves for too little gain in movement for TNO detections. We are therefore scheduling a set of three (g, r) observation pairs. The i and z are likely to detect only sufficiently large TNOs, so that data will be checked but not required for confirmation of TNO detection.

Design considerations

The six-filter observation requirements of the main survey made repeat observations on the field in a single night prohibitive to schedule: we plan for three observations spaced around or at greater length than one week, but all to be observed within one lunation, and to a proper depth. If these observing conditions were not met, the field would need to be redone.

While four observations would be better, fitting that into the scheduler was implausible. Instead, any discoveries will be followed up either by requests to the 25% of Time Allocation Committee-controlled SkyMapper time, or to queue requests to Faulkes South. These followup observations would ideally occur within about three weeks, as each increase in the lag time before followup will increase the orbit's uncertainty and the size of the target area to search.

One week between first and last discovery observations still does not allow Sedna-like objects to be distinguished from the family of orbits of KBO-distant scattered-disk objects near aphelion. Further recovery observations in subsequent years are necessary (Schwamb et al. 2010).

The Sedna-population survey of Schwamb et al. (2009) considered opposition fields to be those within 14° of opposition. Beyond 42° from opposition they had significant contam-

ination from asteroids (M. Schwamb, pers. comm.). With two epochs in one night, they were able to recover possible asteroids 2-3 nights after discovery (as the asteroid motion increased, `orbfit` switches its identification from TNO to asteroid).

We hoped to have control over the patterning sequence of field observation: observing close to the ecliptic early in the survey would be best, preferably observing in an ecliptic tessellation of fields, sequenced in longitudinal swaths to optimise TNO detection across field edges. Our sky coverage overlaps in the north with that of Pan-STARRS, providing comparative calibration. Depth-wise, we also ask the scheduler to keep the depth of the observations to the defined depth in g and r: if some of the observations don't reach an appropriate depth, reschedule and re-observe, as a critical depth is also required for SkyMapper stellar and galactic science.

There are two remaining areas of unsurveyed sky in the south. South of about -80° declination, where telescopes that like Uppsala have equatorial mounts cannot point, leaves a small patch of 376 deg^2. This area over the celestial pole is at ecliptic latitude -65°, so it will have a low probability of containing TNOs even when surveyed to 21st magnitude. The second unsurveyed area is the area of avoidance across the galactic plane. This region is defined in the Uppsala survey as fifteen degrees avoidance either side of the galactic plane, which forms a region that, south of -15° declination where the survey has coverage, is 4,200 deg^2.

The galactic plane falls largely at lower ecliptic latitudes, and is a worthwhile area to survey in the future: the $-10 \leq b \leq 10$ part that is south of the celestial equator covers a substantial 3560 deg^2. We plan an additional TNO search of this region by an image subtraction survey with a modified version of the TNO survey pipeline. The data for this would either come from the Southern Sky Survey, or from a separate survey at a reduced exposure time to lessen the field crowding produced from going to m_r21.6.

Each night, the half-terabyte of main survey data are sent via high-speed link to their archive at the ANU supercomputing facilities. The main SkyMapper data processing pipeline is then run as time allows on the supercomputer's queue, and extracts an object catalogue within a few days of the observations. Since the delay of the supercomputing in producing an object catalogue is of uncertain duration, a separate set of processing is made on the 32-core `miner` machine at Mt Stromlo. This separate processing is maintained by the supernova search team, and is the same as that run on their dedicated supernova search area. We will also run our TNO survey pipeline with their output. A comparable TNO survey from supernova survey data, SDSS Stripe 82 (Table 1.2), surveyed 300 sq. deg to SDSS depths and found 24 new TNOs, going to ±20° ecliptic latitude and providing some constraints on inclination distributions (A. Becker, pers. comm.).

The SN survey maintains an MPC-linked module that identifies known asteroids on their fields to clean their transient list. We plan to harvest these known asteroids for colours and photometry to a separate database, and exclude them from the transient list supplied to the TNO survey pipeline.

Once SkyMapper begins operation, the main survey may be completed within five years; the entire sky will then have been surveyed to better than 90% completion to $m_r \sim 21.5$ or deeper. We can then expect LSST to begin surveying and add new objects to our inventory of the Solar System at a prodigious rate. The next decade of small-body planetary exploration will be an exciting time.

References

Abernathy, M. R., Tegler, S. C., Grundy, W. M., Licandro, J., Romanishin, W., Cornelison, D., & Vilas, F. 2009, ICARUS, 199, 520

Aihara, H., et al. 2011, The Astrophysical Journal Supplement Series, 193, 29

Allen, R. L., Bernstein, G. M., & Malhotra, R. 2001, The Astrophysical Journal, 549, L241

—. 2002, The Astronomical Journal, 124, 2949

Bailey, J. A. 1998, Proceedings of the SPIE, 3355, 932

Barucci, M. A., Boehnhardt, H., Cruikshank, D. P., & Morbidelli, A., eds. 2008a, The Solar System Beyond Neptune (The University of Arizona Press)

Barucci, M. A., & Peixinho, N. 2006, Asteroids, 229, 171

Barucci, M. A., et al. 2008b, Astronomy and Astrophysics, 479, L13

Batygin, K., Brown, M. E., & Fraser, W. C. 2011, The Astrophysical Journal, 738, 13

Bauer, J. M., et al. 2011, EPSC-DPS Joint Meeting 2011, 1390

—. 2013, The Astrophysical Journal, 773, 22

Becker, A. C., et al. 2008, The Astrophysical Journal, 682, L53

Beichman, C. A. 1987, IN: Annual review of astronomy and astrophysics. Volume 25 (A88-13240 03-90). Palo Alto, 25, 521

Bernstein, G., & Khushalani, B. 2000, The Astronomical Journal, 120, 3323

Bernstein, G. M., Trilling, D. E., Allen, R. L., Brown, M. E., Holman, M., & Malhotra, R. 2004, The Astronomical Journal, 128, 1364

—. 2006, The Astronomical Journal, 131, 2364

Bertin, E., & Arnouts, S. 1996, Astronomy and Astrophysics Supplement, 117, 393

Bertini, I. 2011, Planetary and Space Science, 59, 365

Bessell, M., Bloxham, G., Schmidt, B., Keller, S., Tisserand, P., & Francis, P. 2011, arXiv, astro-ph.IM

Bessell, M. S. 1990, Astronomical Society of the Pacific, 102, 1181

Bianco, F. B., et al. 2010, The Astronomical Journal, 139, 1499

Boehnhardt, H., & Hainaut, O. 2000, The Transneptunian Population, 4, 20

—. 2002, In: Highlights of Astronomy, 12, 239

Boulade, O., et al. 1998, Society of Photo-Optical Instrumentation Engineers (SPIE) Conference Series, 3355, 614

Bowell, E., Hapke, B., Domingue, D., Lumme, K., Peltoniemi, J., & Harris, A. W. 1989, in Asteroids II; Proceedings of the Conference, Tucson, AZ, Mar. 8-11, 1988 (Tucson, Arizona: IN: Asteroids II; Proceedings of the Conference, Tucson, AZ, Mar. 8-11, 1988 (A90-27001 10-91). Tucson, AZ, University of Arizona Press, 1989, p. 524-556.), 524–556

Brannigan, E., Takami, M., Chrysostomou, A., & Bailey, J. 2006, Monthly Notices of the Royal Astronomical Society, 367, 315

Brown, M. E. 2001, The Astronomical Journal, 121, 2804

—. 2002, Annual Review of Earth and Planetary Sciences, 30, 307

—. 2008, in The Solar System Beyond Neptune (The University of Arizona Press), 335–344

—. 2012, Annual Review of Earth and Planetary Sciences, 40, 467

Brown, M. E., Barkume, K. M., Blake, G. A., Schaller, E. L., Rabinowitz, D. L., Roe, H. G., & Trujillo, C. A. 2007, The Astronomical Journal, 133, 284

Brown, M. E., & Calvin, W. M. 2000, Science, 287, 107

Brown, M. E., Kulkarni, S. R., & Liggett, T. J. 1997, The Astrophysical Journal, 490, L119

Brown, M. E., & Pan, M. 2004, The Astronomical Journal, 127, 2418

Brown, M. E., Trujillo, C., & Rabinowitz, D. 2004, The Astrophysical Journal, 617, 645

Brown, M. E., Trujillo, C. A., & Rabinowitz, D. L. 2005, The Astrophysical Journal, 635, L97

Brown, M. J. I., & Webster, R. L. 1998, Publications of the Astronomical Society of Australia, 15, 176

Budding, E., & Demircan, O. 2007, Introduction to astronomical photometry, 2nd edn. (Cambridge University Press)

Buie, M. W., & Grundy, W. M. 2000, ICARUS, 148, 324

Canup, R. M. 2005, Science, 307, 546

Chiang, E. I., & Brown, M. E. 1999, The Astronomical Journal, 1411

Christensen, E., et al. 2012, AAS/Division for Planetary Sciences Meeting Abstracts, 44

Christy, J. W., & Harrington, R. S. 1978, Astronomical Journal, 83, 1005

Cochran, A. L., Cochran, W. D., & Torbett, M. V. 1991, Bulletin of the American Astronomical Society, Vol 23, p1314

Cochran, A. L., Levison, H. F., Stern, S. A., & Duncan, M. J. 1995, The Astrophysical Journal, 455, 342

Cochran, A. L., Levison, H. F., Tamblyn, P., Stern, S. A., & Duncan, M. J. 1998, The Astrophysical Journal, 503, L89

Collaboration, L. S., et al. 2009, eprint arXiv:0912.0201

Cook, J. C., Desch, S. J., Roush, T. L., Trujillo, C. A., & Geballe, T. R. 2007, The Astrophysical Journal, 663, 1406

Cook, J. C., Olkin, C. B., Desch, S. J., Mastrapa, R. M., Roush, T. L., & Verbiscer, A. J. 2009, 40th Lunar and Planetary Science Conference, 40, 2222

Cooper, P. D., Johnson, R. E., & Quickenden, T. I. 2003, ICARUS, 166, 444

Cooper, P. D., Moore, M. H., & Hudson, R. L. 2008, ICARUS, 194, 379

Dauphas, N., & Chaussidon, M. 2011, Annual Review of Earth and Planetary Sciences, 39, 351

Dawes, A., et al. 2007, Journal of Chemical Physics, 126, 4711

De Elía, G. C., Brunini, A., & Di Sisto, R. P. 2008, Astronomy and Astrophysics, 490, 835

Delsanti, A., Hainaut, O. R., Boehnhardt, H., & Delahodde, C. E. 2000, American Astronomical Society, 32, 1031

Delsanti, A. C., Hainaut, O. R., Boehnhardt, H., Delahodde, C. E., Sekiguchi, T., & West, R. M. 1999, American Astronomical Society, 31

DePoy, D. L., et al. 2008, in Astronomical Telescopes and Instrumentation: Synergies Between Ground and Space, ed. I. S. McLean & M. M. Casali (SPIE), 70140E–70140E–9

Djorgovski, S. G., et al. 2011, The First Year of MAXI: Monitoring Variable X-ray Sources, arXiv 1102.5004v1

Doressoundiram, A., Boehnhardt, H., Tegler, S. C., & Trujillo, C. 2008, in The Solar System Beyond Neptune, ed. M. A. Barucci, H. Boehnhardt, D. P. Cruikshank, & A. Morbidelli (The University of Arizona Press), 91

Dumas, C., Terrile, R. J., Brown, R. H., Schneider, G., & Smith, B. A. 2001, The Astronomical Journal, 121, 1163

Elias, J. H., Joyce, R. R., Liang, M., Muller, G. P., Hileman, E. A., & George, J. R. 2006a, in Astronomical Telescopes and Instrumentation, ed. I. S. McLean & M. Iye (SPIE), 62694C–62694C–12

Elias, J. H., Rodgers, B., Joyce, R. R., Lazo, M., Doppmann, G., Winge, C., & Rodríguez-Ardila, A. 2006b, in Astronomical Telescopes and Instrumentation, ed. I. S. McLean & M. Iye (SPIE), 626914–626914–12

Elliot, J. L., Kern, S. D., Gulbis, A. A. S., & Kane, J. F. 2006, XI IAU Regional Latin American Meeting of Astronomy (Eds. L. Infante & M. Rubio) Revista Mexicana de Astronomía y Astrofísica (Serie de Conferencias) Vol. 26, 26, 1

Elliot, J. L., et al. 2005, The Astronomical Journal, 129, 1117

—. 2010, Nature, 465, 897

Fitzsimmons, A. 2000, Minor Bodies in the Outer Solar System: Proceedings of the ESO Workshop Held at Garching, 87

Francis, P. J. 2005, The Astrophysical Journal, 635, 1348

Fraser, W. C., & Kavelaars, J. J. 2008, ICARUS, 198, 452

—. 2009, The Astronomical Journal, 137, 72

Fraser, W. C., et al. 2008, ICARUS, 195, 827

Fuentes, C. I., George, M. R., & Holman, M. J. 2009, The Astrophysical Journal, 696, 91

Fuentes, C. I., & Holman, M. J. 2008, The Astronomical Journal, 136, 83

Fuentes, C. I., Holman, M. J., Trilling, D. E., & Protopapas, P. 2010, The Astrophysical Journal, 722, 1290

Fuentes, C. I., Trilling, D. E., & Holman, M. J. 2011, The Astrophysical Journal, 742, 118

Garradd, G. J., Sostero, G., Camilleri, P., Guido, E., Jacques, C., & Pimentel, E. 2008, IAU Circ., 8969, 1

Gilbert, A. M., & Wiegert, P. A. 2009, ICARUS, 201, 714

Girardi, L., et al. 2011, in Red Giants as Probes of the Structure and Evolution of the Milky Way (Berlin, Heidelberg: Springer Berlin Heidelberg), 165–170

Gladman, B. 2002, ICARUS, 157, 269

Gladman, B., Kavelaars, J. J., Nicholson, P. D., Loredo, T. J., & Burns, J. A. 1998, The Astronomical Journal, 116, 2042

Gladman, B., Kavelaars, J. J., Petit, J.-M., Morbidelli, A., Holman, M. J., & Loredo, T. 2001, The Astronomical Journal, 122, 1051

Gladman, B., Marsden, B. G., & Vanlaerhoven, C. 2008, Space Science Reviews, -1, 43

Gladman, B., et al. 2009, The Astrophysical Journal, 697, L91

—. 2012, The Astronomical Journal, 144, 23

Gomes, R. D. S. 2009, Celestial Mechanics and Dynamical Astronomy, 104, 39

Gomes, R. S., Matese, J. J., & Lissauer, J. J. 2006, ICARUS, 184, 589

Graham, J. A. 1982, Publications of the Astronomical Society of the Pacific, 94, 244

Grav, T., Jedicke, R., Denneau, L., Chesley, S., Holman, M. J., & Spahr, T. B. 2011, Publications of the Astronomical Society of the Pacific, 123, 423

Grundy, W., NOLL, K., & STEPHENS, D. 2005, ICARUS, 176, 184

Gulbis, A. A. S., Elliot, J. L., Adams, E. R., Benecchi, S. D., Buie, M. W., Trilling, D. E., & Wasserman, L. H. 2010, The Astronomical Journal, 140, 350

Gulbis, A. A. S., et al. 2006, Nature, 439, 48

Hapke, B. 2005, Theory of Reflectance and Emittance Spectroscopy (University of Pittsburgh: Theory of Reflectance and Emittance Spectroscopy)

Hill, G. W. 1879, Monthly Notices of the Royal Astronomical Society, 39, 258

Høg, E., et al. 2000, Astronomy and Astrophysics, 355, L27

Horner, J., & Evans, N. W. 2002, Monthly Notices of the Royal Astronomical Society, 335, 641

Houck, J. R., et al. 1984, Astrophysical Journal, 278, L63

Hsieh, H. H. 2009, Astronomy and Astrophysics, 505, 1297

Hsieh, H. H., & Jewitt, D. 2006, Science, 312, 561

Irwin, M., Tremaine, S., & Zytkow, A. N. 1995, Astronomical Journal v.110, 110, 3082

Ivezic, Z., et al. 2001, The Astronomical Journal, 122, 2749

Jewitt, D. 2000a, The Transneptunian Population, 4, 18

Jewitt, D. 2000b, in Minor Bodies in the Outer Solar System: Proceedings of the ESO Workshop Held at Garching, Institute for Astronomy, University of Hawaii, 2680 Woodlawn Drive, Honolulu, HI 96822, USA, 1

—. 2010, Proceedings of the International Astronomical Union, 5, 3

Jewitt, D., & Luu, J. 1993, Nature (ISSN 0028-0836), 362, 730

Jewitt, D., Luu, J., & Chen, J. 1996, Astronomical Journal v.112, 112, 1225

Jewitt, D., Luu, J., & Trujillo, C. 1998, The Astronomical Journal, 115, 2125

Jewitt, D. C., & Luu, J. 2004, Nature, 432, 731

Jewitt, D. C., & Luu, J. X. 1995, The Astronomical Journal (ISSN 0004-6256), 109, 1867

Jones, R. L., Parker, J. W., Bieryla, A., Marsden, B. G., Gladman, B., Kavelaars, J., & Petit, J.-M. 2010, The Astronomical Journal, 139, 2249

Jones, R. L., et al. 2006, ICARUS, 185, 508

Juric, M., et al. 2008, The Astrophysical Journal, 673, 864

Kaib, N. A., et al. 2009, The Astrophysical Journal, 695, 268

Kavelaars, J., Jones, L., Gladman, B., Parker, J. W., & Petit, J.-M. 2008a, in The Solar System Beyond Neptune (The Solar System Beyond Neptune, M. A. Barucci, H. Boehnhardt, D. P. Cruikshank, and A. Morbidelli (eds.), University of Arizona Press, Tucson, 592 pp., p.59-69), 59–69

Kavelaars, J. J., Gladman, B., Petit, J., Parker, J. W., & Jones, L. 2008b, American Astronomical Society, 40, 481

Kavelaars, J. J., et al. 2009, The Astronomical Journal, 137, 4917

Keller, S. C., et al. 2007, Publications of the Astronomical Society of Australia, 24, 1

Kenyon, S. J., & Bromley, B. C. 2008, The Astrophysical Journal Supplement Series, 179, 451

Kenyon, S. J., Bromley, B. C., O'Brien, D. P., & Davis, D. R. 2007, arXiv, astro-ph

Kiss, C., et al. 2013, Astronomy and Astrophysics, 555, 3

Kowal, C. T. 1989, ICARUS, 77, 118

Kowal, C. T., Liller, W., & Marsden, B. G. 1979, Proceedings of the International Astronomical Union, 81, 245

Kraus, A. L., & Ireland, M. J. 2011, The Astrophysical Journal, 745, 5

Kretke, K. A., Levison, H. F., & Buie, M. W. 2011, American Astronomical Society, 42, 0902

Lacerda, P. 2010, in Proceedings of the International Astronomical Union, 192–196

Lagrange, A. M., et al. 2010, Science, 329, 57

Landolt, A. U. 1992, The Astronomical Journal, 104, 340

Larsen, J. A., et al. 2001, Space Science Reviews, 121, 562

—. 2007, The Astronomical Journal, 133, 1247

Larson, S., Beshore, E., Hill, R., Christensen, E., McLean, D., Kolar, S., McNaught, R., & Garradd, G. 2003, Bulletin of the American Astronomical Society, 35, 982

Larson, S., Brownlee, J., Hergenrother, C., & Spahr, T. 1998, Bulletin of the American Astronomical Society, 30, 1037

Lecar, M., Podolak, M., Sasselov, D., & Chiang, E. 2006, The Astrophysical Journal, 640, 1115

Lellouch, E., Sicardy, B., De Bergh, C., Käufl, H. U., Kassi, S., & Campargue, A. 2009, Astronomy and Astrophysics, 495, L17

Leonard, F. C. 1930, Astronomical Society of the Pacific Leaflets, 1, 121

Levison, H. F., & Duncan, M. J. 1990, Astronomical Journal (ISSN 0004-6256), 100, 1669

Levison, H. F., Morbidelli, A., Gomes, R., & Backman, D. 2007, Protostars and Planets V, 669

Levison, H. F., Morbidelli, A., Vanlaerhoven, C., Gomes, R., & Tsiganis, K. 2008, ICARUS, 196, 258

Luu, J., Marsden, B. G., Jewitt, D., Trujillo, C. A., Hergenrother, C. W., Chen, J., & Offutt, W. B. 1997, Nature, 387, 573

Luu, J. X., & Jewitt, D. 1988, Astronomical Journal (ISSN 0004-6256), 95, 1256

Luu, J. X., & Jewitt, D. C. 1998a, Astrophysical Journal Letters v.502, 502, L91

—. 1998b, The Astrophysical Journal, 494, L117

Lykawka, P. S., & Mukai, T. 2005, Planetary and Space Science, 53, 1319

Malhotra, R. 1993, Nature, 365, 819

—. 1995, The Astronomical Journal, 110, 420

Marshall, S., et al. 2001, American Astronomical Society, 33, 1048

Martin, R. G., & Livio, M. 2012, Space Science Reviews, 425, L6

Mastrapa, R. M. E., & Brown, R. H. 2006, ICARUS, 183, 207

Matese, J. J., & Whitmire, D. P. 2011, ICARUS, 211, 926

Merlin, F., Barucci, M. A., De Bergh, C., Demeo, F. E., Alvarez-Candal, A., Dumas, C., & Cruikshank, D. P. 2010, ICARUS, 210, 930

Millis, R. L., Buie, M. W., Wasserman, L. H., Elliot, J. L., Kern, S. D., & Wagner, R. M. 2002, The Astronomical Journal, 123, 2083

Miyazaki, S., et al. 2012, in SPIE Astronomical Telescopes + Instrumentation, ed. I. S. McLean, S. K. Ramsay, & H. Takami (SPIE), 84460Z–84460Z–9

Monet, D. 1998, USNO-A2.0 (United States Naval Observatory.)

Moody, R. 2004, PhD thesis, RSAA, the Australian National University.

Moody, R., Schmidt, B., Alcock, C., Goldader, J., Axelrod, T., Cook, K. H., & Marshall, S. 2003, Earth, 92, 125

Moore, M. H., Ferrante, R. F., Hudson, R. L., & Stone, J. N. 2007, ICARUS, 190, 260

Morbidelli, A. 2005, arXiv.org, 12256

Morbidelli, A., & Brown, M. E. 2004, Comets II, 175

Morbidelli, A., Levison, H. F., & Gomes, R. 2008, in The Solar System Beyond Neptune (The University of Arizona Press), 275–292

Murray-Clay, R. A., & Schlichting, H. E. 2011, The Astrophysical Journal, 730, 132

Nesvorný, D. 2011, The Astrophysical Journal Letters, 742, L22

Nesvorny, D., Youdin, A. N., & Richardson, D. C. 2010, The Astronomical Journal, 140, 785

Noll, K. S., Grundy, W. M., Stephens, D. C., Levison, H. F., & Kern, S. D. 2008, ICARUS, 194, 758

Ofek, E. O. 2012, arXiv.org

Oka, A., Nakamoto, T., & Ida, S. 2011, The Astrophysical Journal, 738, 141

Ortiz, J. L., et al. 2012, Nature, 491, 566

Parker, A. H., & Kavelaars, J. 2010a, arXiv, astro-ph.EP

Parker, A. H., & Kavelaars, J. J. 2010b, The Astrophysical Journal, 722, L204

—. 2011, The Astrophysical Journal, 744, 139

Person, M. J., Elliot, J. L., Gulbis, A. A. S., Pasachoff, J. M., Babcock, B. A., Souza, S. P., & Gangestad, J. 2006, The Astronomical Journal, 132, 1575

Petit, J.-M., Holman, M. J., Gladman, B. J., Kavelaars, J. J., Scholl, H., & Loredo, T. J. 2006, Monthly Notices of the Royal Astronomical Society, 365, 429

Petit, J.-M., Kavelaars, J. J., Gladman, B., & Loredo, T. 2008, The Solar System Beyond Neptune, -1, 71

Petit, J.-M., et al. 2011, The Astronomical Journal, 142, 131

Pickles, A. J., & Rosing, W. E. 2013, Proceedings for the Calibration and Standardization of Large Surveys, Missions in Astronomy and Astrophysics conference (Fermilab, April 16-19, 2012)

Polishook, D., et al. 2012, Monthly Notices of the Royal Astronomical Society, 421, 2094

Porter, J. M., Oudmaijer, R. D., & Baines, D. 2004, Astronomy and Astrophysics, 428, 327

Protopapa, S., Boehnhardt, H., Herbst, T. M., Cruikshank, D. P., Grundy, W. M., Merlin, F., & Olkin, C. B. 2008, Astronomy and Astrophysics, 490, 365

Rabinowitz, D., Schwamb, M. E., Hadjiyska, E., & Tourtellotte, S. 2012, The Astronomical Journal, 144, 140

Rabinowitz, D., & Team, t. Q. E. S. 2000, American Astronomical Society, 32, 1028

Rabinowitz, D. L., Barkume, K. M., Brown, M. E., Roe, H., Schwartz, M., Tourtellotte, S., & Trujillo, C. 2006, The Astrophysical Journal, 639, 1238

Ragozzine, D., & Brown, M. E. 2009, The Astronomical Journal, 137, 4766

Rhoads, E. 2005, PhD thesis, Ph.D dissertation, 2005. 95 pages; United States – Minnesota: University of Minnesota; 2005. Publication Number: AAT 3167711. DAI-B 66/03, p. 1511, Sep 2005

Romanishin, W., & Tegler, S. C. 2005, ICARUS, 179, 523

Rousselot, P., Petit, J., Poulet, F., & Sergeev, A. 2005, ICARUS, 176, 478

Russell, H. N. 1916, The Astrophysical Journal, 43, 173

Schaller, E. L., & Brown, M. E. 2007a, The Astrophysical Journal, 670, L49

—. 2007b, The Astrophysical Journal, 659, L61

Schlichting, H. E., Ofek, E. O., Wenz, M., Sari, R., Gal-Yam, A., Livio, M., Nelan, E., & Zucker, S. 2009, Nature, 462, 895

Schlichting, H. E., & Sari, R. 2011, The Astrophysical Journal, 728, 68

Schwamb, M. E., Brown, M. E., & Rabinowitz, D. L. 2009, The Astrophysical Journal Letters, 694, L45

Schwamb, M. E., Brown, M. E., Rabinowitz, D. L., & Ragozzine, D. 2010, The Astrophysical Journal, 720, 1691

Sekiguchi, T., Ootsubo, T., Hasegawa, S., Usui, F., Cruikshank, D. P., Dalle Ore, C. M., & Müller, T. G. 2012, Asteroids, 1667, 6477

Sesar, B., et al. 2006, The Astronomical Journal, 131, 2801

Seto, N., & Cooray, A. 2007, The Astrophysical Journal, 659, L33

Shankman, C., Gladman, B. J., Kaib, N., Kavelaars, J. J., & Petit, J.-M. 2013, The Astrophysical Journal Letters, 764, L2

Sheppard, S. S. 2010, The Astronomical Journal, 139, 1394

Sheppard, S. S., Jewitt, D. C., Trujillo, C. A., Brown, M. J. I., & Ashley, M. C. B. 2000, The Astronomical Journal, 120, 2687

Sheppard, S. S., & Trujillo, C. A. 2010, Science, 329, 1304

Sheppard, S. S., et al. 2011, The Astronomical Journal, 142, 98

Sicardy, B., et al. 2011, Nature, 478, 493

Snodgrass, C., Carry, B., Dumas, C., & Hainaut, O. 2010, Astronomy and Astrophysics, 511, 72

Sonnett, S., Kleyna, J., Jedicke, R., & Masiero, J. 2011, ICARUS, 215, 534

Stansberry, J., Grundy, W., Brown, M. E., Cruikshank, D., Spencer, J., Trilling, D., & Margot, J. L. 2008, in The Solar System Beyond Neptune (The University of Arizona Press), 161–179

Stephens, D. C., & Noll, K. S. 2006, The Astronomical Journal, 131, 1142

Stetson, P. B. 2000, Publications of the Astronomical Society of the Pacific, 112, 925

Strazzulla, G., & Palumbo, M. E. 1998, Planetary and Space Science, 46, 1339

Taylor, S. R. 2001, Solar System Evolution: A New Perspective (Australian National University, Canberra: Solar System Evolution)

Thirouin, A., Ortiz, J. L., Duffard, R., Santos-Sanz, P., Aceituno, F. J., & Morales, N. 2010, Astronomy and Astrophysics, 522, 93

Tisserand, F. 1890, Bulletin Astronomique, 7, 184

Todd, D. P. 1880, Space Science Reviews, 1, 167

Tombaugh, C. W. 1946, Astronomical Society of the Pacific Leaflets, 5, 73

—. 1961, Planets and Satellites, 12

Torbett, M. V. 1989, The Astronomical Journal, 98, 1477

Trujillo, C., & Jewitt, D. 1998, The Astronomical Journal, 115, 1680

Trujillo, C. A. 2008, Space Science Reviews, 573

Trujillo, C. A., & Brown, M. E. 2003, Earth, 92, 99

Trujillo, C. A., Brown, M. E., Barkume, K. M., Schaller, E. L., & Rabinowitz, D. L. 2007, The Astrophysical Journal, 655, 1172

Trujillo, C. A., Jewitt, D. C., & Luu, J. X. 2000, The Astrophysical Journal, 529, L103

—. 2001a, The Astronomical Journal, 122, 457

Trujillo, C. A., Luu, J. X., Bosh, A. S., & Elliot, J. L. 2001b, The Astronomical Journal, 122, 2740

Tsiganis, K., Gomes, R., Morbidelli, A., & Levison, H. F. 2005, Nature, 435, 459

Tyson, J. A., Guhathakurta, P., Bernstein, G. M., & Hut, P. 1992, Bulletin of the American Astronomical Society, 24, 1127

Usui, F., et al. 2011, Publications of the Astronomical Society of Japan, 63, 1117

Volk, K., & Malhotra, R. 2011, The Astrophysical Journal, 736, 11

Waszczak, A., et al. 2013, Monthly Notices of the Royal Astronomical Society, 433, 3115

Williams, I. 1995, ICARUS, 116, 180

Wright, E. L. 2011, Space Science Reviews, -1, 31302

Zakamska, N. L., & Tremaine, S. 2005, The Astronomical Journal, 130, 1939

Zalucha, A. M., Zhu, X., Gulbis, A. A. S., Strobel, D. F., & Elliot, J. L. 2011, ICARUS, 214, 685

Zheng, W., Jewitt, D., & Kaiser, R. I. 2009, J.Phys.Chem.A, 11174

APPENDIX A

Uppsala survey

Table A.1 Field centres used for pointing in the Uppsala 0.5 m Southern Sky Survey. Partial version of table; the full 8700-plus line version can be found in the electronic version of this thesis. Note that this table comprises all the fields that the Survey observes, not only those fields with 30+ observations that were used to form the Uppsala TNO survey. Fields used in the final survey per survival through the pipeline described in § 3.2.1 are indicated by ∗ on their field ID.

Field ID	RA (hours)	Dec	Ecliptic lat.	Ecliptic lon.	Galactic lat.	Galactic lon.
S17060	08:18:08.3	-17:08:29.9	131.84	-35.70	238.85	+10.72
S17061	08:26:30.6	-17:08:29.9	134.20	-35.13	239.98	+12.39
S17062	08:34:53.0	-17:08:29.9	136.52	-34.54	241.15	+14.04
S17063	08:43:15.3	-17:08:29.9	138.83	-33.93	242.35	+15.66
S17064	08:51:37.6	-17:08:29.9	141.10	-33.29	243.59	+17.27
S17065*	08:59:59.9	-17:08:29.9	143.35	-32.63	244.86	+18.86
S17066*	09:08:22.3	-17:08:29.9	145.58	-31.95	246.19	+20.43
S17067*	09:16:44.6	-17:08:29.9	147.78	-31.26	247.55	+21.97
S17068*	09:25:06.9	-17:08:29.9	149.96	-30.54	248.96	+23.49
S17069*	09:33:29.2	-17:08:29.9	152.11	-29.82	250.43	+24.98
S17070*	09:41:51.6	-17:08:29.9	154.25	-29.07	251.94	+26.44
S17071*	09:50:13.9	-17:08:29.9	156.36	-28.32	253.51	+27.87
S17072*	09:58:36.2	-17:08:29.9	158.45	-27.55	255.15	+29.27
S17073*	10:06:58.5	-17:08:29.9	160.52	-26.77	256.84	+30.63
S17074*	10:15:20.9	-17:08:29.9	162.57	-25.98	258.60	+31.95
S17075	10:23:43.2	-17:08:29.9	164.60	-25.18	260.42	+33.22
S17076	10:32:05.5	-17:08:29.9	166.62	-24.37	262.32	+34.46
S17077*	10:40:27.8	-17:08:29.9	168.62	-23.56	264.28	+35.65
S17078*	10:48:50.2	-17:08:29.9	170.60	-22.74	266.32	+36.78
S17079	10:57:12.5	-17:08:29.9	172.57	-21.92	268.44	+37.86
S17080	11:05:34.8	-17:08:29.9	174.53	-21.09	270.63	+38.89
S17081	11:13:57.2	-17:08:29.9	176.47	-20.26	272.90	+39.85
S17082*	11:22:19.5	-17:08:29.9	178.41	-19.43	275.24	+40.75
S17083*	11:30:41.8	-17:08:29.9	180.33	-18.60	277.66	+41.58
S17084	11:39:04.1	-17:08:29.9	182.24	-17.76	280.15	+42.34
S17085	11:47:26.5	-17:08:29.9	184.15	-16.93	282.70	+43.03
S17086	11:55:48.8	-17:08:29.9	186.05	-16.10	285.32	+43.63
S17087*	12:04:11.1	-17:08:29.9	187.94	-15.28	288.00	+44.15
S17088*	12:12:33.4	-17:08:29.9	189.83	-14.45	290.73	+44.59
S17089*	12:20:55.8	-17:08:29.9	191.71	-13.64	293.51	+44.94
S17090*	12:29:18.1	-17:08:29.9	193.59	-12.82	296.31	+45.20

[a] Fields marked with ∗ are the 2136 that have produced lists of matched candidates and transient sources.